Applied Research Laboratory

AD-A236 335

Technical Report

A MODAL ANALYSIS OF SUBMERGED
COMPOSITE PLATES USING DIGITAL SPECKLE
PATTERN INTERFEROMETRY

by

T. F. Bergen
M. J. Pechersky

DTIC
ELECTE
S MAY 3 0 1991
E D

PENNSTATE

91-00653

The Pennsylvania State University
APPLIED RESEARCH LABORATORY
P.O. Box 30
State College, PA 16804

A MODAL ANALYSIS OF SUBMERGED
COMPOSITE PLATES USING DIGITAL SPECKLE
PATTERN INTERFEROMETRY

by

T. F. Bergen
M. J. Pechersky

Technical Report No. TR 91-006
May 1991

REPORT DOCUMENTATION PAGE

Public reporting burden for this collection of information is estimated to average 1 hour per response, including the time for reviewing instructions, searching existing data sources, gathering and maintaining the data needed, and completing and reviewing the collection of information. Send comments regarding this burden estimate or any other aspect of this collection of information, including suggestions for reducing this burden, to Washington Headquarters Services, Directorate for Information Operations and Reports, 1215 Jefferson Davis Highway, Suite 1204, Arlington, VA 22202-4302, and to the Office of Management and Budget, Paperwork Reduction Project (0704-0188), Washington, DC 20503.

1. AGENCY USE ONLY (Leave blank)	2. REPORT DATE	3. REPORT TYPE AND DATES COVERED
	May 1991	

4. TITLE AND SUBTITLE	5. FUNDING NUMBERS
A Modal Analysis of Submerged Composite Plates Using Digital Speckle Pattern Interferometry	N00039-88-C0051

6. AUTHOR(S)

T. F. Bergen, M. J. Pechersky

7. PERFORMING ORGANIZATION NAME(S) AND ADDRESS(ES)	8. PERFORMING ORGANIZATION REPORT NUMBER
Applied Research Laboratory Penn State University P.O. Box 30 State College, PA 16804	TR-91-006

9. SPONSORING / MONITORING AGENCY NAME(S) AND ADDRESS(ES)	10. SPONSORING / MONITORING AGENCY REPORT NUMBER
Space and Naval Warfare Systems Command Department of the Navy Washington, DC 20363-5100	

11. SUPPLEMENTARY NOTES

12a. DISTRIBUTION / AVAILABILITY STATEMENT	12b. DISTRIBUTION CODE
Approved for public release; distribution unlimited	

13. ABSTRACT (Maximum 200 words)

An experimental analysis of the modal vibrations of laminated composite plates with free and cantilever boundary conditions is described in this thesis. The vibrations of the plates are studied in air and when submerged in a water tank to examine the effects of fluid loading on the plates. The experiments were also performed on similar homogeneous aluminum plates to illustrate the effects of anisotropy in the composites.

The analysis was performed with the experimental technique of Digital Speckle Pattern Interferometry (DSPI) which is like holographic interferometry with the exception that a video camera and digital image processor are used to collect and process the holographic images. DSPI provides full-field, non-intrusive, out-of-plane displacement measurements of vibrating structures, and produces mode shapes in the form of speckle correlation fringe patterns. In addition, the drive point mobilities of the plates were determined with the aid of a laser Doppler vibrometer.

14. SUBJECT TERMS		15. NUMBER OF PAGES
modal vibrations, composites, plate, cantilever, fluid loading, interferometry		168
		16. PRICE CODE

17. SECURITY CLASSIFICATION OF REPORT	18. SECURITY CLASSIFICATION OF THIS PAGE	19. SECURITY CLASSIFICATION OF ABSTRACT	20. LIMITATION OF ABSTRACT
Unclassified	Unclassified	Unclassified	Unlimited

The results of the experiments showed that the composites exhibited unpredictable modal behavior due to anisotropy in the plates. For this reason, DSPI proved to be an efficient technique for acquiring mode shapes. In addition, the use of vibrometry in conjunction with DSPI provided an accurate experimental modal analysis system.

Accession For		
NTIS GRA&I	☒	
DTIC TAB	☐	
Unannounced	☐	
Justification		
By		
Distribution/		
Availability Codes		
	Avail and/or	
Dist	Special	
A-1		

ABSTRACT

An experimental analysis of the modal vibrations of laminated composite plates with free and cantilever boundary conditions is described in this thesis. The vibrations of the plates are studied in air and when submerged in a water tank to examine the effects of fluid loading on the plates. The experiments were also performed on similar homogeneous aluminum plates to illustrate the effects of anisotropy in the composites.

The analysis was performed with the experimental technique of Digital Speckle Pattern Interferometry (DSPI) which is like holographic interferometry with the exception that a video camera and digital image processor are used to collect and process the holographic images. DSPI provides full-field, non-intrusive, out-of-plane displacement measurements of vibrating structures, and produces mode shapes in the form of speckle correlation fringe patterns. In addition, the drive point mobilities of the plates were determined with the aid of a laser Doppler vibrometer.

The results of the experiments showed that the composites exhibited unpredictable modal behavior due to anisotropy in the plates. For this reason, DSPI proved to be an efficient technique for acquiring mode shapes. In addition, the use of vibrometry in conjunction with DSPI provided an accurate experimental modal analysis system.

TABLE OF CONTENTS

LIST OF FIGURES

LIST OF TABLES

CHAPTER 1

INTRODUCTION

The modal vibrations of composite structures can be much more complex than similar structures made of homogeneous materials such as metals. Unusual vibration patterns and additional resonances can exist due to the complex internal structure of a composite material. Furthermore, these non-classical modes are more difficult to predict by analytical techniques. Even more complex mode shapes may be demonstrated by the composites when vibrating in an underwater environment. Speckle pattern interferometry has proven to be an excellent vibration analysis technique especially for structures where non-classical vibration behavior is exhibited. This speckle technique was used in the work reported in this thesis for detailed investigation of composite plate vibrations.

1.1. Objectives

The primary objective of the work described in this thesis was to study the modal vibrations of composite plates in various situations. The natural frequencies and mode shapes of the plates were compared for the plates in air and underwater to investigate the effect of the fluid loading. In addition, the vibrations of the composites were compared with those of similar homogeneous aluminum plates to demonstrate the effect of the anisotropy in the composites.

Another objective of this research was to design, assemble, and assess a

Digital Speckle Pattern Interferometry (DSPI) system that could perform the described vibration analysis. DSPI evolved from holographic interferometry, and has several advantages over holographic interferometry and other modal analysis techniques when applied to structural vibration analysis. The advantage of DSPI over conventional holography is that it allows the user to isolate resonances of an object in real time since DSPI uses video to display interferometric fringe patterns. Individual resonant modes may be easily isolated by slowly sweeping through the excitation frequency range while observing the fringe patterns and the input force level. The time-consuming process of photographic film development required in time-average holography is unnecessary.

An advantage of DSPI over standard modal analysis techniques is that DSPI provides a nonintrusive, full-field measurement, and mass loading by transducers ceases to be a problem. DSPI is an excellent vibration analysis technique for modes with high spatial frequencies (short wavelengths) where standard modal analysis techniques may be more time consuming and limited by hardware and software capacity. Furthermore, modal analysis of submerged objects by standard methods presents additional difficulties, especially with hammer impulse excitation.

Preliminary research indicated that the design and construction of a DSPI system was a complicated and difficult process. Commercial systems are available, but are extremely expensive, especially if a great deal of system versatility is required. It was decided that a DSPI system should be assembled in the laboratory to gain an in-depth understanding of its operation and to reduce costs. Once the system was

assembled, it would be applied to the modal vibration analysis of the composite plates both in air and underwater.

1.2. Overview of DSPI

A brief overview of DSPI is presented to provide a general description of the basic principles of operation of this technique as well as its evolution and applications. A review of the most important literature published on this subject is also included in this overview.

1.2.1. Historical Perspective

Digital Speckle Pattern Interferometry has evolved from traditional holographic interferometry over the past quarter century. Holographic interferometry was first demonstrated by Powell and Stetson [1] in 1965. Subsequently, researchers realized that, with the development of modern electronics and compact video cameras, interferometric fringe patterns could be captured on video, processed electronically, and displayed on a television monitor. TV holography was initially proposed by Butters and Leendertz [2] among others in 1971, and later dubbed Electronic Speckle Pattern Interferometry (ESPI). The electronic processing in ESPI involves the high-pass filtering to remove optical noise components of the signal and full-wave rectification to improve fringe contrast. The filtering and rectification can be shown to be equivalent to the optical reconstruction process in holography [3].

Subsequent advances in modern technology brought about the development

of digital electronics. This allowed continuous signals to be discretized by analog-to-digital (A/D) converters, and processed in a digital form with image processing algorithms. This A/D conversion is directly applicable to video signals. The filtering and rectification of the signals are performed by digital image processing algorithms. When a digital image processor is utilized, the interferometric technique is often called Digital Speckle Pattern Interferometry (DSPI).

1.2.2. Basic Principles

DSPI incorporates the latest technology in lasers, optics and digital video image processing. It operates on the same principles as holographic interferometry with the exception that the holographic images are collected with a video camera rather than a photographic plate. Since the video camera and display equipment have much lower spatial resolution than photographic emulsion, the objective speckle must pass through a small aperture to produce a speckle size which is compatible with the video system.

A monochromatic laser beam is split into a reference beam and an object beam. The reference beam is spatially filtered and expanded onto the image plane of a video camera. The object beam is expanded and scattered from the object under study in the form of a speckle pattern. Speckle is the random intensity seen when laser light is scattered from an optically rough surface. Speckle is treated as noise in holography, but still carries the phase information about the wavefront needed in DSPI. This scattered light is then imaged through a small aperture onto

the video camera where it is combined with the reference beam. If the two beams are coherent and have the same polarization, they will interfere destructively or constructively depending on their relative phase. Phase changes introduced by out-of-plane motion of the object may be collected at the image plane of the camera. If the object is vibrating time-harmonically at a frequency much higher than the sampling rate of the camera, the speckle will correlate or decorrelate depending on the relative phase producing bright and dark fringes respectively.

The speckle correlation information collected by the video camera is sent to a digital image processor. The video signal is digitized and may be processed in real time to filter out noise, or stored in framestores for enhancement during post-processing.

There are several optical configurations which have been proposed to produce this type of interference. The assembly of the apparatus is tedious, but once the system is set up, it is easy to use and has a wide range of applications.

1.2.3. Applications

ESPI/DSPI is a powerful and versatile experimental technique with a virtually unlimited range of applications. It may be used in any situation where holographic interferometry would be used. The technique may be employed to study objects in any optically transparent medium with dimensions from millimeters to meters at ranges of up to several meters [4]. Furthermore, ESPI/DSPI may be operated in time-average, real time, or double exposure mode as in holography.

ESPI/DSPI has been used in the field of acoustics to study vibrations of loudspeakers [5], other electroacoustic transducers, and musical instruments [6]. In industry, the technique makes an excellent on-line inspection device, and has been used in the vibrational analysis of automobile bodies [7] and turbine blades [8]. ESPI has also been utilized in biomedical applications including the observation of the human ear drum, in vivo [9]. ESPI/DSPI is an excellent tool for non-destructive evaluation (NDE), and has been used to detect subsurface delamination flaws in laminated composite materials [10]. Holographic interferometry has also been used successfully to determine underwater plate dynamics by Croteau and Sheets in 1974 [11], but underwater experiments using ESPI/DSPI have not been reported in open literature.

The purpose of this thesis is to describe a Digital Speckle Pattern Interferometry (DSPI) system which was constructed as part of this research and to describe experiments performed with the device. Chapter 2 provides a detailed description of the system including its physical operating principles. Each component in the system is described and an assembly procedure is presented.

Chapter 3 includes a detailed description of the plate specimens under study and the experiments performed on the plates. The experiments included the determination of the drive point frequency response functions of the plates using laser Doppler vibrometry, and mode shape determination using DSPI. The results of the experimental determination of the natural frequencies and mode shapes of the plates in air and underwater are presented. The vibration characteristics of the

composite plates and aluminum plates are analyzed and compared to illustrate the effect of the fluid loading and anisotropy in the composites. The results are compared with theory where possible.

Conclusions about this research including a discussion of the results and evaluation of the DSPI system are presented in Chapter 4. Future work in this area is proposed and a brief summary of the work is outlined. The frequency response functions and DSPI results are incorporated in the appendices.

CHAPTER 2

DESCRIPTION OF DSPI SYSTEM

2.1. Operating Principles

The fundamental principles of operation of a DSPI system are considered in this section. The important physical properties of highly coherent laser light which make DSPI possible are explained. The most important properties include the behavior of two superimposed laser beams and, of course, the speckle effect. The optical arrangement required to properly superimpose two laser beams for the creation of interferometric fringe patterns is described. The time-average speckle pattern fringe function for vibration analysis is derived, and the video processing of the speckle pattern is discussed.

2.1.1. Properties of Laser Light

Laser theory and operation is fairly complicated and will not be discussed in this thesis, although the properties of laser light will be explained. Light Amplification by Stimulated Emission of Radiation (LASER) produces highly intense and coherent monochromatic electromagnetic radiation in the infrared, visible, or ultraviolet regions of the wavelength spectrum. These descriptors are investigated in this section.

Laser light is a sinusoidal electromagnetic wave. Its propagation is described

by the solution to the electromagnetic wave equation which may be derived from Maxwell's equations:

$$\frac{\partial^2 U}{\partial z^2} - \frac{1}{c^2}\frac{\partial^2 U}{\partial t^2} \qquad (1)$$

where z is the propagation direction, c is the speed of light, and U is the electric field intensity [12]. The solution to this equation may be written in the complex harmonic wave form:

$$U(z,t) - u_0 \exp i[2\pi ft - \phi(z)] \qquad (2)$$

where u_0 is the field intensity, f is the frequency of the wave and $\Phi(z)$ is the phase determined by the position in space. There are two solutions to the wave equation and equation (2) represents the positive-going wave.

The light wave has polarization and coherence. Coherence means that the wave will approximate a sine wave of fixed frequency for a distance known as the coherence length of the laser. The coherence time is the time during which the wave maintains its sinusoidal form [13]. During this time, the spatial and temporal phase of the wave has great importance as explained later. The polarization refers to the

directional variation in the electric field relative to the propagation direction. For instance, if the beam travels horizontally and the electric field oscillates in the vertical direction perpendicular to the propagation direction, the beam is said to be vertically plane polarized [13, p.7].

The superposition of two monochromatic light waves is clearly explained by Jones and Wykes [13, p.10]. Consider two coherent light waves with the same wavelength but with difference complex amplitudes given by the equations:

$$U_1 = u_1 \exp i(2\pi ft + \phi_1) \tag{3}$$

$$U_2 = u_2 \exp i(2\pi ft + \phi_2) \tag{4}$$

If these two waves are superimposed, they may be treated like phasors [12, p.21], and the total complex amplitude of the resulting wave is:

$$U_T = u_1 \exp i(2\pi ft + \phi_1) + u_2 \exp i(2\pi ft + \phi_2) \tag{5}$$

which may be written as:

$$U_T = (u_1 \exp i\phi_1 + u_2 \exp i\phi_2) \exp i 2\pi ft \qquad (6)$$

Since the intensity of a light wave is proportional to u^2 [12, p.3], the total intensity of the superimposed complex waves is obtained by multiplying the complex amplitude by its complex conjugate yielding the well known expression:

$$I_T = I_1 + I_2 + 2\sqrt{I_1 I_2} \, \cos(\phi_1 - \phi_2) \qquad (7)$$

In this equation, all intensity and phase terms may vary spatially in a plane.

When coherent laser light is used to illuminate an optically rough surface, the scattered light is perceived by the eye as "speckle." Laser speckle is seen as a spatially random light intensity distribution on a coherently illuminated surface whose random surface height variations (roughness) are on the order of the wavelength of the illuminating beam. Each point on the surface acts as a source, and the amplitude and phase of the scattered light at any point in space are determined by the coherent contributions from each point on the surface [13, p.52]. This type of scattering is based on Huygen's Principle and is called objective speckle [13, p.51]. Researchers noticed that speckle is sensitive to movement, i.e. an object under coherent illumination will appear to "twinkle" if the object is displaced slowly. This led to the

realization that, although the speckle appears to be random, the scattered wave still carries the wavefront phase information which is a measure of the geometry of the scattering surface [2, p.28].

Subjective or image-plane speckle is observed when an image of the scattering object is formed as with a lens. In this case, the size and spatial distribution of the speckle is determined by the limiting aperture of the imaging system, i.e., since the scattered light is passing through a lens and an aperture, the light will diffract onto the image plane changing the size of the speckle. This is discussed in detail by Jones and Wykes who define the average in-plane speckle size (diameter) as [13, p.56]:

$$d_{sp} \approx \frac{2.4\lambda v}{a} \qquad (8)$$

where λ is the wavelength of the light, v is the lens-to-image plane distance, and a is the diameter of the aperture. Obviously, as the size of the aperture is decreased, the speckle size increases and vice versa. This is significant because the size of the speckle may be varied to accomodate the resolution of the recording system.

If the coherently illuminated object is set into high- frequency time-harmonic vibration and viewed through an imaging system, the speckle will appear to blur together or "decorrelate" in regions of out-of-plane motion. Regions of no motion on the surface would be expected to scatter high-definition or "correlated" speckle.

Nodal regions on the surface would then appear as bright areas. The adjacent sinusoidally vibrating regions periodically reach the extremes in displacement where the surface is briefly stationary. In the positions where this stationary displacement is a multiple of the half-wavelength of the light, the speckle pattern is the same as the pattern for the stationary state except it will be less intense due to partial correlation of the speckle. If a reference state of the phase of the speckle pattern is superimposed on the image-plane speckle pattern, then the stationary peak displacements may be determined exactly [14].

2.1.2. Optical Arrangement

An optical system must be designed to properly combine the subjective speckle pattern of the object with the reference state so that out-of-plane displacements may be measured. The reference state may be in the form of a smooth reference beam of fixed uniform phase, or a speckle reference wave [15] which will not be considered here. The optical system must also be configured to meet the spatial resolution requirements of the recording system.

The most commonly used optical arrangement for this purpose, as discussed by Jones and Wykes, consists of a lens, variable viewing aperture (iris), and 45° beamsplitter [13, p.186]. The speckle scattered by the object is focused by the lens through the iris onto the image plane. The beamsplitter is positioned between the iris and image plane so that the object wave passes through the beamsplitter. The reference beam is expanded by a microscope objective and spatially filtered with a

25 μm pinhole and travels perpendicularly to the optical axis of the lens-aperture system. The reference wave is combined with the object wave by being reflected onto the optical axis with the beamsplitter. The object and reference waves will then be colinear between the beamsplitter and image plane. This configuration will be sensitive to out-of-plane displacements given by:

$$\Delta\phi(x,y,t) = \frac{4\pi d(x,y,t)}{\lambda} \qquad (9)$$

where $\Delta\Phi$ is the change in phase of the object wave at point (x,y) on the image plane due to the object displacement d, and λ is the wavelength of the light. This equation assumes that the angle between the illumination and viewing directions is very small so that the cosine of the angle is approximately equal to 1 [13, p.154]. Other configurations involve having the reference wave pass through a pinhole in the center of a mirror which reflects the subjective speckle pattern onto the image plane [13, p.185], or the use of fiber optics to combine the beams [16].

The spatial resolution of the resulting speckle pattern must be considered. Jones and Wykes show that for a linear variation of the relative phase of the combined wavefronts across the image plane, the object and reference beams must be "conjugate" [13, p.176]. This means that the beams appear from the image plane to diverge from the same point. Conjugacy is achieved by insuring that the reference

pinhole-to-beamsplitter distance is the same as the viewing aperture-to-beamsplitter distance. The aperture may then be adjusted to obtain a subjective speckle pattern resolvable by the recording system.

2.1.3. Time-Average Speckle Pattern Interferometry

The derivation of the time-average fringe function will assume that a subjective speckle pattern is combined with a uniform reference wave as described in the previous section. In addition, the object under study vibrates sinusoidally so that the out-of-plane displacement of the surface is given by:

$$d(x,y,t) = A(x,y) \sin(\omega t) \tag{10}$$

where A is the amplitude of the displacement of the surface and ω is the circular frequency of vibration. Using this in equation (9) and including the phase change term in equation (7), the instantaneous intensity of the speckle pattern across the image plane (x,y) with the object vibrating sinusoidally is given by:

$$I_T(t) = I_o + I_r + 2\sqrt{I_o\,I_r}\ \cos(\phi_o - \phi_r + \frac{4\pi A}{\lambda}\sin\omega t) \tag{11}$$

where the subscript o refers to the object beam and r refers to the reference beam. If the image is recorded during a time much greater than the period of vibration, the image will be time-averaged as described by the equation:

$$\langle I_T \rangle_\tau = I_o + I_r + 2\sqrt{I_o I_r} \quad \frac{1}{\tau} \int_0^\tau \cos(\phi_o - \phi_r + \frac{4\pi A}{\lambda}\sin\omega t)dt \tag{12}$$

The integral may be rewritten:

$$\frac{1}{\tau} \int_0^\tau \cos(\psi + \frac{4\pi A}{\lambda}\sin\omega t)dt \tag{13}$$

where $\Psi = \Phi_o - \Phi_r$. The solution to the integral may be shown to be [17]:

$$J_0(\frac{4\pi A}{\lambda}) \cos\psi \tag{14}$$

Substituting into Equation 12, the intensity of the resulting time-average speckle pattern is:

$$I = I_o + I_r + 2 \sqrt{I_o I_r} \, J_0 \left(\frac{4\pi A}{\lambda} \right) \cos\psi \qquad (15)$$

The phase term Ψ is the difference between the reference phase which may be varied, and the object phase which is susceptible to slowly-varying random phase changes due to instability in the optical components. The instability may result from extraneous vibrations, air currents, or slight thermal gradients.

Time-average DSPI is ideal for vibration analysis because nodal lines appear as zero-order bright fringes. Out-of-plane surface displacement amplitude is determined easily by counting higher-order fringes which occur to the sides of the bright fringes in the image plane. The main difficulty with this method is obtaining high-contrast fringe patterns which is determined by the recording system.

2.1.4. Video System

Interferometric speckle patterns may be collected by a video camera simply by placing the camera face at the image plane of the imaging system. Many video cameras use a charge coupling device (CCD) array to collect images. This consists of an array of photodetectors whose output voltage is proportional to the illuminating intensity. Video images are usually sampled as 512 X 512 pixels at 30 frames per second. The output signal from the camera is proportional to the expression in equation (15). The camera signal may be processed electronically or ser· to a digital

image processor, and then viewed on a television monitor. In either case, the video processing involves filtering out any noise in the image and increasing the dynamic range of the speckle pattern to improve the contrast and fringe visibility.

The first two terms of the expression will contain any optical noise as described by Creath [18] and should be subtracted out to obtain a high contrast time-average fringe function. Optical noise may be due to diffraction from dust particles on the optics or interference from high-order reflections of stray light. Subtraction techniques are described by Creath [18, p.296] and may be performed by real-time image processing algorithms.

One possible algorithm subtracts a static reference image from the live image. For this method to work, the reference beam must be reflected from a mirror which can be oscillated by a piezoelectric crystal. The reference image will contain only the noise terms if the image is captured while the mirror is driven at a high amplitude corresponding to a zero of the Bessel function and the object is at rest. This method is highly susceptible to the instability in the optics.

An alternative algorithm takes advantage of the instability by subtracting sequential frames and taking the magnitude of the difference. This is equivalent to high-pass filtering and rectification in ESPI, and the image reconstruction process in holography as described by Lokberg [3]. Since sequential frames will contain I_o and I_r these terms will be subtracted out and the brightness B of the resulting image on the monitor will be given by the expression:

$$B \propto 2\sqrt{I_o I_r} \ |\ J_0(\frac{4\pi A}{\lambda}) \ \cos\psi\ | \tag{16}$$

The absolute value of the cos Ψ term may vary slowly due to instabilities causing the image to fade in and out. This term will have a different value between 0 and 1 from frame to frame. The image should then be captured when this term is near a maximum to yield a high contrast fringe pattern. The captured single frame will be described by the equation:

$$B - K\ |\ J_0(\frac{4\pi A}{\lambda})| \tag{17}$$

where K is a positive constant. The fringe function is usually approximated by a squared zero-order Bessel function to be consistent with time-average holography. The squaring is often attributed to square-law rectification in ESPI [19] or square-law detection by the imaging array. In any case, the analysis of the fringe patterns is the same since only the argument of the function is of interest. A plot of the absolute value of the zero-order Bessel function is shown in shown in Figure 2.1. The interpretation of time-average fringe patterns using this equation is described in the following chapter.

2.1.5. Vibration Phase Determination Using DSPI

The phase of vibration may be determined by shifting the phase of the reference beam relative to the object wave. This technique is well known and will
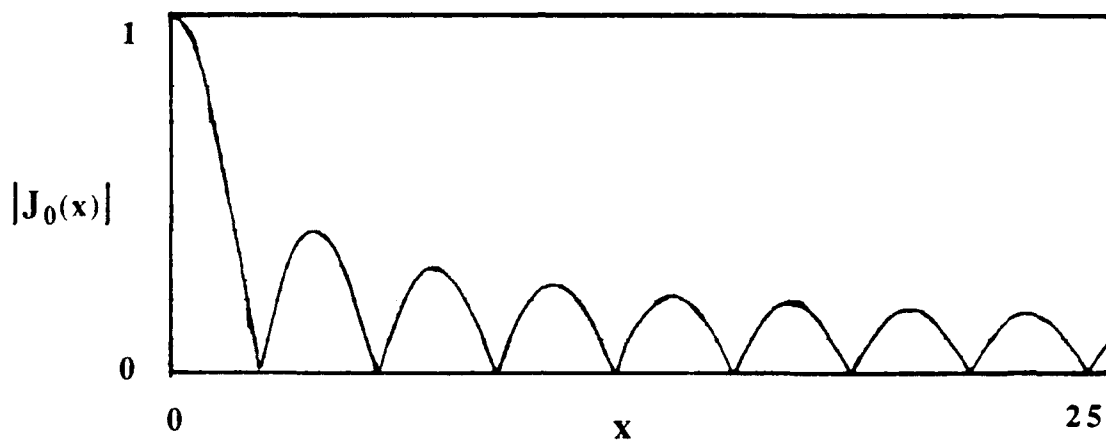
Figure 2.1:   Plot of absolute value of zero-order Bessel function

not be discussed in detail or used in this thesis. Reference phase shifting is performed easily in practice by reflecting the reference beam from an oscillating mirror surface. The mirror is excited at the same frequency as the object but with a different phase. By varying this phase, bright nodal fringes will appear where the vibration of the object is in phase with the mirror. A mathematically more complex fringe function is obtained with the argument of the Bessel function being a function of the displacement and phase of the mirror as well as the displacement and phase of the object [20]. The phase of vibration may also be determined by vibrating the

mirror at a slightly different frequency than the object. The image will appear to vibrate at the resulting beat frequency [21].

2.2. System Components

The DSPI system used in this study, which is illustrated in Figure 2.2, was assembled from commercially available components. A brief description of each component is provided in this section, and the assembly procedure of the components is listed in the following section. The elements of the DSPI system included the following:

Table Top: The laser and all optical components were mounted on a 4' x 12' Newport Research Series Table Top which has 1/4 - 20 holes tapped in an array on 1 inch centers. The Table Top was suspended by Newport's Pneumatic Vibration Isolation Support System for seismic vibration isolation.

Laser: The Coherent Innova 90-4 Argon Ion Laser was the backbone of the DSPI system. The 90-4 can continuously produce up to 2 watts of vertically polarized monochromatic light tuned to a wavelength of 5145 Å. An etalon was used in the laser to ensure extremely long coherence length.

DIGITAL SPECKLE PATTERN INTERFEROMETER

LEGEND

NDF - Neutral Density Filter
BC - Beam Combiner
CAM - CCD Camera
EMS - Electro-mechanical shaker
I   - Iris
M   - Mirror
OBJ - Object
PH - Pinholes (spatial filters)
PSM - Phase shifting mirror (PZT)
VBS - Variable beam splitter
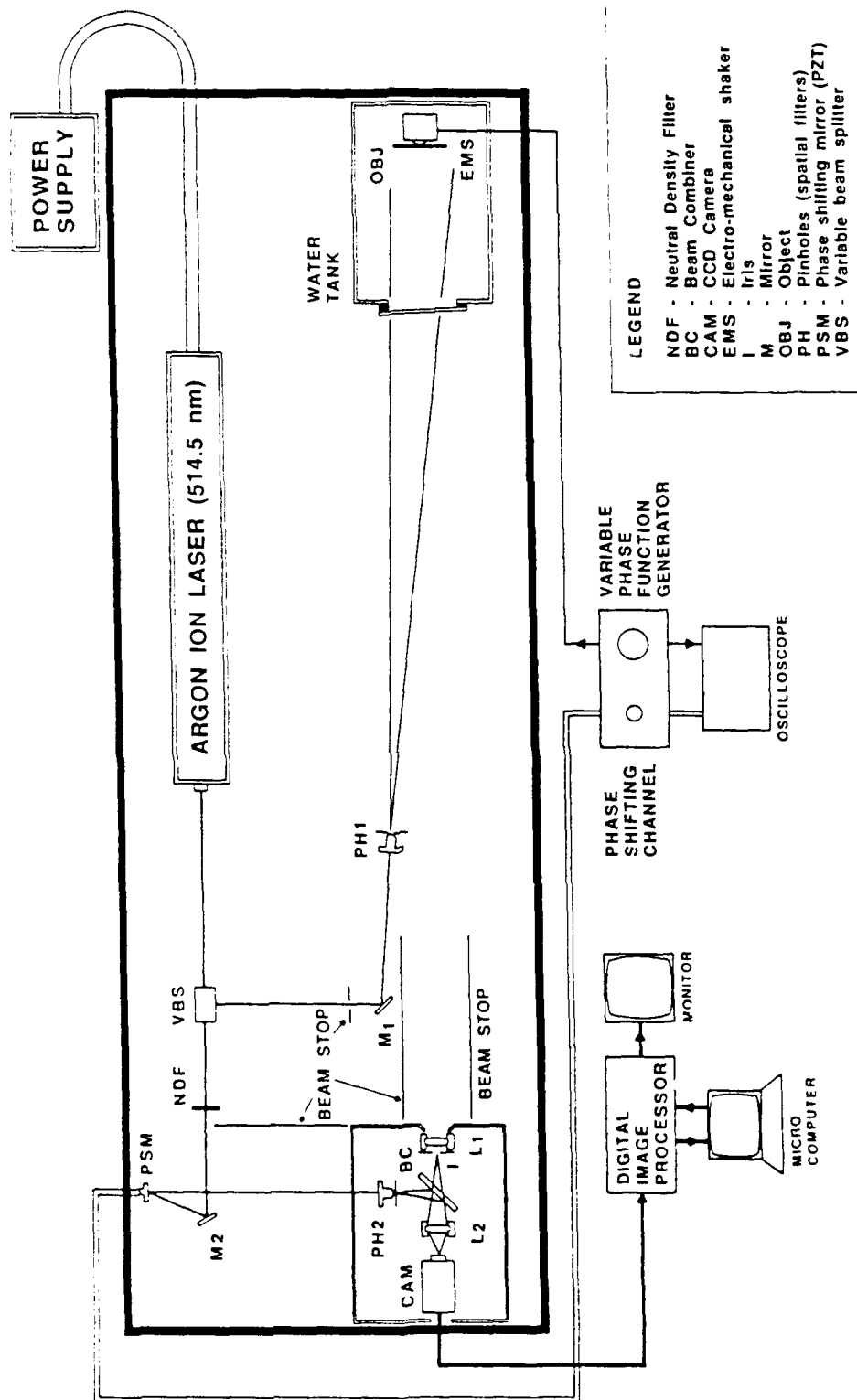
Figure 2.2:   Schematic of DSPI system

<u>Variable Beamsplitter (VBS)</u>: The output beam from the laser was split into the object and reference beam by a Newport 930 Variable Attenuator/Beamsplitter. The 930 uses a polarizing cube beamsplitter and half wave plates to maintain vertical polarization of the two beams. An adjustable half wave plate is used to vary the relative intensities of the beams.

<u>Phase Shifting Mirror (PSM)</u>: The small mirror, which was also supplied by Newport, was mounted on a PZT driver in a gimbal mount for easy positioning.

<u>Pinholes (PH)</u>: The Newport Model 910 Compact Spatial Filters were employed to expand and spatially filter the laser beams. The beam is expanded by a 10X microscope objective and filtered by a 10 to 25 micron pinhole. The alignment of the pinhole using the integral 5-axis adjustments is described in the Newport Catalog [22].

<u>Mirrors (M)</u>: The beams were diverted with 2 inch diameter mirrors mounted in gimbal mounts for fine adjustment.

<u>Neutral Density Filters (NDF)</u>: Melles Griot Neutral Density Filters were utilized to attenuate the reference beam as needed.

Lenses: Precision Computer-Optimized Achromatic Doublets from Melles

Griot were used as the imaging optics.

Beam Combiner (BC): A 4 inch Newport Quartz Broadband 50/50 Dielectric

Beamsplitter mounted in an Aerotech gimbal mount combined the

object and reference waves.

Video Camera (CAM): Images were collected at 30 frames per second by a

Sanyo VDC3860 CCTV video camera. The image device was a 2/3

inch diagonal frame transfer CCD with 800 (horizontal) by 490

(vertical) elements.

Image Processor: The MaxVision AT-1 image processing system was

provided by Datacube, Inc. The system contains A/D and D/A

converters for video I/O, a high-speed digital processor, and algorithms

written in the C Programming Language for real-time digital

image processing. The MaxVision system was controlled by a Dell

System 220 microcomputer which used a 80286 microprocessor.

Output Devices: The video output from the image processor was viewed on

a Sony Trinitron Color Video Monitor. Hard copy of the images was

provided by a Team Systems TP-6490 Video Printer. Video was also

recorded in real-time if necessary using a Panasonic AG-1950 Multi Function VCR.

Vibration Electronics: Objects were excited with a Bruel & Kjaer Type 4810 Mini Shaker (EMS) which has a 10 Newton sine peak force rating and frequency range of DC to 18 kHz. The drive signal was generated by a Hewlett Packard Model 203A Variable Phase Function Generator and amplified by a B & K Type 2706 Power Amplifier.

2.3. Assembly Procedure

A detailed description of the optical set-up used in DSPI is provided in this section. The basic optical arrangement was taken from Lokberg [23] and Stetson [24]. The schematic of the DSPI system which is illustrated in Figure 2.2 should be studied carefully before and used as a guide during the assembly of the device. Although the schematic is not to scale, it gives a general idea of the placement of the optical components on the table top. The location of the components is not critical since the laser beam is highly coherent and optical path lengths are variable. All optical components are supported on optical posts and stands so that their height above the table is adjustable. The stands may either be fastened directly to the table top with 1/4 - 20 cap screws or mounted on magnetic bases for easy placement. The CCD camera, lenses, and beam combiner were mounted on a 1 meter long Ealing

Triangular Optical Bench with Ealing Bench Carriers to facilitate adjustments of the optics.

Protective laser goggles should always be worn while the laser is in operation. A white index card may be used to see the beam through the goggles. A ruler and the array of holes on the table are useful for aligning the beams and positioning the optics. With these tools and a great deal of patience, the system may be assembled using the following procedure:

1) Turn on the laser, allow it to warm up, and tune it for maximum output. Level the laser with its adjustable feet such that the output beam is a fixed distance above the table.

2) Fasten the Variable Beam Splitter to the table about 1 to 2 feet in front of the laser so the holes are the same height above the table as the beam. The reference beam should pass through the VBS while the object beam exits the beamsplitter in the perpendicular direction. The relative intensities of the two beams may be varied as needed in the rest of the procedure.

3) Place the optical bench with the CCD camera, lenses, and beam combiner approximately in the position shown in the schematic. The bench should be aligned with a row of holes about 1 foot from the

edge of the table which will define the viewing direction of the camera. Placement of the camera and optics is described later.

4)   Place an object in front of the bench at the opposite end of the table. The center of the object should be at the same heigi· .. 'ove the table as the beam and on the same row of holes as the bench.

5)   Direct the object beam onto the center of the object with mirror M1. The mirror should be placed such that the angle between the illumination and viewing directions is minimum without obstructing the view. Position and align spatial filter PH1 in the object beam for uniform illumination of the object. Close the laser aperture.

6)   Fix the beam combiner to the optical bench wherever the reference beam will be reflected onto the combiner, usually about in the center. Provide enough room on the bench behind the BC for the camera and lens L2 to be moved for focusing purposes. The BC should be fixed at a 45 degree angle to the bench as shown in the schematic.

7)   Fasten the lens-iris combination a few inches in front of the BC according to the imaging requirements. For the 4 inch square plate experiments and an object distance of 2500 mm, a 160 mm focal length

doublet was chosen for L1 and placed with the aperture 80 mm in front of the BC.

8) Place lens L2 and CCD camera onto the optical bench (a 300 mm focal length doublet was used for L2). Connect the camera output to the image processor input with the appropriate BNC cable and turn on the microcomputer and video monitor. Load the MaxVision software by entering "MV1" at the DOS prompt.

9) Open the laser aperture and "Initialize MaxVision" to view the image of the object on the monitor. Move L2 along the optical bench to attain the desired object magnification, and adjust the position of the CCD camera to focus the object.

10) Tape a white card across the front of the camera, and open the iris for maximum aperture so that a clear image of the object appears on the card. Using the holes in the table top, find a line perpendicular to the optical bench at the center of the beam combiner. Place the PSM on this line as shown in the schematic with the center of the mirror at the same height above the table as the laser beam.

11) Divert the reference beam onto the PSM with mirror M2. The angle

between the incident and reflected beams at the PSM should be as small as possible. Adjust the gimbal mounts on the PSM and M2 so that the reference beam follows the path shown in the schematic, and a spot of light is centered on the image of the object on the card.

12) Install and adjust the spatial filter PH2 with a 25 μm pinhole so that the uniform reference beam is concentric with the image on the card. The pinhole must be the same distance from the center of the BC as the imaging iris to satisfy the conjugacy requirement.

13) Adjust the VBS for minimum intensity of the reference beam, remove the card and observe the image on the monitor. Decrease the imaging aperture and install the Neutral Density Filter required to attenuate the reference beam so that the image on the monitor is not "washed out".

14) Carefully observe the object and reference images on the monitor by blocking one and viewing the other. The object should be speckled and in focus, and the reference should be approximately uniform although some optical noise from diffraction fringes will be present. With both beams unblocked, the image on the monitor should appear to slowly flicker due to the instability in the optical components. If the

flickering is not seen, gradually adjust the gimbal mounting on the BC until it is seen indicating that the beams are coherent at the image plane of the camera and time-average speckle patterns may be obtained.

The assembly procedure requires patience and practice, and usually takes about 3 hours. Once it is set up, the measurement procedure for time-average vibration analysis may be easily carried out as described in the following chapter.

CHAPTER 3

EXPERIMENTAL VIBRATION ANALYSIS

3.1. Description of Specimens

Four different square plates were considered in this study for a total of 16 cases. The vibrations of two laminated composite plates with different thicknesses were compared with those of two homogeneous aluminum plates with identical exterior dimensions. Mode shapes were observed both in air and underwater with the plates completely free on the edges and with the plates clamped on one edge.

3.1.1. Composite plates

Two square fiber reinforced polymer (FRP) composite plates were the primary subjects of this analysis. The plates were composed of carbon fiber sheets laminated in a polyether etherketone (PEEK) resin. The fiber direction lay-up was $0°$, $+ 45°$, $- 45°$, $+ 90°$, and symmetric about the midplane of the plates. One of the square plates was 48 layers thick (0.25 inch total thickness) and 3.83 inches on each side; the other plate was 16 layers thick (0.08 inch total thickness) and 4.00 inches on each side. This configuration yielded a quasi-isotropic composite material in bending with an average elastic modulus of 9.526 X 10^6 psi (66 GPa) for the 48-layer plate and 7.571 X 10^6 psi (52 GPa) for the 16-layer plate, and Poisson's ratio of 0.32. The

laminate properties were computed by the COMPLY program [25]. The thick plate had a mass of 98.56 grams and the thin plate had a mass of 33.94 grams.

3.1.2. Homogeneous plates

Homogeneous aluminum plates were analyzed to compare with the composites to show the effects of anisotropy on the vibrations of the composites. Aluminum has an elastic modulus of about 30 X 10^6 psi (70 GPa) and Poisson's ratio of 0.33. These plates had exactly the same exterior dimensions as the composites. The 0.25 inch thick aluminum plate had a mass of 169.67 grams and the 0.08 inch thick plate had a mass of 57.35 grams.

3.1.3. Boundary and Loading Conditions

The four plates described above were each analyzed in four different situations. These conditions were chosen because theoretical natural frequencies and mode shapes for the homogeneous cases were readily available. Comparison of experimental results with theory would then be uncomplicated.

A waterproof container for the electrodynamic shaker used to excite the plates was constructed for the underwater experiments. The container consisted of a 4 inch diameter PVC pipe which was threaded on the inside, and two aluminum end caps screwed into each end of the pipe. The shaker was fastened at the center of the rear end cap inside the pipe, and a hole was drilled in the center of the other cap to allow a stinger or extention to be attached to the shaker.

The plates were first analyzed in a completely free edge condition with excitation at the center. A small nut was attached to the center of each plate with contact cement and threaded onto the force gage which provided support and excitation at the same point. The force transducer was attached to the shaker through a nylon extension which was sealed to prevent water from reaching the shaker. The extension/force gage assembly had a total mass of 36.73 grams. The fixture used in the experiments for the free condition is pictured in Figure 3.1.

Further analysis was performed with the plates in a cantilever configuration. The plates were clamped on one edge in an ordinary bench vise so that the plates then had an aspect ratio of 0.8, i.e. 20% of the square plate was actually clamped in the vise jaws. The cantilever plates were then driven at an upper corner by the force gage which was connected to the shaker through a sealed nylon stinger. The plates were driven at the corner because none of the theoretical modes had a node at that location. The stinger/force gage asssembly had a total mass of 36.48 grams. The fixture to create the cantilever condition is pictured in Figure 3.2.

Each of these cases was then studied both in air and underwater. The specimens and fixtures were placed in a transparent plexiglas water tank which was filled with distilled water for the underwater experiments. The water tank was 1 by 2 feet in area and about 1.5 feet deep. The viewing window was mounted at an angle on the side of the tank to reflect the laser beam away from the optics. The underwater configuration is pictured in Figure 3.3.
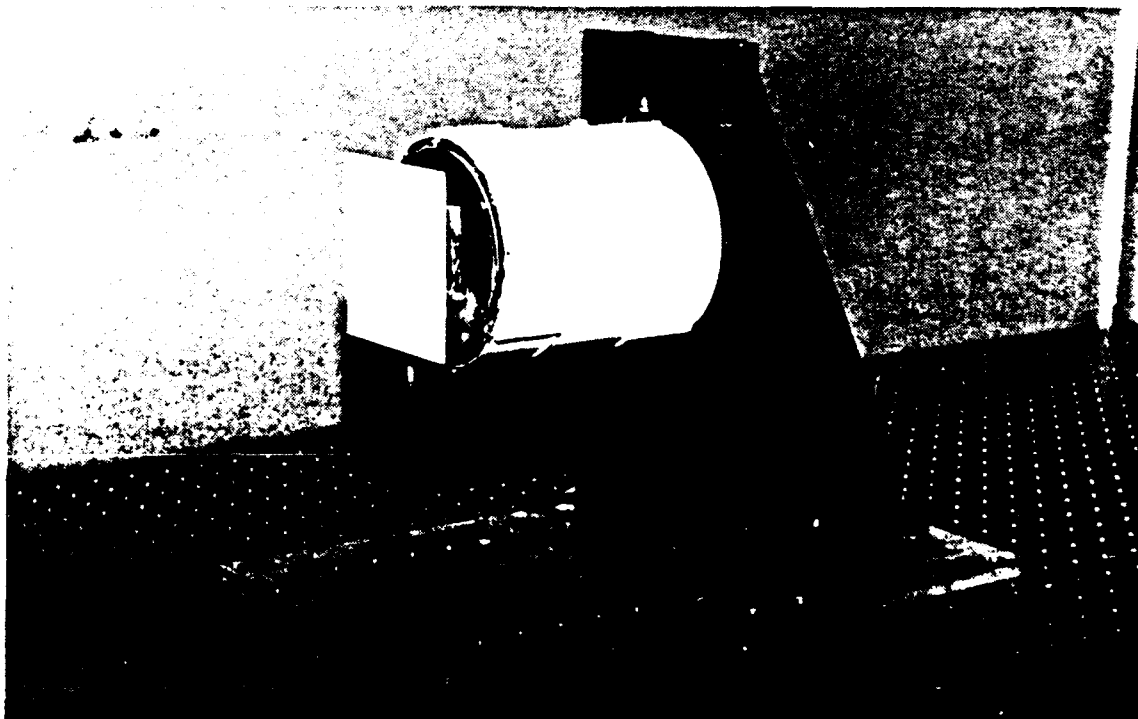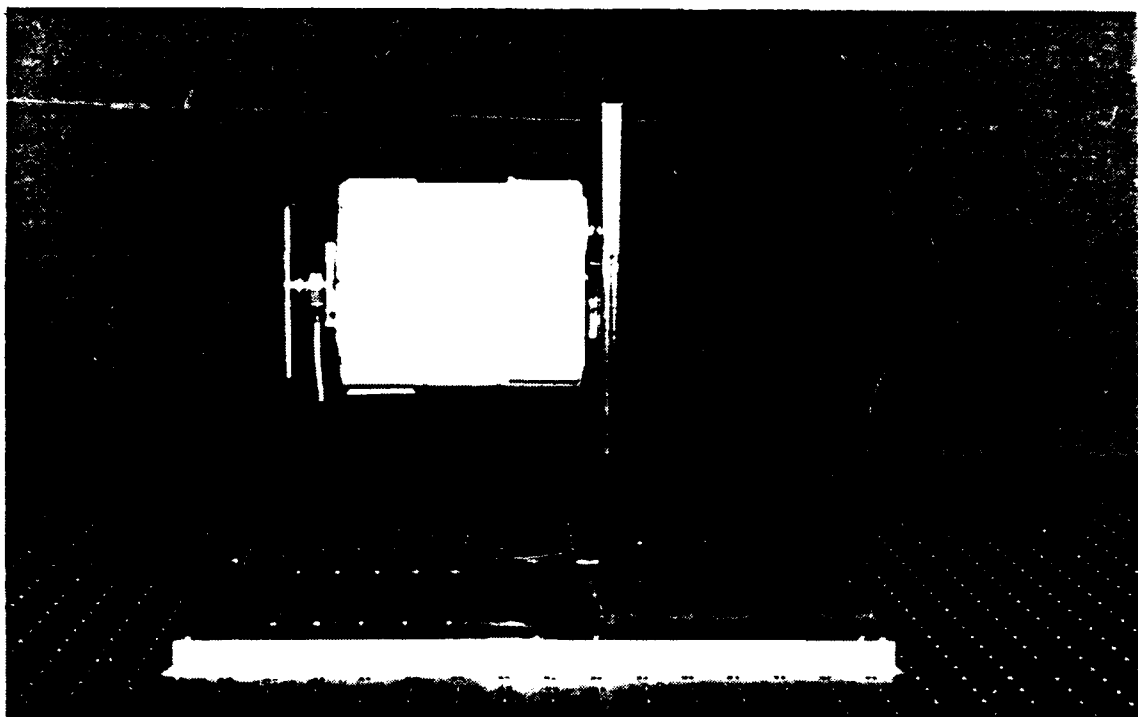
Figure 3.1:   Side and oblique views of fixture for free condition
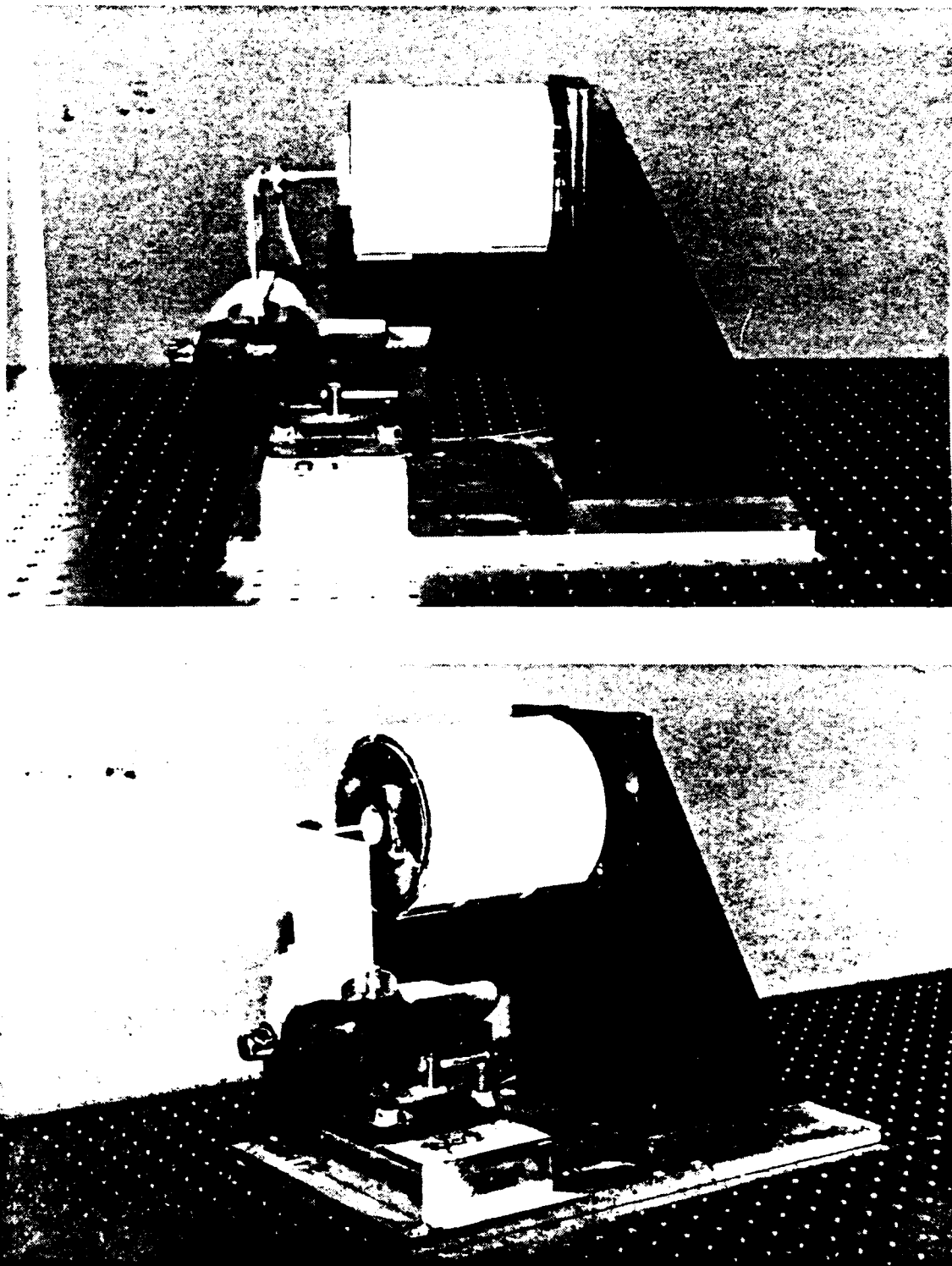
Figure 3.2:   Side and oblique views of fixture for cantilever condition

36
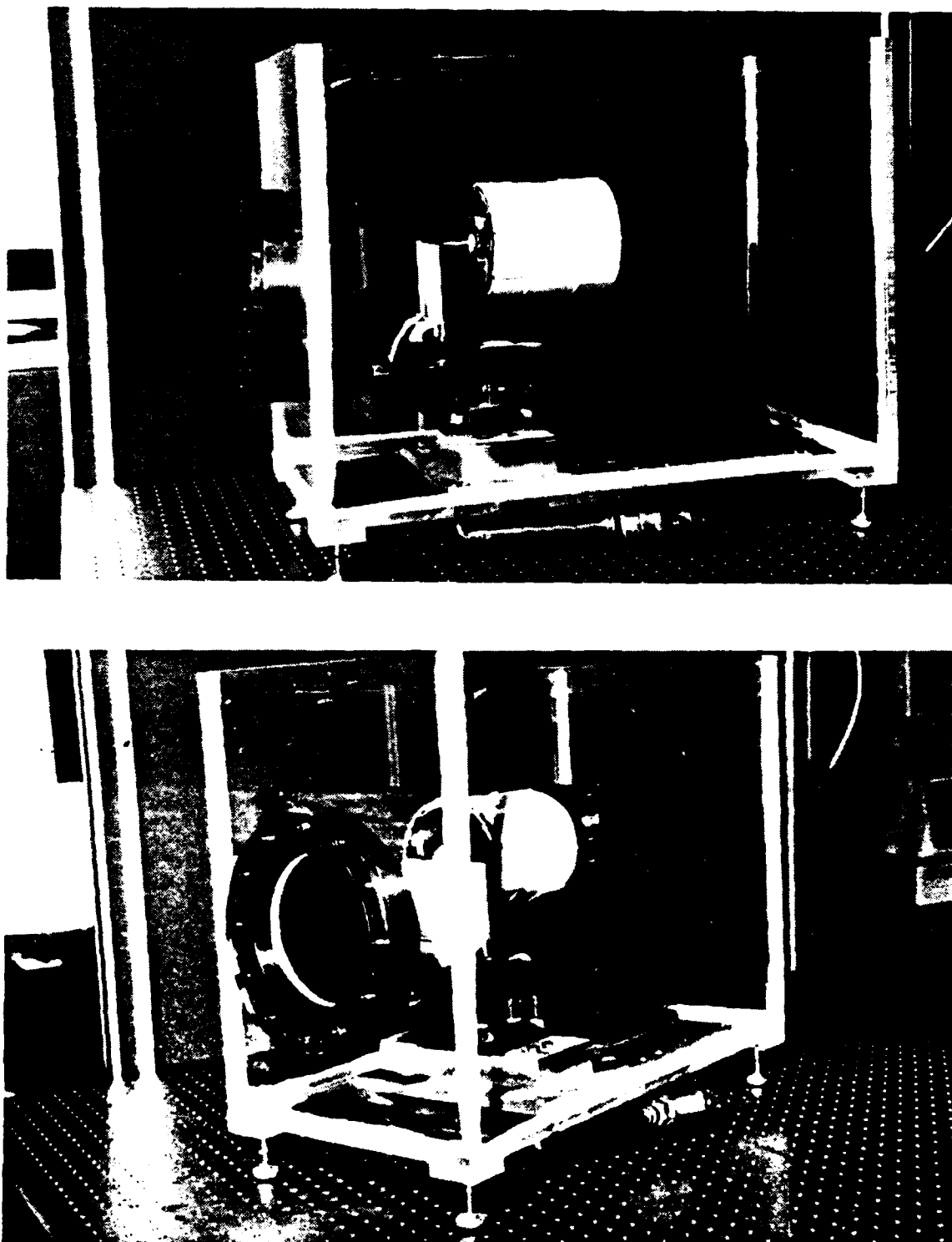
Figure 3.3: Side and oblique views of set-up for underwater experiments

3.2. Description of Experiments

The theoretical calculations, and experimental procedures for determination of frequency response functions, natural frequencies, and mode shapes are described in this section.

3.2.1. Determination of Theoretical Modes

The theoretical natural frequencies corresponding to classical mode shapes of homogeneous plates were calculated as benchmark values. There is no closed-form solution of the plate equation for the free and cantilever boundary conditions. Therefore, the natural frequencies and mode shapes were taken from Leissa [26], who determined the modes with numerical solutions of the plate equation. He defines a frequency parameter λ which given by the expression:

$$\lambda = \omega a^2 \sqrt{\rho/D} \tag{18}$$

where ω is the circular frequency, a is the side dimension of the plate, ρ is the mass per unit area of the plate, and D is the flexural rigidity of the plate. This is given by the expression:

$$D = \frac{Eh^3}{12(1-v^2)} \tag{19}$$

where E is Young's modulus, h is the thickness of the plate, and v is Poisson's ratio.

The values of λ for normal resonant modes are given by Leissa for completely free and cantilever plates. The values of D, ρ, and a were substituted into the above equation and solved for ω. Division by 2π then gives the natural frequency corresponding to the given mode shape. The first five frequency parameters and mode shapes for a completely free square plate are presented in Figure 3.4. These are for modes which are symmetric about the coordinate axes and diagonals, and have no nodal lines at the center.

The first nine frequency parameters from Leissa for cantilever plates with various aspect ratios is shown in Table 3.1. Leissa indicates that the order in which the mode shapes occur is dependent on the aspect ratio of the plate [26, p.79]. An aspect ratio of 0.8 was used in this analysis.

Leissa also presents experimentally determined nodal patterns for a cantilever plate with an aspect ratio of 0.8. These are shown in Figure 3.5.

A dense fluid medium generally has the effect of adding mass and damping to a submerged structure. The added mass will decrease the natural frequencies of vibration assuming it does not affect the mode shape. Blevins [27] presents simple equations for approximating the added mass to the free and cantilever plates due to fluid loading. These equations are generally functions of the plate geometry, boundary conditions, mode number, and the density of the fluid medium. An approximation of the added mass for a free square plate with one side exposed to the
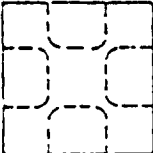
39

Nodal pattern	$\omega a^2\sqrt{\rho/D}$
	24. 2702
	63. 6870
	122. 4449
	168. 4888
	299. 9325

Figure 3.4: Frequency parameters and mode shapes for a completely free square plate (Leissa, p. 104)

Table 3.1:   Frequency parameters for rectangular cantilever plates (Leissa, p. 82)

TABLE 4.51.—*Frequency Parameters* $\lambda = \omega a^2 \sqrt{\rho/D}$ *and* $\lambda^* = \omega b^2 \sqrt{\rho/D}$ *for Symmetric Modes of a Rectangular Cantilever Plate;* $\nu = 0.3$

Aspect ratio	λ and λ^* for mode—				
	1	2	3	4	5
a/b	λ				
1.00	3.472	21.29	27.2	54.3	61.3
0.95	3.474	21.13	25.3	51.8	61.2
0.90	3.476	20.74	23.7	49.2	61.2
0.85	3.477	19.85	22.7	46.9	61.1
0.80	3.479	18.49	22.2	44.5	61.1
0.75	3.481	16.98	22.1	42.1	61.1
0.70	3.484	15.48	22.0	40.0	60.3
0.65	3.486	14.06	21.9	37.9	54.0
0.60	3.488	12.68	21.9	35.7	46.7
0.55	3.491	11.41	21.9	33.7	40.1
0.50	3.493	10.22	21.9	31.5	34.1
0.45	3.496	9.13	21.8	27.6	30.7
0.40	3.498	8.11	21.5	22.0	28.8
0.35	3.501	7.18	18.3	21.9	27.2
0.30	3.503	6.32	14.52	21.4	25.8
0.25	3.506	5.57	11.31	15.3	-----
0.20	3.508	4.85	8.65	-------	------
0.15	3.511	4.28	6.5	-------	------
0.10	-------	-------	-------	-------	------
0.05	-------	-------	-------	-------	------
0.00	3.5160	-------	-------	-------	------

TABLE 4.52.—*Frequency Parameters* $\lambda = \omega a^2 \sqrt{\rho/D}$ *and* $\lambda^* = \omega b^2 \sqrt{\rho/D}$ *for Antisymmetric Modes of a Rectangular Cantilever Plate;* $\nu = 0.3$

Aspect ratio	λ and λ^* for mode—			
	1	2	3	4
a/b	λ			
1.00	8.55	31.1	64.2	71.1
0.95	8.23	30.3	58.6	69.8
0.90	7.92	29.5	53.2	68.7
0.85	7.60	28.7	48.0	67.7
0.80	7.27	28.0	43.0	66.6
0.75	6.96	27.2	38.5	64.1
0.70	6.63	26.5	34.1	59.8
0.65	6.32	25.7	30.3	55.4
0.60	6.00	24.4	27.2	51.1
0.55	5.68	22.0	25.6	47.1
0.50	5.38	19.0	24.8	43.2
0.45	5.07	16.4	24.1	39.6
0.40	4.79	13.8	23.6	34.6
0.35	4.51	11.5	23.1	27.7
0.30	4.26	9.62	21.0	23.2
0.25	4.04	7.91	15.8	--------
0.20	3.85	6.42	11.58	--------
0.15	3.70	5.20	--------	--------
0.10	3.64	--------	--------	--------
0.05	--------	--------	--------	--------
0	--------	--------	--------	--------

MODES 1(0/0)   2(1/0)   3(2/0)

4(0/1)   5(1/1)   6(3/0)
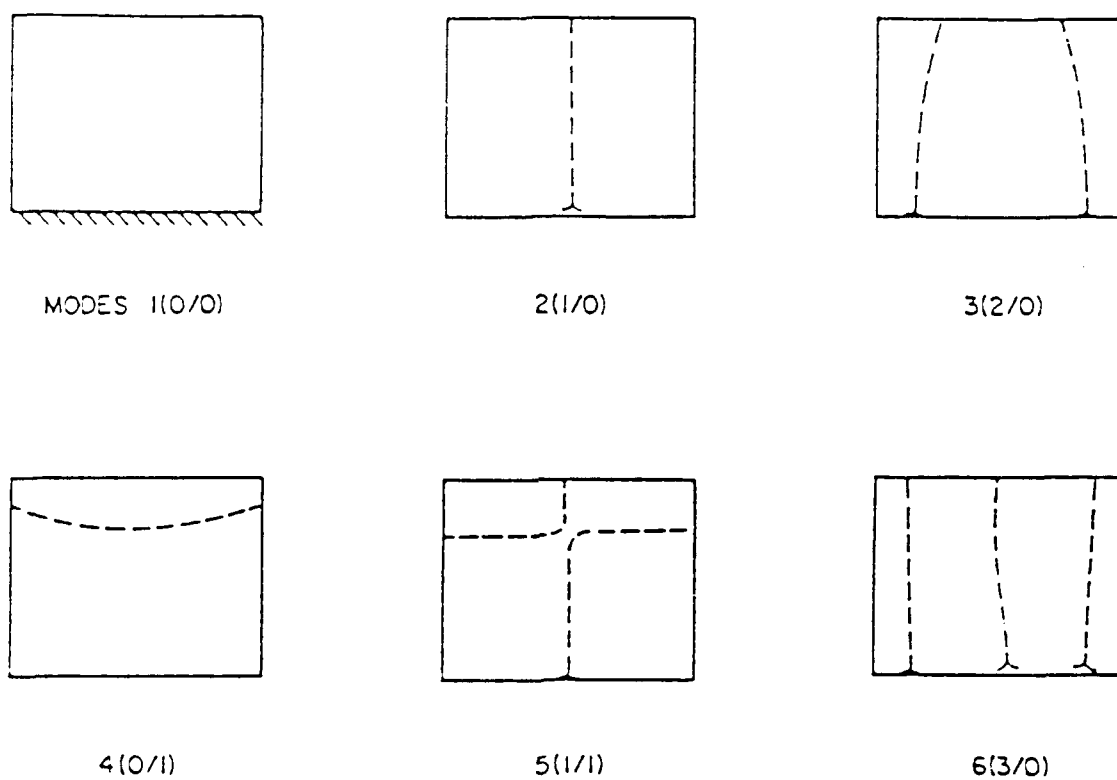
Figure 3.5:   Experimentally determined nodal patterns for   rectangular cantilever
               plate with 0.8 aspect ratio (Leissa, p. 85)

fluid is given by Blevins as [27, p.405]:

$$M_A \approx 0.579 \frac{\pi}{4} \rho_o a^3 \tag{20}$$

where ρ_o is the fluid density, and a is the plate side dimension. This mass term is simply doubled if the plate is loaded on both sides. For the cantilever plate, the added mass may be approximated to be [27, p.416]:

$$M_A \approx \rho_o a b^2 \tag{21}$$

where a is the length of the plate and b is the width being clamped.

The natural frequencies of the submerged plates may be approximated using those determined for the plates in air based on the fact that the natural frequency is inversely proportional to the square root of the mass. This effect of the added mass on natural frequency is expressed approximately by Blevins as [27, p.413]:

$$f_{n_{water}} \approx (1 + \frac{M_A}{m})^{-1/2} f_{n_{air}} \tag{22}$$

where m is the mass of the plate and f_n is the natural frequency. This equation does not account for the effect of mode shape and hydrodynamic short-circuiting. Leibowitz presents a correction for this using the Feit-Junger Method [28] by dividing the added mass term by the factor:

$$h \sqrt{k_m^2 + k_n^2 - k^2} \qquad (23)$$

where k_m and k_n are the plate modal wavenumbers, k is the acoustic wavenumber and h is the thickness of the plate. This correction factor is given for a simply supported plate, but provides an adequate approximation for the plates in this study. The results of the calculations of theoretical natural frequencies are presented in section 3.3.3.

3.2.2. Determination of Drive Point Mobilities

The drive point mobility of a structure is defined as the ratio of drive point velocity to input driving force as a function of frequency. This is the inverse of the mechanical impedance and is usually measured in dB relative to some convenient value. Mobility is a convenient quantity to study because resonances are indicated by maxima in the curves and a 180° shift in the phase. The peaks result from the fact that a minimum input force is required to excite the structure at resonance.

The velocity at the drive point was measured with a laser Doppler vibrometer which was manufactured by DANTEC Electronik of Denmark. The vibrometer contains a laser light source, and sophisticated optics and electronics which determine the out-of-plane velocity of a point on a surface. A low power Helium-Neon laser beam is focused onto the point of interest on the structure. The beam is reflected back into the vibrometer and collected by the optics where the Doppler shift frequency is detected. If the point of measurement is moving with some velocity V, then the Doppler shift frequency f_D of the r lected light is given by:

$$f_D = \frac{2\mu V}{\lambda} \tag{24}$$

where λ is the wavelength of the laser light, and μ is the correction factor for the index of refraction of the ambient medium. This shift frequency signal is sent to the Frequency Shifter/Doppler Frequency Tracker for processing into a velocity signal.

A schematic of the experimental set-up for the frequency response function measurements is illustrated in Figure 3.6. The plates were fixtured and driven by the shaker-stinger-force gauge assembly described in section 3.1.3 for all 16 cases.

For these measurements, the plates were excited with a broadband random noise signal which was generated by the Bruel & Kjaer Type 2032 Dual Channel Signal Analyzer. A broadband input was used to excite all the modes in the
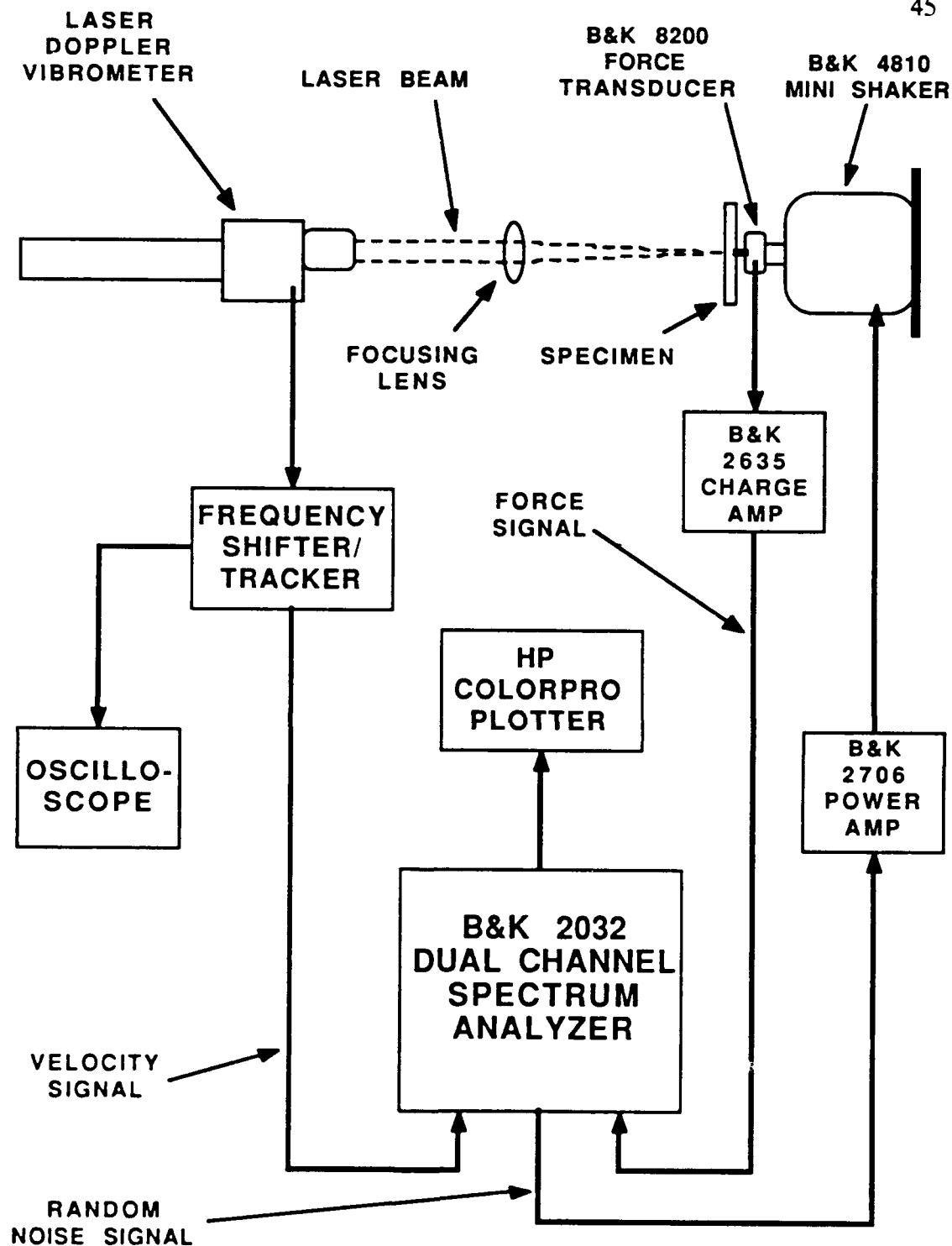
Figure 3.6: Experimental set-up for frequency response function measurements

frequency range of the interest. The force was measured by the force transducer at the drive point and the velocity was measured at the drive point by a laser Doppler vibrometer. The mobility curves were then computed by the signal analyzer, and the magnitude and phase of the frequency response functions were recorded.

Peaks in the curves and phase shifts were used to confirm the resonance frequencies determined with the DSPI system.

3.2.3. Experimental Procedure for Obtaining Modes Using DSPI

The DSPI system was used to determine the mode shapes at the corresponding measured resonance frequencies. The plates were fixtured for the free and cantilever cases, and submerged in water as described in section 3.1.3. The plates were driven with a sinusoidal signal from the HP function generator. The signal was amplified by a B&K 2706 Power Amplifier and input to the B&K 4810 Mini Shaker.

The B&K 8200 Force Transducer with a charge sensitivity of 4.07 pC/N was used to measure the driving force. The force signal was amplified by the B&K 2635 Charge Amplifier which was set for an output of 1 V/N, and sent to the WAVEPAK Waveform Analysis Package. WAVEPAK utilizes hardware which digitizes the input time signal and stores the data where the software can access it. The software can simulate a digital storage oscilloscope or act as an FFT analyzer. The force signal was observed using the oscilloscope program. A single snapshot of the signal may be stored so that the frequency and amplitude of the input force was easily

determined using the WAVEPAK cursor.

A digital multimeter was attached at the output terminals of the power amplifier so that the voltage and frequency of the input signal were readily displayed. Resonances in the plates were located by sweeping through the excitation frequency from about 500 Hz to 10 kHz, observing the force signal on WAVEPAK, and listening to the response of the plate. The mode shapes and natural frequencies of the plates were isolated using the DSPI system and the following procedure:

1) Turn on the laser and allow it to warm up. Always use protective goggles when operating the laser. Also turn on the microcomputer, image processor, and monitor. Type MV1 to access the MaxVision program Primary Menu.

2) Place the object under study at the appropriate distance from the imaging optics as shown in the system schematic (Figure 2.2). The center of the object should be on the same axis as the imaging lenses and camera.

3) If necessary, redirect the object beam onto the center of the object using mirror M1. Insert the spatial filter PH1 into the beam and adjust it so that the expanding beam evenly illuminates the object.

4) With the camera and image processor on, choose Initialize MaxVision in the Primary Menu to obtain a live video image on the monitor. Move the camera

or lens L2 along the optical bench until the proper magnification and focus of the object is viewed on the monitor.

5) Choose the Demonstration Menu from the MaxVision Primary Menu and then the Magnitude of Live TPC algorithm. Set the x and y offsets to zero with continuous elapse time. Without excitation, the image of the object speckle should appear to have uniform illumination, but fade in and out on the monitor.

6) Turn on the function generator and set the frequency below 500 Hz. Slowly increase the gain on the power amp until interferometric fringes are seen on the monitor. The gain will need to be adjusted according to the excitation frequency to obtain fringes which are easily distinguishable by eye.

7) Isolate resonances by slowly increasing the frequency of excitation, observe the behavior of the input force signal, examine the fringe pattern on the monitor, and listen to the response of the plate. Resonance is best indicated by a drastic decrease in the input force for a constant amplitude signal from the generator.

8) When a resonance is located, adjust the gain of the input signal until 5 or 6 secondary fringes are seen about the bright nodal fringes. Freeze the image

when the fringe contrast is a maximum. This is sometimes difficult due to the optical instabilities and the algorithm may need to be repeated. Record the frequency and amplitude of the input signal, and the amplitude of the force signal.

9) Perform any postprocessing on the image with the image processor and save it using the Image Management Menu. A simple image enhancement may be achieved by multiplying the image by a constant value to raise the mean value of the pixels. Print the image with the video printer if desired.

3.3. Experimental Results

The results of the experimental determination of the resonance frequencies and mode shapes of the plates are discussed in this section. The mobility curves are presented in Appendix A and the interferometric mode shapes from DSPI are compiled in Appendix B. The natural frequencies and related data are tabulated herein for ease of comparison.

3.3.1. Drive Point Mobility Results

The results of the drive point mobility measurements using laser Doppler vibrometry are presented in Appendix A. The boundary and loading condition, and

frequency range for each case is specified. The resonance frequencies and mobility levels extracted from the curves are presented in section 3.3.3.

3.3.2. Mode Shapes Determined by DSPI

The mode shapes of the plates which were obtained with the DSPI system are compiled in Appendix B. The boundary and loading conditions and frequency of vibration for each mode is indicated. The resonance frequencies and input force levels are also tabulated in section 3.3.3 for easy comparison with theoretical data.

3.3.3. Natural Frequency Results

The natural resonance frequencies which were calculated from theory, and determined experimentally are tabulated in this section. The theoretical frequencies may be compared with the natural frequencies determined from the frequency response function (FRF) measurements and the DSPI experiments. The drive point mobility level from the vibrometer measurements and input force amplitude from the DSPI experiments for each mode is also presented. The force is measured in Newtons, and the mobility levels are measured in dB relative to 0.003164 m/sec/N in air and 0.004208 m/sec/N in water. The first value for air comes from the velocity calibration factor from the frequency shifter of the vibrometer, and the second value is corrected for the index of refraction of water.

Table 3.2 shows the results for the 0.25-inch-thick plates in air with the free boundary condition. The aluminum plates are abbreviated Al in the tables and Co

for the composites. The frequency response functions are shown in Appendix A. The corresponding mode shapes are presented in Appendix B. In these figures, the 0° fiber direction is vertical for the composite.

Table 3.2:   Experimental results for free 0.25" plates in air

PLATE	MODE	THEO. FREQ.	FRF FREQ.	DSPI FREQ.	MOBIL. LEVEL	INPUT FORCE
0.25 Al	1 (0,2)	3946 Hz	3912 Hz	3912 Hz	4.0 dB	0.376 N
0.25 Co	1		3592	3592	-4.7	0.535
0.25 Co	2		4312	4314	10.2	0.406

Table 3.3 shows the results for the 0.08 inch thick plates in air with the free boundary condition. The mobility functions are presented in Appendix A. The corresponding mode shapes are presented in Appendix B. The 0° fiber direction is vertical for the composite in these figures.

The results of the 0.25 inch thick plates vibrating underwater with the free boundary condition are presented in Table 3.4. The mobility curves are given in Appendix A. The corresponding mode shapes determined by DSPI are presented in Appendix B. The 0° fiber direction is again vertical for the composite.

Table 3.3: Experimental results for free 0.08" plates in air

PLATE	MODE	THEO. FREQ.	FRF FREQ.	DSPI FREQ.	MOBIL. LEVEL	INPUT FORCE
0.08 Al	1 (0,2)	1176 Hz	1088 Hz	1089 Hz	20.2 dB	0.020 N
0.08 Al	2 (2,2)	3087	2784	2788	15.3	0.027
0.08 Al	3 (0,4)	5935	5280	5281	17.8	0.087
0.08 Al	4 (2,4)	8167	7336	7335	9.3	0.112
0.08 Co	1		928	921	12.4	0.006
0.08 Co	2		1240	1240	20.4	0.023
0.08 Co	3		2832	2819	18.4	0.048
0.08 Co	4		4984	4972	14.7	0.113
0.08 Co	5		6304	6304	8.7	0.192
0.08 Co	6		8392	8392	-5.4	0.356

Table 3.4: Experimental results for free 0.25" plates underwater

PLATE	MODE	THEO. FREQ.	FRF FREQ.	DSPI FREQ.	MOBIL. LEVEL	INPUT FORCE
0.25 Al	1 (0,2)	2838 Hz	2824 Hz	2837 Hz	2.7 dB	0.782 N
0.25 Al	2 (2,2)	7002	7368	7367	-2.6	0.841
0.25 Co	1		2168	2171	-15.9	0.662
0.25 Co	2		2704	2695	1.9	0.381
0.25 Co	3		6528	6525	-6.7	1.850

The results of the 0.08-inch-thick plates vibrating underwater with the free boundary condition are given in Table 3.5. The mobility functions are presented in Appendix A. The corresponding mode shapes determined by DSPI are shown in Appendix B. The 0° fiber direction is vertical for the composite in these figures.

Table 3.6 shows the results of the 0.25 inch thick plates vibrating in air with the cantilever boundary condition. The frequency response functions are shown in Appendix A. The corresponding mode shapes are presented in Appendix B. In these figures, the 0° fiber direction is horizontal. The clamp is at the bottom and the excitation point is at the upper left corner.

The results of the 0.08 inch thick plates in the cantilever condition vibrating in air are shown in Table 3.7. The mobility curves are presented in Appendix A. The corresponding mode shapes are presented in Appendix B. The 0° fiber direction for the composite is vertical. The clamp is at the bottom and the excitation point is at the upper left corner.

Table 3.5: Experimental results for free 0.08" plates underwater

PLATE	MODE	THEO. FREQ.	FRF FREQ.	DSPI FREQ.	MOBIL. LEVEL	INPUT FORCE
0.08 Al	1 (0,2)	824 Hz	560 Hz	561 Hz	9.4 dB	0.012 N
0.08 Al	2 (2,2)	1964	1600	1602	9.5	0.045
0.08 Al	3 (0,4)	3561	3184	3152	14.4	0.221
0.08 Al	4 (2,4)	4575	4480	4436	11.4	0.466
0.08 Co	1		520	525	7.9	0.008
0.08 Co	2		1368	1380	6.7	0.092
0.08 Co	3		2432	2423	6.6	0.102
0.08 Co	4		3152	3142	12.4	0.103
0.08 Co	5		3584	3592	3.9	0.182
0.08 Co	6		3800	3788	1.8	1.990
0.08 Co	7		4248	4250	8.7	0.180
0.08 Co	8		6432	6398	11.8	0.382
0.08 Co	9		6824	6831	0.5	0.488
0.08 Co	10		7264	7258	-9.9	0.820

Table 3.6: Experimental results for cantilever 0.25" plates in air

PLATE	MODE	THEO. FREQ.	FRF FREQ.	DSPI FREQ.	MOBIL. LEVEL	INPUT FORCE
0.25 Al	1 (0,0)	883 Hz	670 Hz	665 Hz	11.7 dB	0.117 N
0.25 Al	2 (1,0)	1845	1484	1518	16.4	0.270
0.25 Co	1 (0,0)		628	601	8.4	0.118
0.25 Co	2 (0,0)		830	789	8.4	0.261
0.25 Co	3 (1,0)		1558	1565	22.3	0.105

Table 3.7:   Experimental results for cantilever 0.08" plates in air

PLATE	MODE	THEO. FREQ.	FRF FREQ.	DSPI FREQ.	MOBIL. LEVEL	INPUT FORCE
0.08 Al	1 (1,0)	264 Hz	388 Hz	402 Hz	24.8 dB	0.032 N
0.08 Al	2 (1,0)	551	636	595	11.7	0.046
0.08 Al	3 (2,0)	1401	1432	1367	21.6	0.034
0.08 Al	4 (0,1)	1682	1580	1568	6.9	0.105
0.08 Al	5 (1,1)	2121	2056	2035	5.6	0.162
0.08 Al	6 (2,1)	3258	3020	2931	9.2	0.074
0.08 Al	7 (3,0)	3371	3356	3280	-2.0	0.215
0.08 Co	1 (1,0)		584	549	22.1	0.011
0.08 Co	2 (2,0)		1348	1282	22.7	0.013
0.08 Co	3 (0,1)		1868	1848	3.4	0.120
0.08 Co	4 (1,1)		2276	2255	11.4	0.090
0.08 Co	5 (3,0)		3028	2898	4.1	0.185

Table 3.8 contains the results of the 0.25-inch-thick plates vibrating underwater with the cantilever boundary condition. The corresponding mobility functions are given in Appendix A. The mode shapes obtained with the DSPI system are shown in Appendix B. The 0° fiber direction for the composite is horizontal. Again, the clamp is at the bottom and the excitation point is at the upper left corner.

Table 3.8:   Experimental results for cantilever 0.25" plates underwater

PLATE	MODE	THEO. FREQ.	FRF FREQ.	DSPI FREQ.	MOBIL. LEVEL	INPUT FORCE
0.25 Al	1 (1,0)		856 Hz	808 Hz	19.8 dB	1.122 N
0.25 Al	2 (1,0)	1044 Hz	1064	1068	20.5	0.347
0.25 Al	3 (2,0)	3086	2956	2988	17.3	0.092
0.25 Co	1 (1,0)		928	961	32.0	0.107
0.25 Co	2 (2,0)		2624	2649	24.7	0.164

The results of the 0.08 inch thick plates vibrating underwater in the cantilever
l undary condition are contained in Table 3.9. The frequency response functions are
presented in Appendix A. The corresponding mode shapes determined by DSPI are
presented in Appendix B. The 0° fiber direction for the composites is vertical, the
clamp is at the bottom, and the excitation point is at the upper left corner.

Table 3.9:   Experimental results for cantilever 0.08" plates underwater

PLATE	MODE	THEO. FREQ.	FRF FREQ.	DSPI FREQ.	MOBIL. LEVEL	INPUT FORCE
0.08 Al	1 (2,0)	773 Hz	772 Hz	762 Hz	26.8 dB	0.052 N
0.08 Al	2 (1,1)	1147	1004	999	32.3	0.058
0.08 Al	3 (2,1)	1782	1576	1563	37.6	0.058
0.08 Al	4 (3,0)	1874	1748	1726	33.3	0.060
0.08 Al	5 (1,2)		2380	2375	26.8	0.292
0.08 Al	6 (3,1)		2700	2651	26.1	0.166
0.08 Al	7 (2,2)		3132	3139	19.2	0.256
0.08 Al	8 (4,0)		3416	3365	18.2	0.093
0.08 Co	1 (2,0)		612	583	31.3	0.012
0.08 Co	2 (1,1)		928	904	34.0	0.038
0.08 Co	3 (3,0)		1332	1272	45.8	0.006
0.08 Co	4 (3,1)		2144	2114	32.0	0.037
0.08 Co	5 (4,0)		2668	2571	22.6	0.431
0.08 Co	6 (2,2)		2852	2903	20.8	0.211

3.4. Analysis of Results

Analyses of the experimental results are made in this section including an interpretation of the fringe patterns from the DSPI measurements. The sound radiation by the plates and coincidence are briefly discussed, and the drive point mobilities that were measured with the vibrometer experiments are compared with

those calculated from the fringe patterns. Natural frequencies and mode shapes for the various cases are compared and general observations regarding the effects of fluid loading and anisotropy in the composites are presented.

3.4.1. Fringe Pattern Interpretation

The peak out-of-plane displacement at any point on the plates may be easily determined using the fringe function derived in Chapter 2. Bright and dark fringes are lines of constant displacement. This is described by the expression:

$$B \propto | J_0(\frac{4\pi\mu A}{\lambda}) | \tag{25}$$

The factor μ is the index of refraction correction for the medium in which the plates are suspended. A value of 1 is used for air and the index of refraction for water is 1.33. Maxima in the Bessel function appear as bright fringes in the image and dark fringes indicate nulls in the Bessel function. Since the wavelength is known to be 5145 Å and the value of the Bessel function argument is known for the maxima and minima [12, p.193], the displacement may be determined by simply counting fringes. The brightest fringe is used as the reference zero-order fringe which indicates a nodal line since the Bessel function has a maximum value when its argument is zero. The displacements as determined by bright fringe number is presented in Table 3.10.

Table 3.10: Fringe number/displacement relationship in time-average fringe patterns

BRIGHT FRINGE NUMBER	VALUE OF J_0 ARGUMENT	DISPLACEMENT (Å)
0	0.00	0
1	3.83	1568
2	7.02	2874
3	10.17	4164
4	13.32	5454
5	16.47	6743
6	19.62	8033
7	22.76	9319

One of the modes shapes obtained by DSPI is shown in Figure 3.7. It is the second twisting (2,0) mode for the 0.08 inch thick cantilever aluminum plate vibrating in air at 1367 Hz. This fringe pattern may be analyzed with the aid of the table above. Each fringe is a line of constant displacement so that the entire fringe pattern forms a surface displacement map of the plate.

The intensity of the two vertical zero-order fringes is obviously much higher than all other fringes. These bright fringes indicate nodal lines on the plate. The plate is clamped at the bottom so a nodal region is expected to be seen. The displacement anywhere on the plate may be found by simply counting fringes away from the bright fringe, and then calculating the corresponding displacement. For instance, at the drive point which is in the upper left corner of the image, a fifth
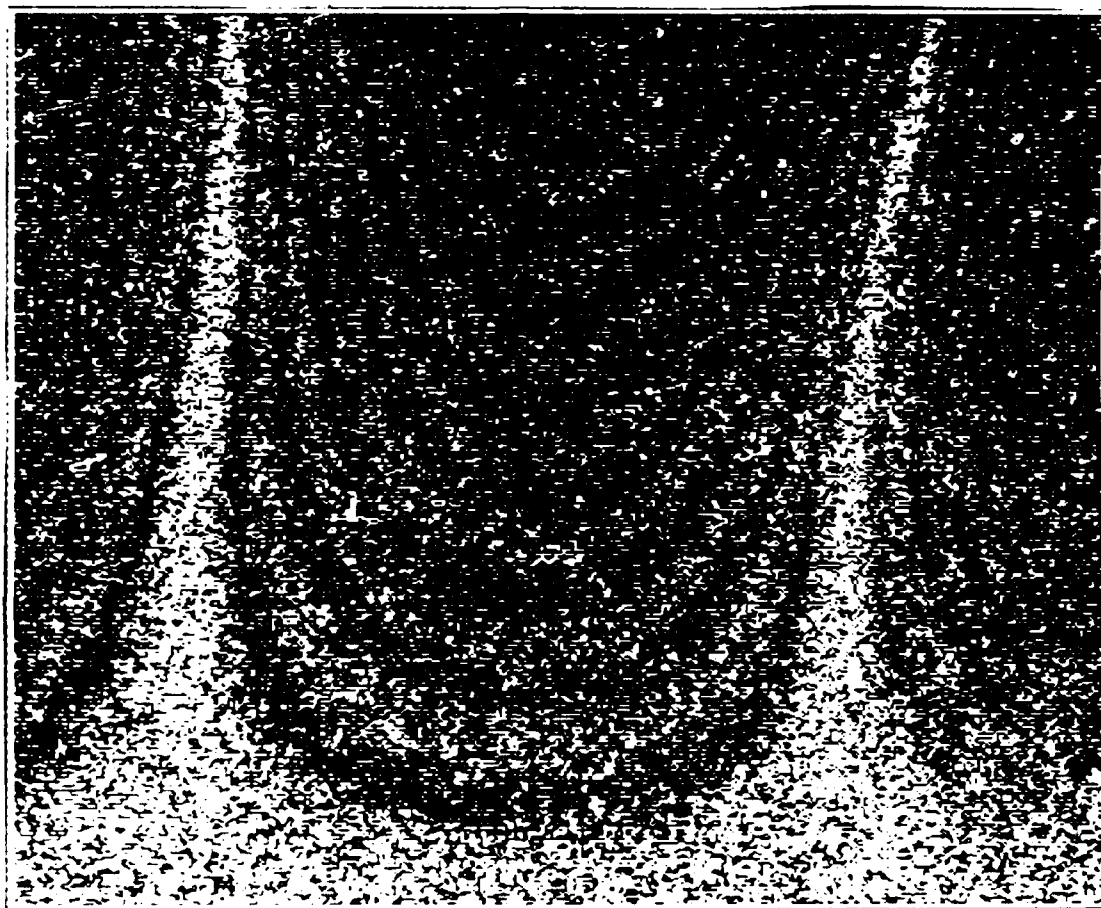
Figure 3.7:   DSPI fringe pattern for (2,0) mode of 0.08" cantilever aluminum plate in air

order bright fringe is seen and corresponds to a peak out-of-plane displacement of 6743 Å from Table 3.10.

A vibration phase mapping analysis as described in section 2.1.5 would show that the antinodal regions at the left and right sides of the plate are in phase, and 180° out of phase with the center region between the vertical nodal lines. This phase map would show that the plate is twisting about the two vertical nodal lines. The motion of the plate is described completely if the displacement and phase information are both known.

3.4.2. Sound Radiation and Coincidence

Coincidence occurs when a plate in an acoustic medium vibrates at a critical frequency such that the wavelength of the flexural waves on the plate is the same as the wavelength of the acoustic waves in the medium. This is an important phenomenon because below coincidence, the plate will not radiate sound efficiently. The equation for the well-known critical frequency is given by Junger and Feit [29]:

$$f_c = \frac{c^2}{2\pi} \sqrt{\frac{\rho h}{D}} \tag{26}$$

where c is the sound speed in the medium, ρ is the density of the plate material, h is the thickness of the plate, and D is the flexural rigidity. This equation assumes that the plate is of infinite extent and obeys thin plate theory. The equation may be

approximately valid for finite plates if only high frequencies are under consideration such that the wavelengths are small compared to plate dimension [30]. Otherwise, a small amount of radiation may be heard below coincidence due to edge effects of the finite plates. The frequencies calculated for each case in this study are tabulated in Table 3.11.

Table 3.11:   Coincidence frequencies for each plate in air and in water

PLATE/FLUID	f_c (kHz)
0.25" Al in air	1.93
0.25" Al in water	36.88
0.08" Al in air	6.03
0.08" Al in water	115.25
0.25" Co in air	1.52
0.25" Co in water	29.09
0.08" Co in air	5.35
0.08" Co in water	102.40

Coincidence is important because appreciable sound radiation from the plates will be heard only at resonances above coincidence. For these cases, resonances were identified by listening to the response of the plate as well as observing the input force level. In the experiments, the amplitude of the plate response did not increase significantly at resonance; however, the phase shift associated with resonance from the mobility curves could be heard while slowly sweeping through the resonance. For

natural frequencies below coincidence, resonance could only be identified by observing the input force level. Although the finite dimensions of the plates and boundary conditions affected the sound radiation, the effects of coincidence were observed to generally follow the theory; however, an actual measurement of the radiated sound would provide a better quantitative description.

3.4.3. Comparison of Drive Point Mobilities

The drive point mobility for each mode may be calculated from the fringe patterns and measured input force level. The drive point velocity is determined by calculating the displacement at the drive point on the fringe pattern and multiplying by the frequency for that mode. The mobility level is found by dividing the calculated velocity by the force, dividing by the reference mobility, and taking the logarithm of the ratio. This calculation was performed for the 0.25 inch plates with the free boundary condition. The results are presented in Table 3.12 [31].

The mobilities calculated from the fringe patterns do not agree well with the measured mobilities although relative levels of the modes for each plate follow the same trends. The velocities measured by the vibrometer are much more accurate than those calculated from the speckle patterns because the vibrometer measures at a single point. The accuracy of the displacements measured from the fringe patterns depends on the width of the fringes. The maximum error for a measurement from the center of a fringe is about 325 Å which corresponds to the difference in the Bessel argument across half the width of a fringe. At 3592 Hz, this produces a

velocity error of approximately 0.0007 m/sec for mode 1 of the composite in air.

Some general observations regarding the behavior of the mobility levels were made. The mobility levels for the modes in the 0.25 inch plates were lower than the levels for the 0.08 plates. In addition, the mobility levels for the plates in air were higher than the levels for the plates in water.

Table 3.12: Calculated drive point mobilities and related data (Pechersky and Bergen, 1990)

Mode	Frequency (Hz)	Mode Shape	Drive Point Mobility[1]	Input Force (Newtons)	Drive Point Velocity[2] (m/sec)	Calculated Mobility[3]
Aluminum in Air (Mode 1)	3912	2,0	11.2	0.376	0.0191	12.1
Aluminum in Water (Mode 1)	2837	2,0	2 7	0.782	0.0098	4.7
Aluminum in Water (Mode 2)	7367	2,2	- 2.6	0 841	0 0064	2.6
Composite in Air (Mode 1)	3592	Split Mode	- 5.2	0.535	0.0051	4 8
Composite in Air (Mode 2)	4312	Split Mode	10 0	0 406	0 0166	11.1
Composite in Water (Mode 1)	2171	Split Mode	-15 9	0.662	0.0016	-2 4
Composite in water (Mode 2)	2695	Split Mode	1 9	0 381	0 0077	4 2
Composite in Water (Mode 3)	6525	2,2	-6 7	1 850	0 0105	1 5

[1] From vibrometer measurements in dB re 0 003164 m/NS in air
[2] Estimated from DSPI fringe patterns.
[3] From estimated velocity and input force in dB re 0 003164 m/NS in air.

These trends were expected since greater input forces were required to excite the thicker plates and plates suspended in a fluid medium more dense than air.

3.4.4. Natural Frequency Observations

The calculated theoretical natural frequencies accurately estimated the frequencies for the homogeneous plates vibrating in air usually with less than 10% error. The resonance frequencies for the composite plates were not accurately predicted with a simple calculation. This is due to the anisotropy in the plates and the fact that the average elastic moduli were used in the calculations. The theoretical frequencies computed by assuming simple mass-loading significantly underestimated the measured resonance frequencies for the plates underwater. The underestimate is due to the nature of the added mass approximation used by Blevins which is a function only of the dimensions of the plates and the density of the fluid. In reality, the fluid loading effect depends on the mode shapes and modal masses for individual resonance modes.

The experimental results show that the fluid loading had a greater effect on the composite plates than the aluminum plates because the composites were less dense than the aluminum. The added mass lowered the resonance frequencies of the aluminum by 30% to 40% and the composites by 40% to 60%. The decrease in natural frequencies generally allowed more modes to be excited underwater.

3.4.5. Mode Shape Observations

Up to eight fringes were recorded for the mode shapes described by the speckle patterns. Full-field displacement information for the modes may be determined by the fringe analysis described in section 3.4.1. Only the modes that could be obtained with the DSPI system are presented. Modes below about 400 Hz could not be recorded because an insufficient number of cycles were time-averaged. At higher frequencies, the measurements were limited by the performance of the shaker and the operating range of the force gage (0-10 kHz).

The mode shapes obtained with DSPI agreed well with theory for the homogeneous aluminum plates. This is especially true for the free aluminum plates both in air and underwater. For the 0.08 inch aluminum plates in the cantilever condition, there were slight inconsistencies in the mode shapes. For example, the first mode does not look like the first bending mode but more like a distorted (1,0) mode. The sixth mode is also distorted although it looks like it could be a (2,1) mode. The distortion may be due to added mass or stiffness by the drive mechanism or inexact clamping. This (2,1) mode appeared clearly underwater as the third mode. The occurrence of this mode was not predicted by Leissa. In addition, the (0,1) mode for the aluminum in air was not excited underwater possibly because the nodal line for the mode is close to the drive point. The underwater mode shapes were slightly deformed compared to the in-air modes which is probably due to modal coupling by the dense fluid [29, p.265].

Some of the mode shapes obtained for the free composite plates were clearly different from the ones for the isotropic plates. This is undoubtedly due to the anisotropy in the plates. Irregular and elaborate nodal patterns were acquired for the 0.08 inch composites both in air and underwater with the free boundary condition. The anisotropy seemed to have less of an effect on the composites with the cantilever boundary condition, because some classical mode shapes were obtained although they were slightly deformed. DSPI proved to be extremely practical in vibration analysis of anisotropic structures because the theoretical natural frequencies and mode shapes are generally unavailable.

CHAPTER 4

SUMMARY AND CONCLUSIONS

4.1. Conclusions

General conclusions regarding the experiments are drawn based on the results. These experimental results are briefly discussed and the performance of the DSPI system is evaluated. Future work is proposed and the thesis is summarized.

4.1.1. Discussion of Experimental Results

The experimentally determined natural frequencies for the aluminum plates agreed well with theory. Deviation can be attributed to the drive point mass loading effect of the stinger/force gauge and shaker spindle. The natural frequencies of the composites were difficult to predict due to the anisotropy of the plates. Fluid loading had a greater effect on the composites than the aluminum plates. This allowed extra modes to be excited underwater for both plates in the frequency range of interest.

The excited mode shapes of the aluminum determined by DSPI were also generally close to the theoretical modes according to Leissa. The mode shapes in water are very similar to those in air with a small amount of distortion due to modal coupling by the fluid.

Fluid loading also had a significant effect on the mobility of the plates. The drive point mobility was lowered by the fluid loading. Clearly, if the mobility is

lowered, a greater input force is required to excite the plates at comparable amplitudes. Fluid loading should theoretically decrease the response of the plates with a damping effect.

The loading by the water also profoundly affected the perceived acoustic radiation by the plates. This is due to the fact that the presence of the water greatly increased the coincidence frequency between the fluid and plate. This is important because most of the plate resonances occurred above coincidence in air and well below coincidence in water. Finite plates are efficient acoustic radiators only well above coincidence. This was observed during the experiments by simply listening to the radiation; however, an actual measurement of the radiated sound pressure would give a better quantitative description.

4.1.2. Evaluation of the DSPI System

DSPI proved to be a powerful and convenient method of evaluating the modal vibration characteristics of the plates in this study. Once the system was assembled, it was very easy to use and data was acquired quickly. DSPI is particularly useful for analyzing anisotropic structural vibrations since the theoretical natural frequencies and mode shapes were not readily available. The modal characteristics may be determined by finite element analysis using the predicted elastic moduli of the composite plate, but this is much more time consuming than DSPI.

The mobility could not be accurately determined by DSPI because the speckle patterns do not have the high spatial resolution of a single point velocity

measurement like laser vibrometry. In addition, a precise measure of the damping of structures for each mode cannot be determined by DSPI. The damping may be found from the mobility curves by determining the half-power bandwidth for each mode which is proportional to the damping ratio. The damping along with natural frequencies and mode shapes for each mode provides a complete modal analysis for any structure. Therefore, DSPI and laser vibrometry operating in conjunction furnish excellent non-intrusive modal vibration analysis measurements.

4.2. Future Work

The optical design of ESPI/DSPI is well established, and the only room for improvement is in the mechanical design of the system and fringe pattern enhancement through image processing. Although the applications of DSPI are virtually unlimited, some experiments which would be particularly interesting have been proposed.

4.2.1. Improvements to DSPI System

Improvements to the system discussed in this thesis have been proposed to decrease the effect of the low frequency instability in the optics. One method involves the chopping of the laser output beam as discussed by Lokberg [32]. Another proposed method involves reflecting the reference beam off of the object support before combining it with the object beam. The reflected beam would theoretically provide feedback information about the instability to the reference

beam. Image processing techniques have also been explored to improve the contrast of the fringe patterns and extract displacement information directly from the images. Ideally, the speckle patterns should be smoothed so that the speckle is removed and high-contrast bright and dark fringes are seen as in conventional holography. Output in the form of color displacement maps and animated three-dimensional mode shapes is desirable.

4.2.2. Experimental Applications

A measurement of the sound radiated by vibrating structures in association with the mode shape determination by DSPI has been considered. A measure of the sound pressure produced by a vibrating structure in a reverberant chamber can provide information about the radiation efficiency of the modes of the structure. This efficiency is strongly affected by coincidence as determined by the ambient medium in the chamber. A thorough understanding of the acoustic radiation by a structure may be helpful in implementing sound and vibration control techniques.

This thesis is concerned with the use of DSPI to study the vibrations of flat plates. However, the technique easily lends itself to the study of three-dimensional objects such as shells. The only special consideration for the analysis of three dimensional structures is that the dimensions of the object must fit in the depth of field of the imaging system for proper focusing. Analysis of the fringe patterns may be more difficult since the patterns indicate only the out-of-plane component of the displacements.

4.3. Summary

The experimentally determined natural frequencies and mode shapes agreed well with theory for the homogeneous aluminum plates. The modes of the composite plates could not be predicted due to the anisotropy in the material. The resonances, determined from the laser vibrometry measurements, accurately predicted those determined by DSPI. Fluid loading of the plates had a significant effect on the natural frequencies and mode shapes as expected. The fluid had a greater effect on the natural frequencies of the composites than those of the aluminum. This was also expected. There were slight distortions of the mode shapes underwater due to the modal coupling effect of the fluid. In addition, the plates had decreased mobility and were more difficult to excite underwater due to the fluid loading.

DSPI proved to be an efficient technique for acquiring the mode shapes, especially for the anisotropic plates. Furthermore, the use of vibrometry in conjunction with DSPI provided an accurate experimental modal analysis system.

REFERENCES

1. Powell, Robert L., and Karl A. Stetson, "Interferometric Vibration Analysis by Wavefront Reconstruction," Journal of the Optical Society of America 55 (1965)1593-8.

2. Butters, J.N., and J.A. Leendertz, "Speckle Pattern and Holographic Techniques in Engineering Metrology," Optics and Laser Technology Feb. 1971: 26-30.

3. Lokberg, Ole, "Electronic Speckle Pattern Interferometry," Physical Technology 11 (1980) 17.

4. Lokberg, Ole J., and Jan T. Malmo, "Long-Distance Electronic Speckle Pattern Interferometry," Optical Engineering 27 (1988) 150-6.

5. Tyrer, John R., "The Use of TV Holography (ESPI) for Loudspeaker Chassis and Cabinet Modal Analysis," Journal of the Audio Engineering Society 36 (1988) 342-9.

6. Biedermann, K., and L. Ek, "A Recording and Display System for Hologram Interferometry with Low Resolution Imaging Devices," Journal of Physics E: Scientific Instruments 8 (1975) 574.

7. Malmo, J.T., and E. Vikhagen, "Vibration Analysis of a Car Body by Means of TV Holography," Experimental Techniques Apr. 1988: 28-30.

8. Parker, R.J., and D.G. Jones, "Holography in an Industrial Environment," Optical Engineering 27 (1988) 55-66.

74

9. Lokberg, O.J., K. Hogmoen, and O.M. Holje, "Vibration Measurement on the Human Ear Drum in vivo," <u>Applied Optics</u> 18 (1979) 763-5.

10. Vikhagen, E., and O.J. Lokberg, "Detection of Defects in Composite Materials by Television Holography and Image Processing," <u>Materials Evaluation</u> 48 (1990) 244-8.

11. Croteau, Rudolph E., and Herman E. Sheets, "Determination of Underwater Plate Dynamics Using Laser Beams," <u>Journal of Engineering for Industry</u> Aug. 1974: 722-8.

12. Luxon, and David E. Parker, <u>Industrial Lasers and Their Applications</u> (Englewood Cliffs, NJ: Prentice-Hall,Inc., 1985) 2.

13. Jones, Robert and Catherine Wykes, <u>Holographic and Speckle Interferometry</u> (Cambridge: Cambridge University Press, 1983) 8.

14. Butters, Jones, and Catherine Wykes, "Electronic Speckle Pattern Interferometry," <u>Speckle Metrology</u>, ed. Robert K. Erf (New York: Academic Press, 1978) 115.

15. Slettemoen, Gudmunn A., "Electronic Speckle Pattern Interferometric System Based on a Speckle Reference Beam," <u>Applied Optics</u> 19 (1980) 616-23.

16. Lokberg, Ole J., and Kare Krakhella, "Electronic Speckle Pattern Interferometry Using Optical Fibers," <u>Optical Communications</u> 38 (1981) 155-8.

17. Gradshteyn, I.S., and I.M. Ryzhik, <u>Table of Integrals, Series, and Products</u> (New York: Academic Press, 1980)   952.

18. Creath, Katherine. "Digital Speckle Pattern Interferometry (DSPI) Using a 100x100 Imaging Array," <u>SPIE: State-of-the-Art Imaging Arrays and Their Applications</u> 501 (1984) 293.

19. Lokberg, Ole J., and Gudmann A. Slettemoen, "Interferometric Comparison of Displacements by Electronic Speckle Pattern Interferometry," <u>Applied Optics</u> 20 (1981) 2631.

20. Lokberg, Ole J., and Kare Hogmoen, "Vibration Phase Mapping Using Electronic Speckle Interferometry," <u>Applied Optics</u> 15 (1976) 2701-4.

21. Dandliker, R., and R. Thalmann, "Heterodyne and Quasi-heterodyne Holographic Interferometry," <u>Optical Engineering</u> 24 (1985) 824-31.

22. Newport Research Corporation, <u>Newport Catalog</u> 1990 I-18.

23. Lokberg, Ole J., "ESPI - The Ultimate Holographic Tool for Vibration Analysis?," <u>Journal of the Acoustical Society of America</u> 75 (1984) 1784.

24. Stetson, Karl A., "New Design for Laser Image-Speckle Interferometer," <u>Optics and Laser Technology</u> 2 (1970) 179-81.

25. Amateau, M., COMPLY, Applied Research Laboratory.

26. Leissa, Arthur W., Vibrations of Plates (Washington D.C.: Office of Technology Utilization NASA, 1969).

27. Blevins, Robert D., Formulas for Natural Frequency and Mode Shape (Malabar, FL: Robert E. Krieger Publishing, 1986).

28. Leibowitz, R. C., Vibroacoustic Response of Turbulence Excited Thin Rectangular Plates in Heavy and Light Fluid Media, Ship Acoustics Department Research and Development Report 2976G (Bethesda, MD: David M. Taylor Naval Ship Research and Development Center, Sept. 1975) 470.

29. Jur̩er, Miguel C., and David Feit, Sound, Structures, and Their Interaction (Cambridge, MA: The MIT Press, 1986) 236.

30. Pierce, Allan D., Acoustics (Woodbury, NY: The Acoustical Society of America, 1989) 128.

31. Pechersky, M.J., and T.F. Bergen, "ESPI Measurements of Submerged Composite Plate Vibrations," 1990 SEM Fall Conference on Holographic Interferometr̄ and Speckle Metrology, 4-7 November 1990.

32. Lokberg, Ole J., "Use of Chopped Laser Light in Electronic Speckle Pattern Interferometry," Applied Optics 18 (1979) 2377-84.

APPENDIX A

RESULTS OF DRIVE POINT MOBILITY MEASUREMENTS

The frequency response functions determined from the vibrometry experiments are presented in this appendix. These mobility curves correspond to the data given in section 3.3.3 of the thesis. The correspondence is as follows:

FIGURE NUMBER	CORRESPONDING TABLE OF RESULTS
A.1 - A.2	Table 3.2
A.3 - A.6	Table 3.3
A.7 - A.8	Table 3.4
A.9 - A.12	Table 3.5
A.13 - A.14	Table 3.6
A.15 - A.16	Table 3.7
A.17 - A.18	Table 3.8
A.19 - A.20	Table 3.9
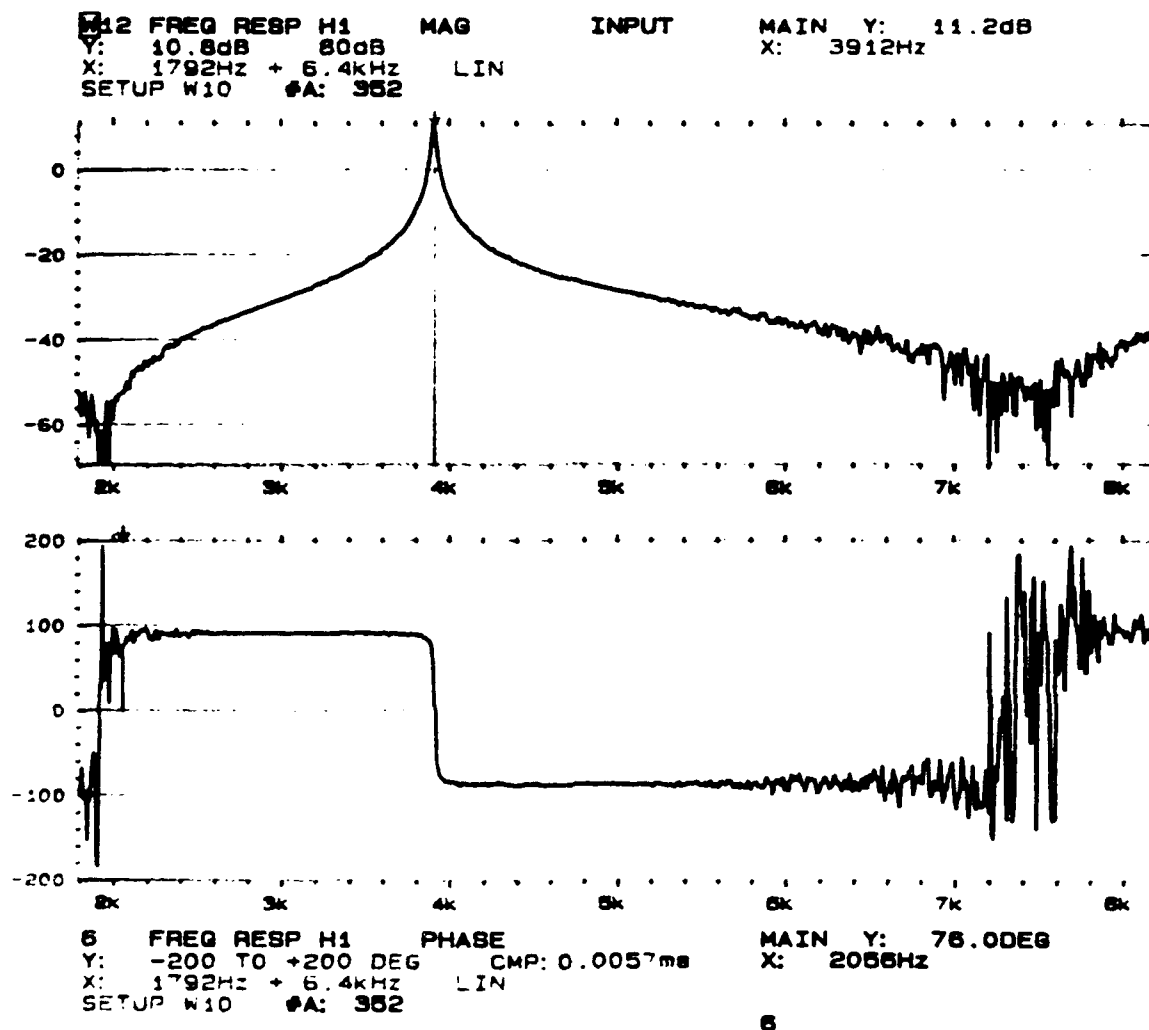
Figure A.1: Drive point mobility of 0.25 inch free aluminum plate in air (1792-8192 Hz).
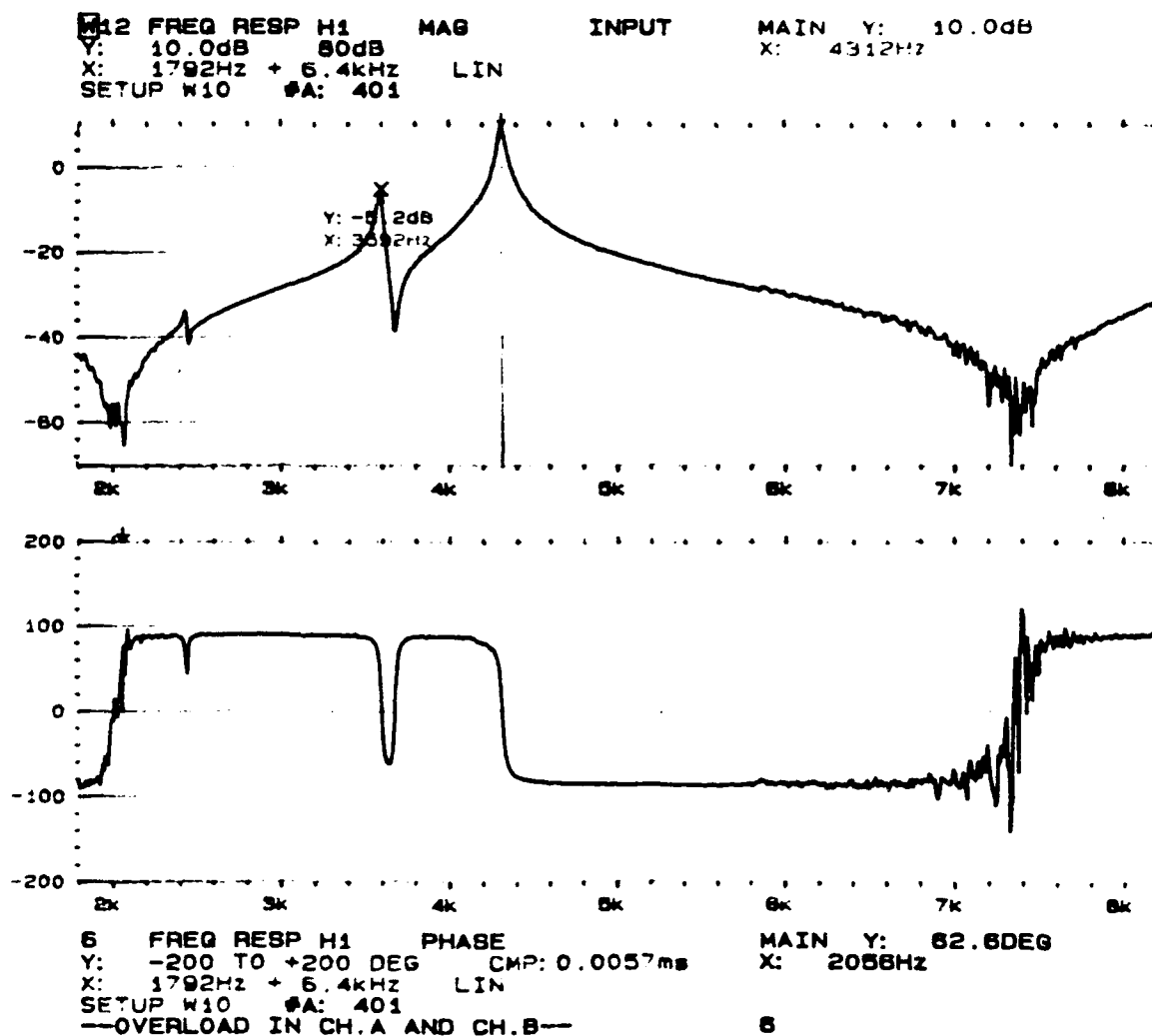
Figure A.2: Drive point mobility of 0.25 inch free composite plate in air (1792-8192 Hz).
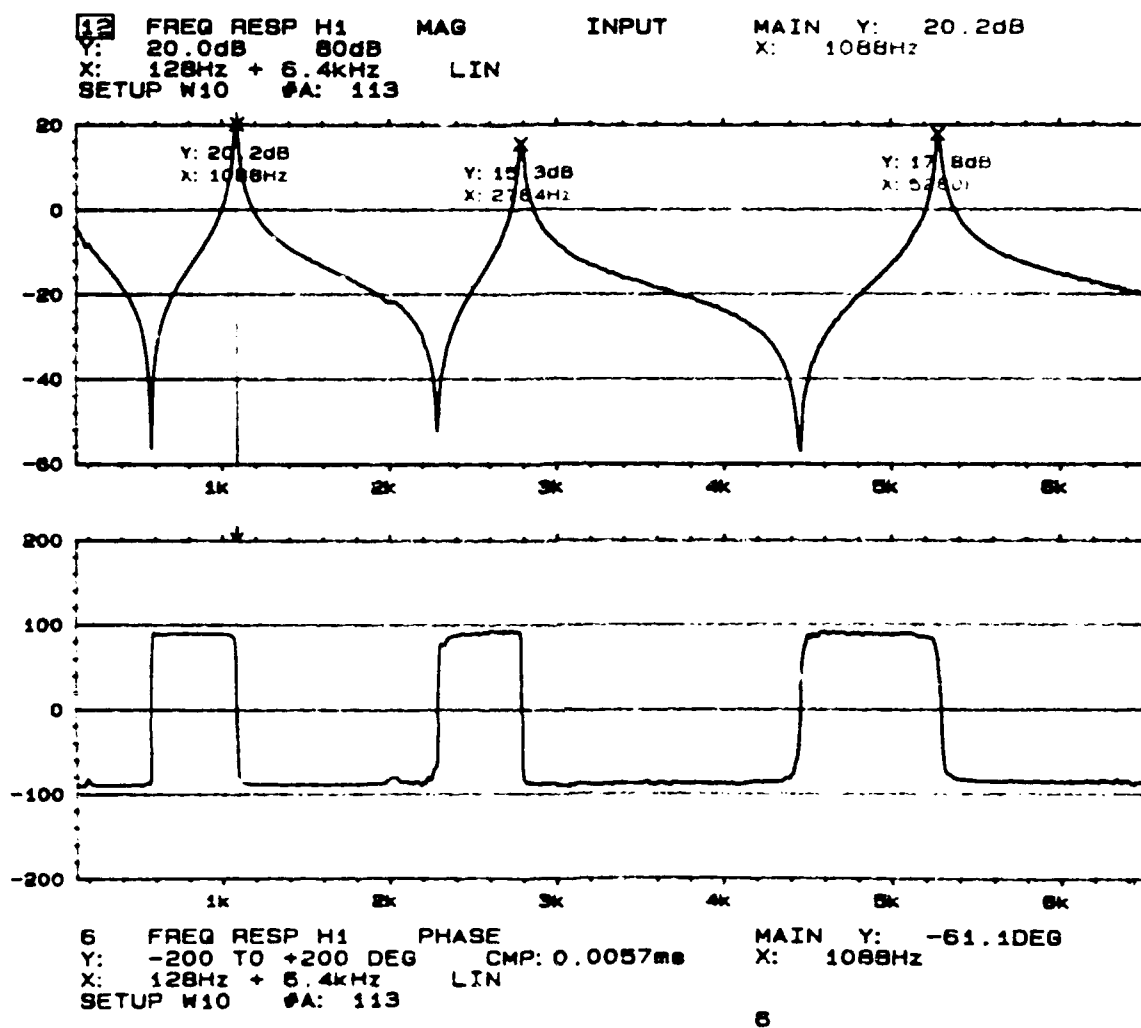
Figure A.3: Drive point mobility of 0.08 inch free aluminum plate in air (128-6528 Hz).
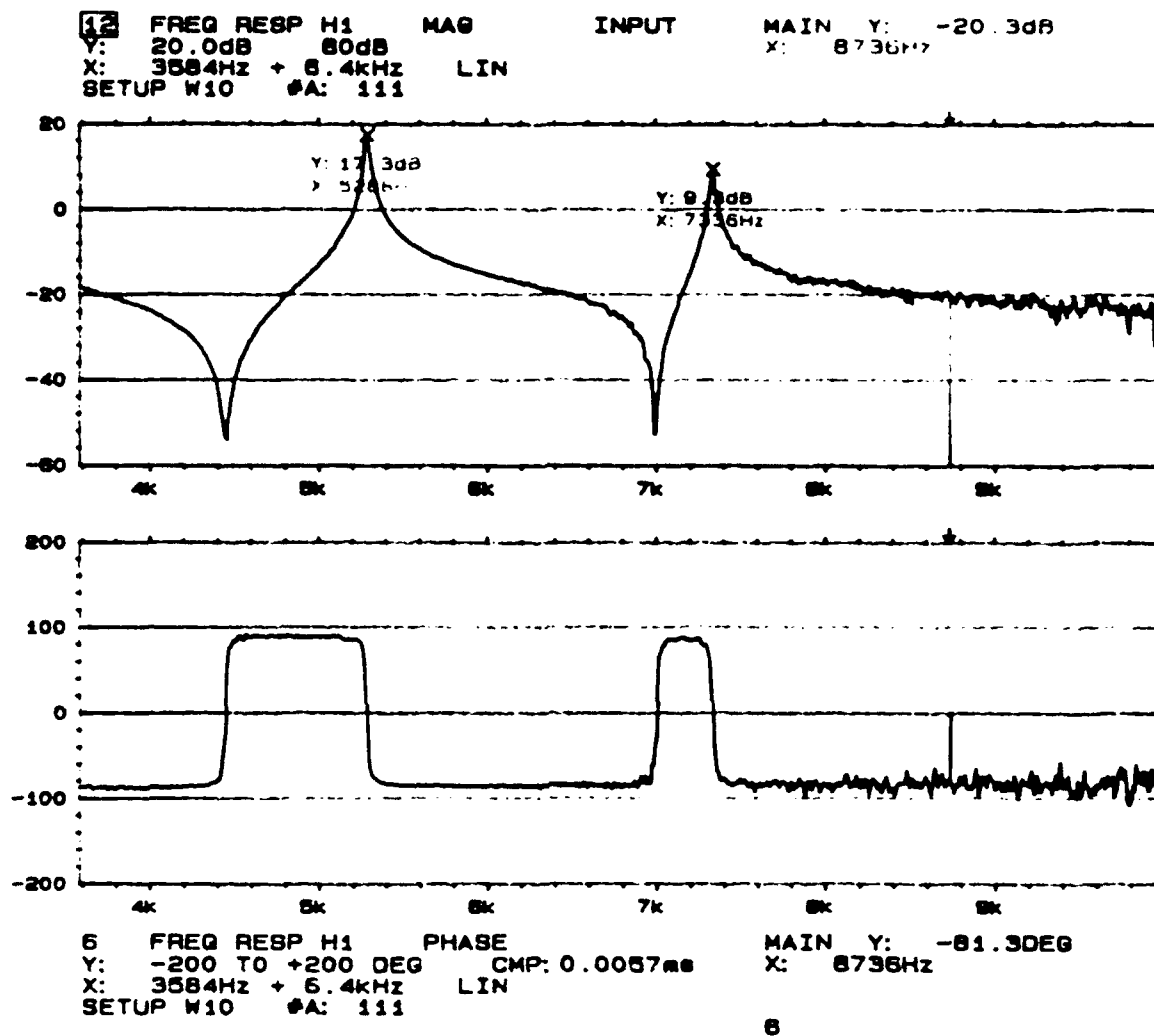
Figure A.4: Drive point mobility of 0.08 inch free aluminum plate in air (3584-9984 Hz).
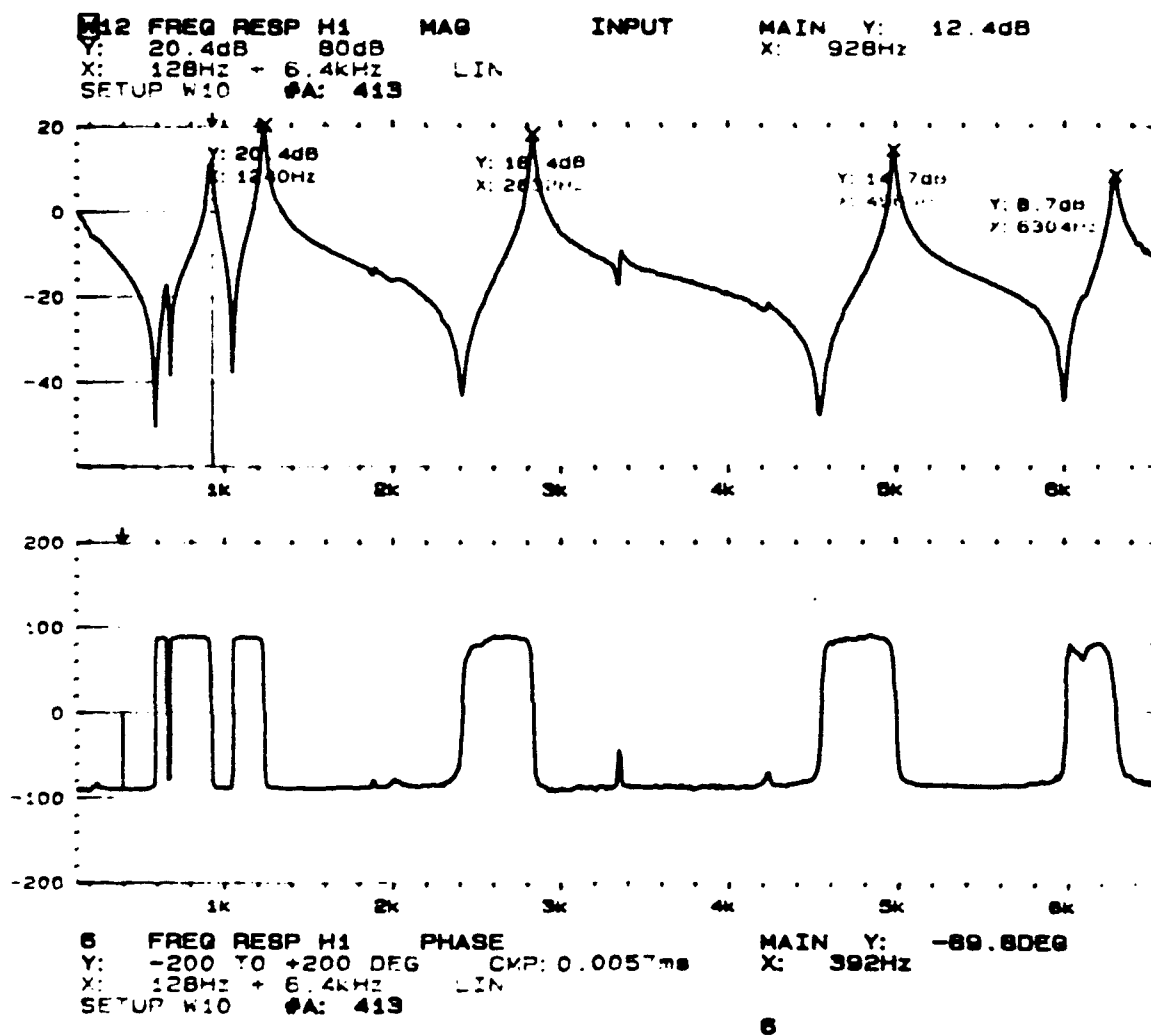
Figure A.5: Drive point mobility of 0.08 inch free composite plate in air (128-6528 Hz).
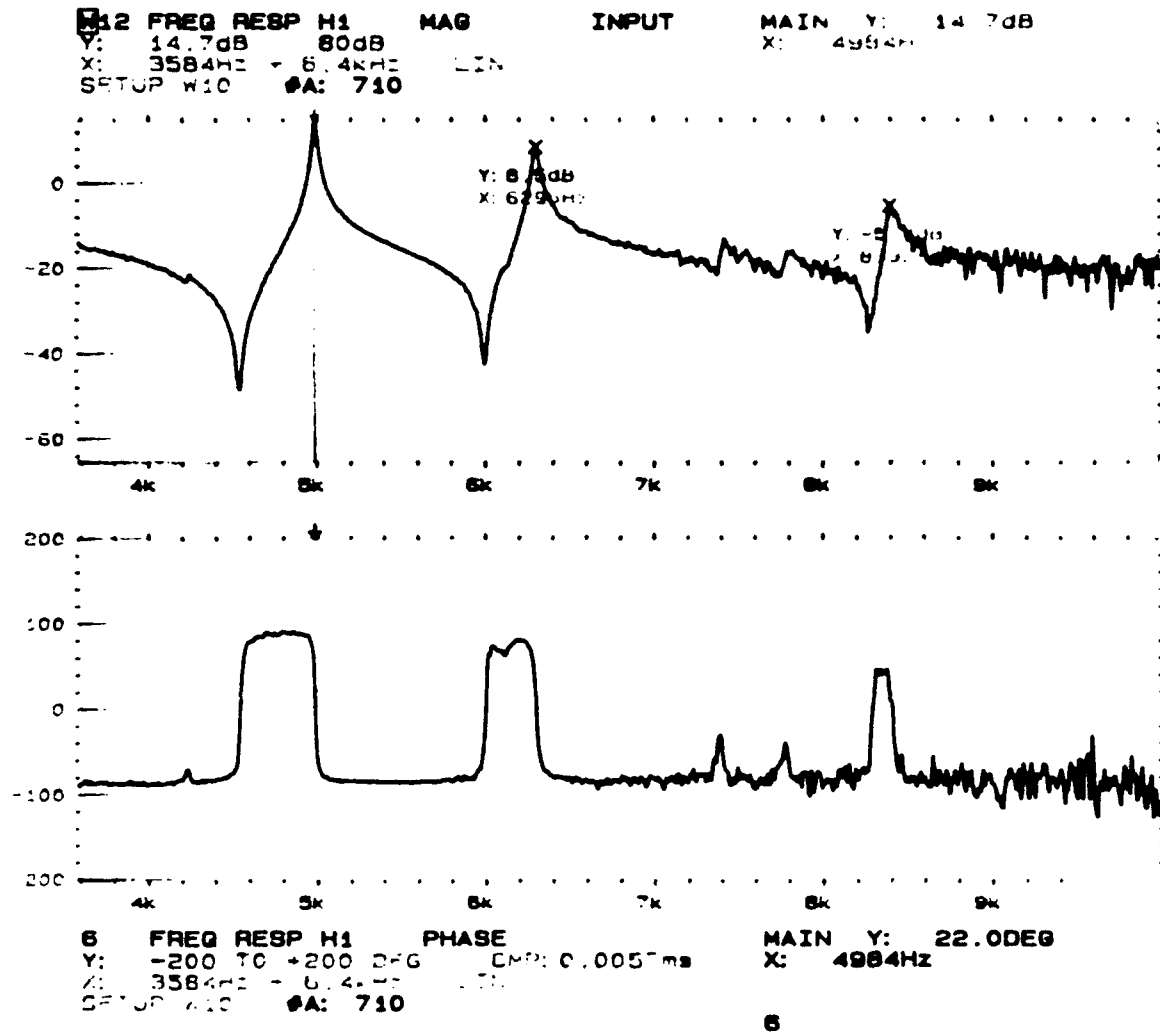
Figure A.6: Drive point mobility of 0.08 inch free composite plate in air (3584-9984 Hz).

85

```
M1   FREQ RESP H1      MAG          INPUT        MAIN  Y:   -2.6dB
Y:   2.7dB   80dB                                X:    7368Hz
X:   1792Hz + 6.4kHz   LIN
SETUP W10   #A:  427
```

```
Y: 2.7dB
X: 2824Hz

                                              Y: -2.6dB
                                              X: 7368Hz
```

```
6    FREQ RESP H1      PHASE                    MAIN  Y:   36.7DEG
Y:   -200 TO +200 DEG      CMP: 0.0057ms        X:    7368Hz
X:   1792Hz + 6.4kHz   LIN
SETUP W10   #A:  427
```

6
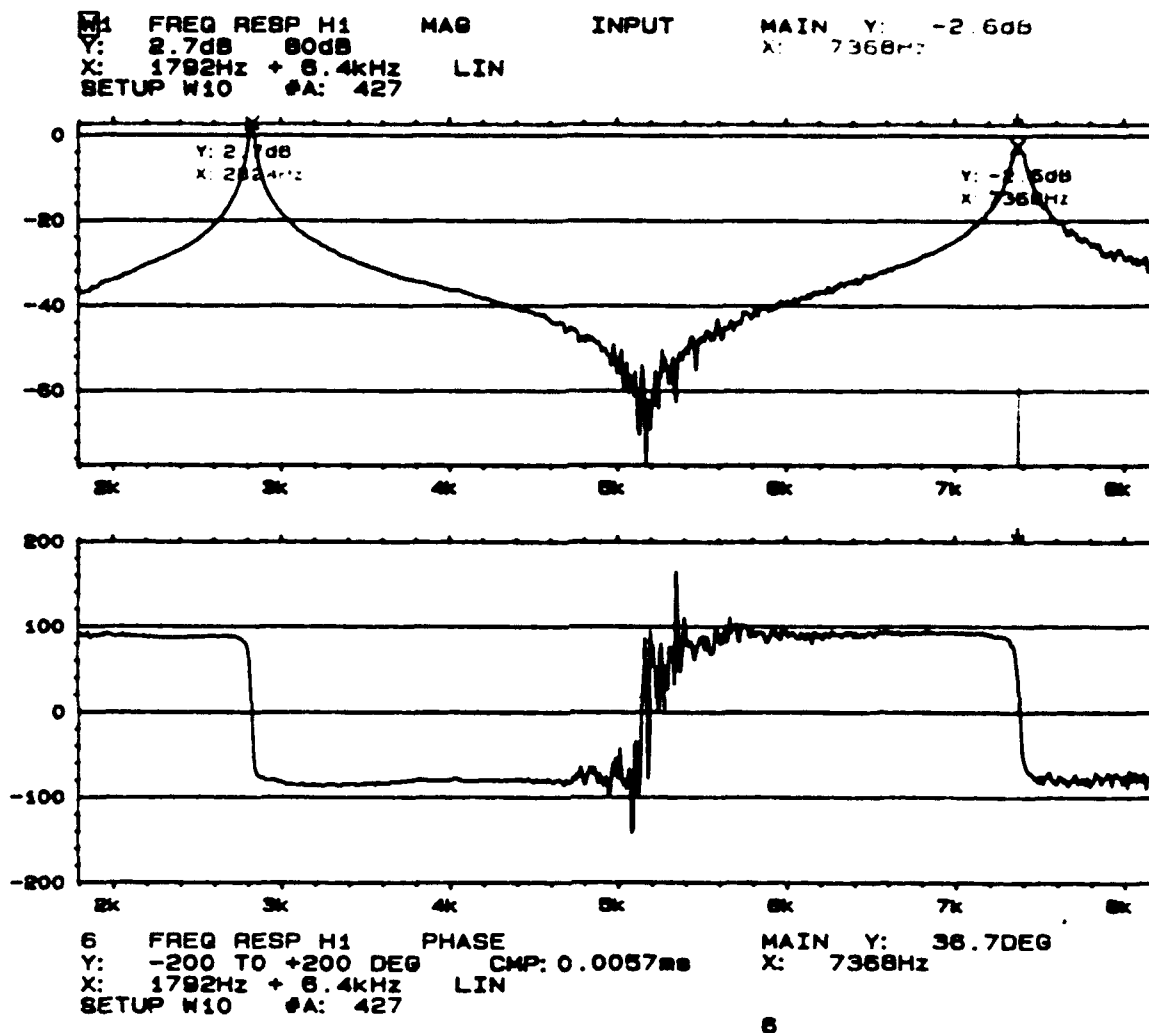
Figure A.7: Drive point mobility of 0.25 inch free aluminum plate underwater (1792-8192 Hz).

W1   FREQ RESP H1   MAG   MAIN Y: -6.7dB
Y: 2.7dB   60dB   X: 6526rt·
X: 1792Hz + 6.4kHz   LIN
SETUP W10   #A: 460

B   FREQ RESP H1   PHASE   INPUT   MAIN Y: 21.7DEG
Y: -200 TO +200 DEG   CMP: 0.0057ms   X: 6526Hz
X: 1792Hz + 6.4kHz   LIN
SETUP W10   #A: 460

                                              6
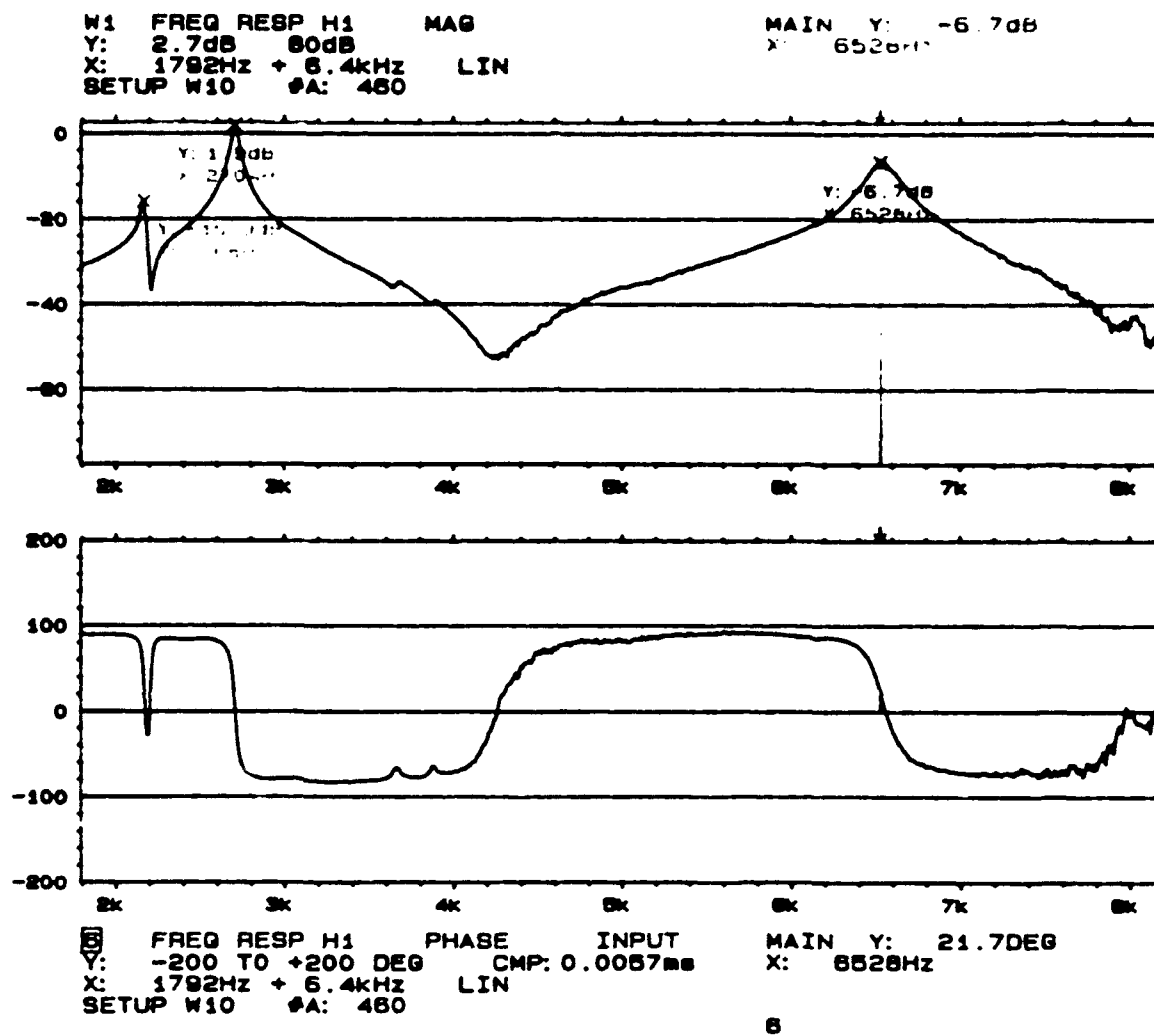
Figure A.8:   Drive point mobility of 0.25 inch free composite plate
              underwater (1792-8192 Hz).
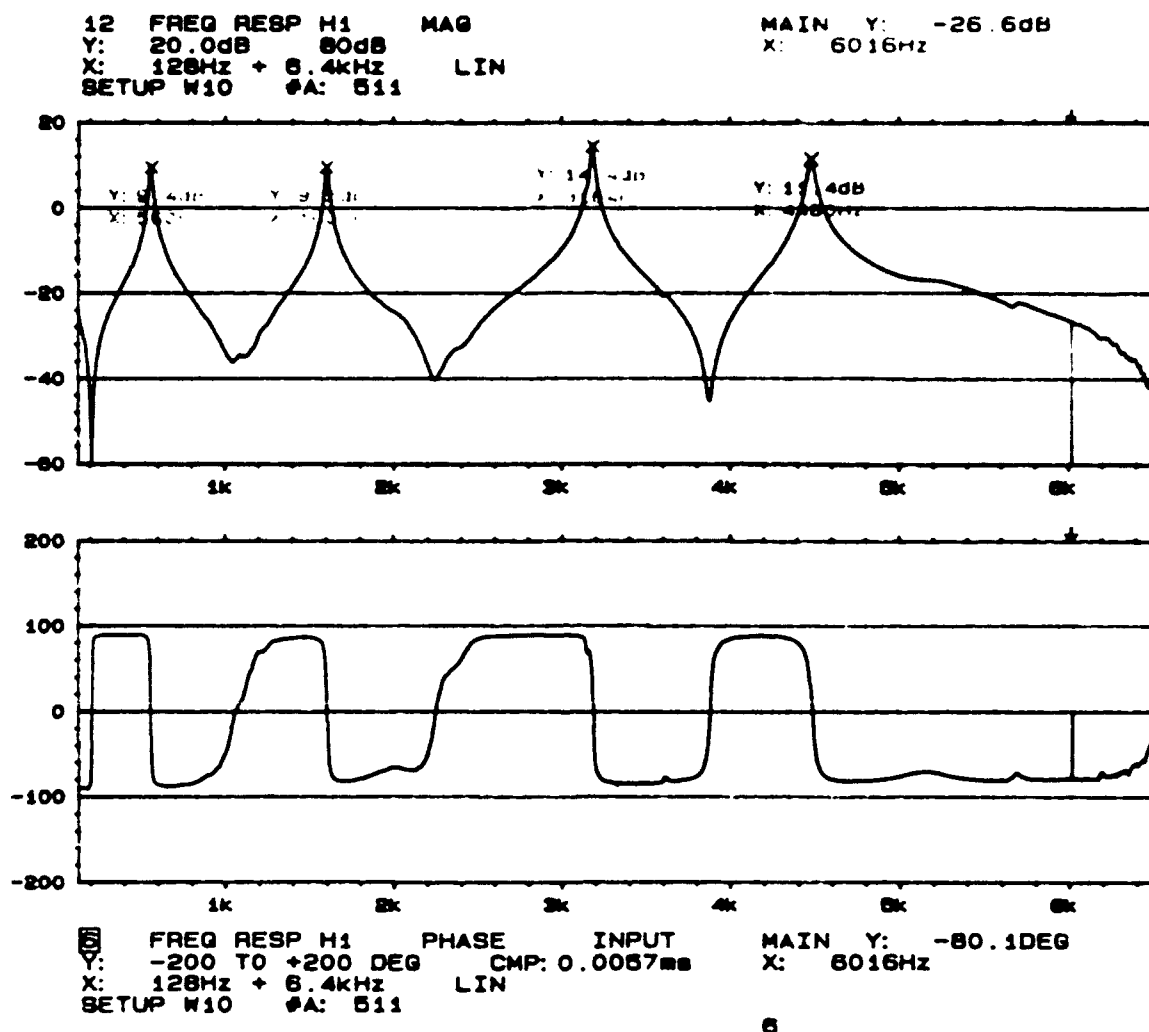
Figure A.9: Drive point mobility of 0.08 inch free aluminum plate underwater (128-6528 Hz).

12 FREQ RESP H1   MAG   INPUT   MAIN Y: -30.0dB
Y: 20.0dB   80dB   > 6 'P-.
X: 3584Hz + 6.4KHz   LIN
SETUP W10   #A: 452

80

Y: -3.0db
X: 9928Hz

0

Y: 1 .4b

-20

-40

-60

4k   5k   6k   7k   8k   9k

200

100

0

-100

-200

4k   5k   6k   7k   8k   9k

6 FREQ RESP H1   PHASE   MAIN Y: 83.0DEG
Y: -200 TO +200 DEG   CMP: 0.0057ms   X: 6784Hz
X: 3584Hz + 6.4kHz   LIN
SETUP W10   #A: 452

6
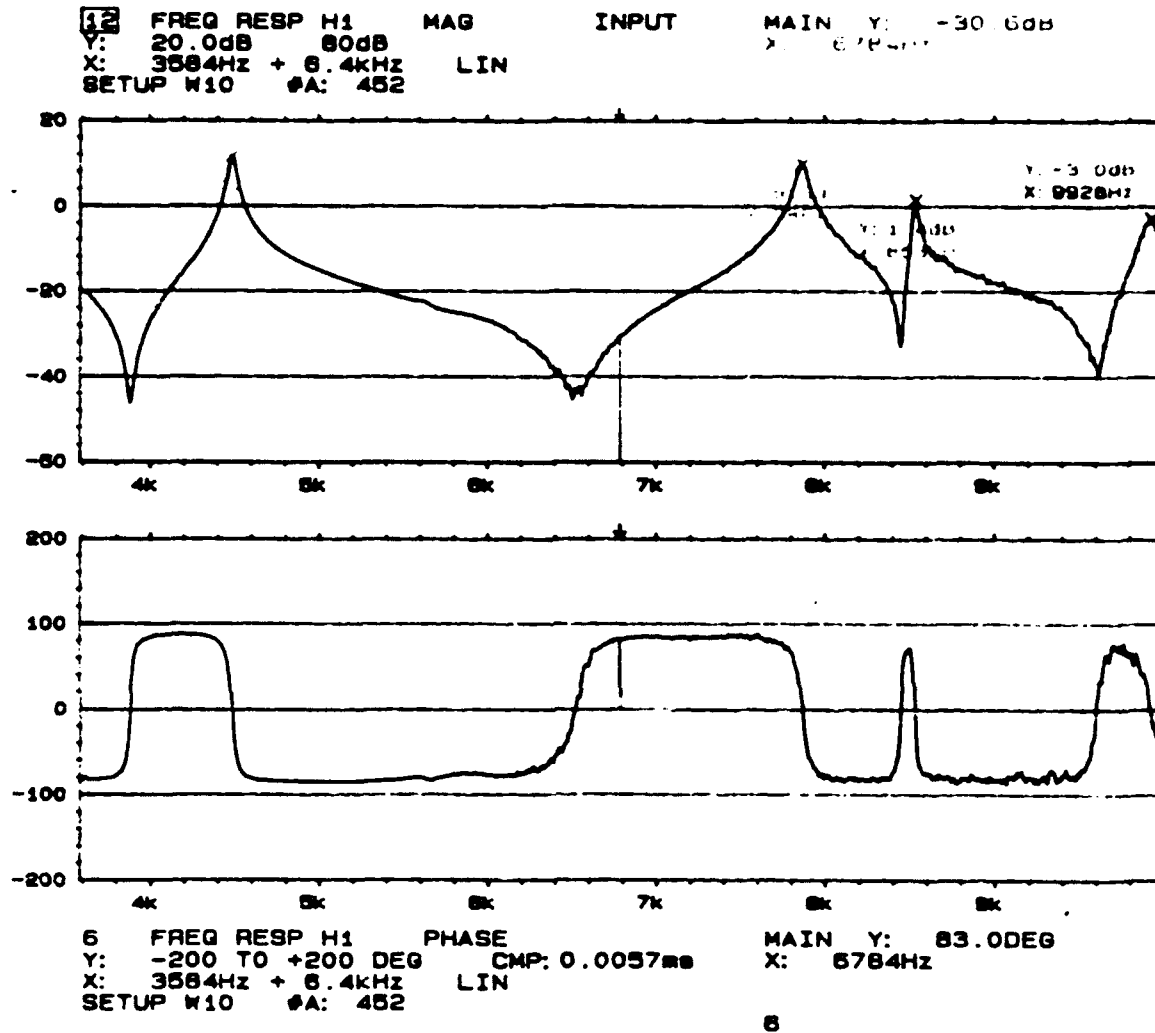
Figure A.10: Drive point mobility of 0.08 inch free aluminum plate
underwater (3584-9984 Hz).

W1   FREQ RESP H1   MAG   MAIN Y: 10.6dB
Y: 13.1dB   60dB   X: 6440Hz
X: 128Hz + 6.4kHz   LIN
SETUP W10   #A: 100

B   FREQ RESP H1   PHASE   INPUT   MAIN Y: -26.1DEG
Y: -200 TO +200 DEG   CMP: 0.0067ms   X: 6440Hz
X: 128Hz + 6.4kHz   LIN
SETUP W10   #A: 100
                                                  6
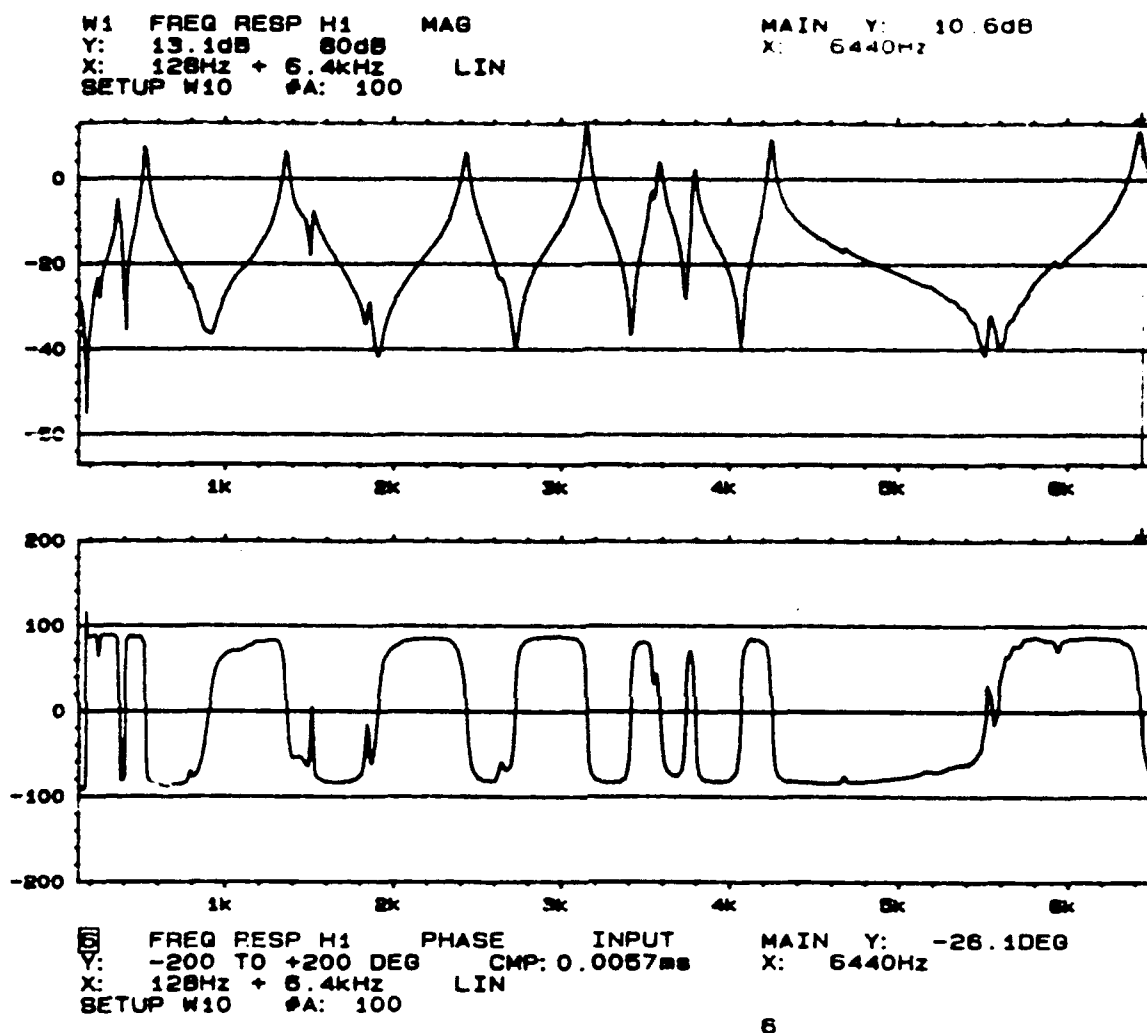
Figure A.11: Drive point mobility of 0.08 inch free composite plate underwater (128-6528 Hz).
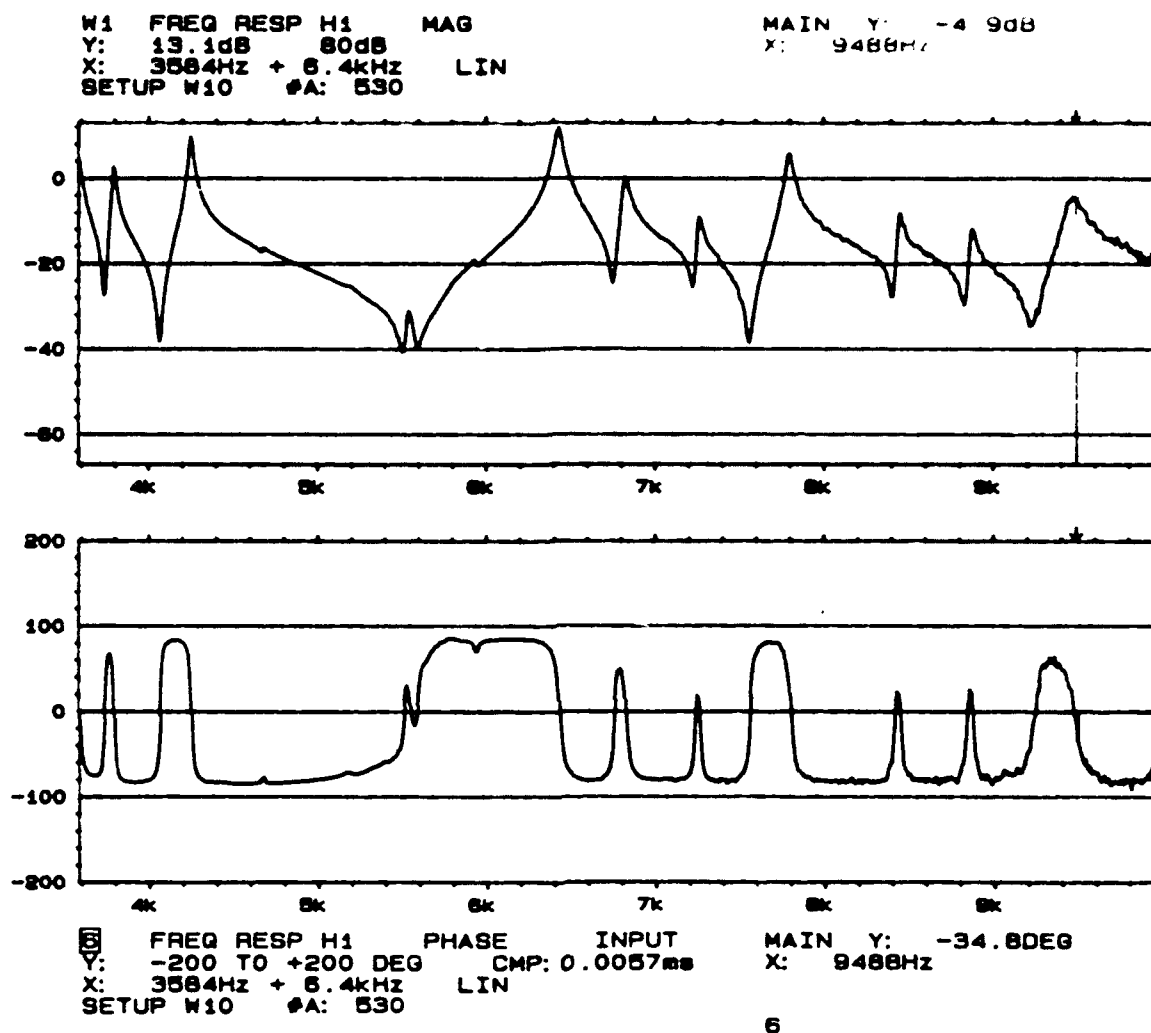
Figure A.12: Drive point mobility of 0.08 inch free composite plate underwater (3584-9984 Hz).
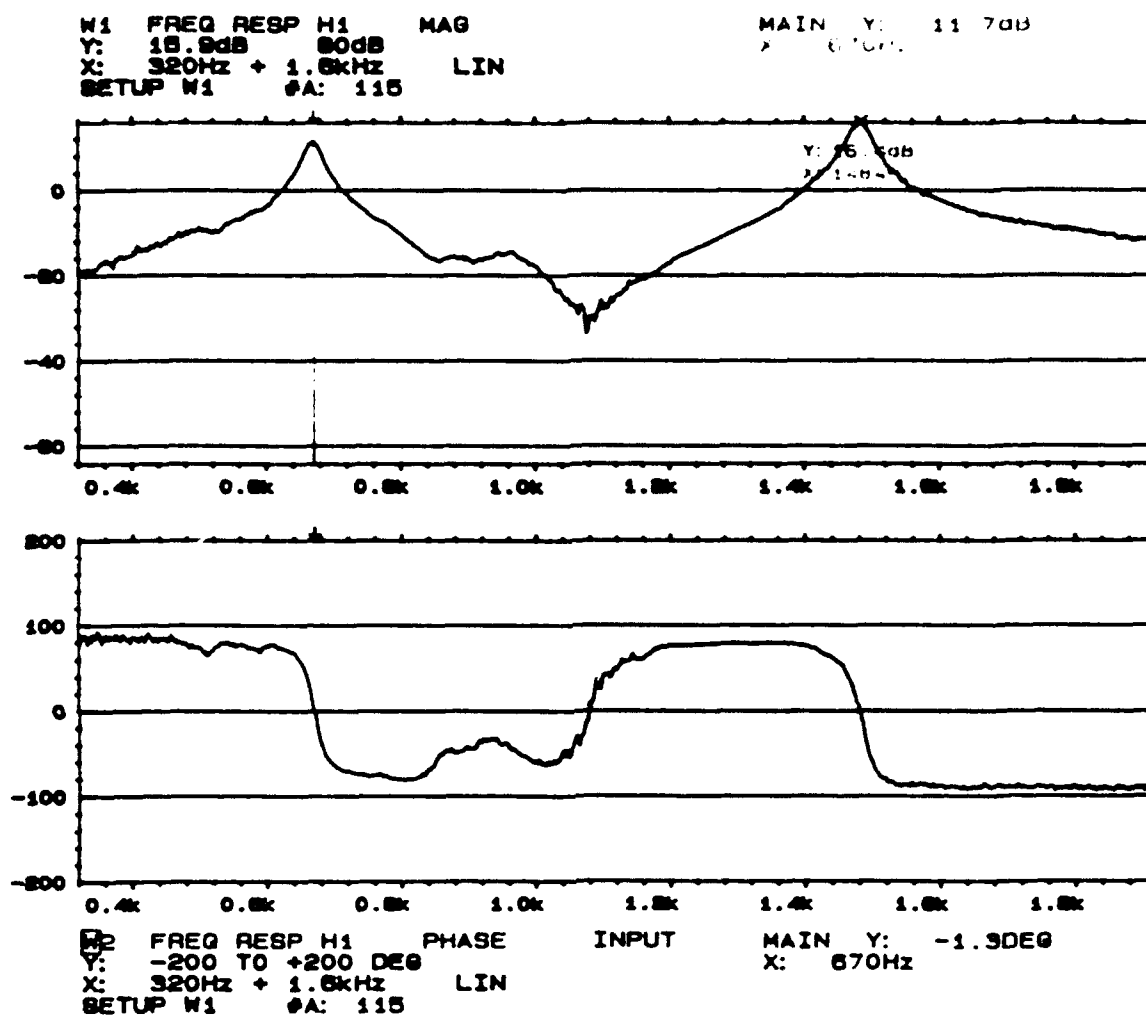
Figure A.13: Drive point mobility of 0.25 inch cantilever
aluminum plate in air (320-1920 Hz).

W1   FREQ RESP H1   MAG   MAIN Y: 22.3dB
Y: 22.3dB   80dB   X:
X: 320Hz + 1.6kHz   LIN
SETUP W1   #A: 284

6   FREQ RESP H1   PHASE   INPUT   MAIN   Y: 5.1DEG
Y: -200 TO +200 DEG   CMP: 0.0228ms   X: 1558Hz
X: 320Hz + 1.6kHz   LIN
SETUP W1   #A: 284

6
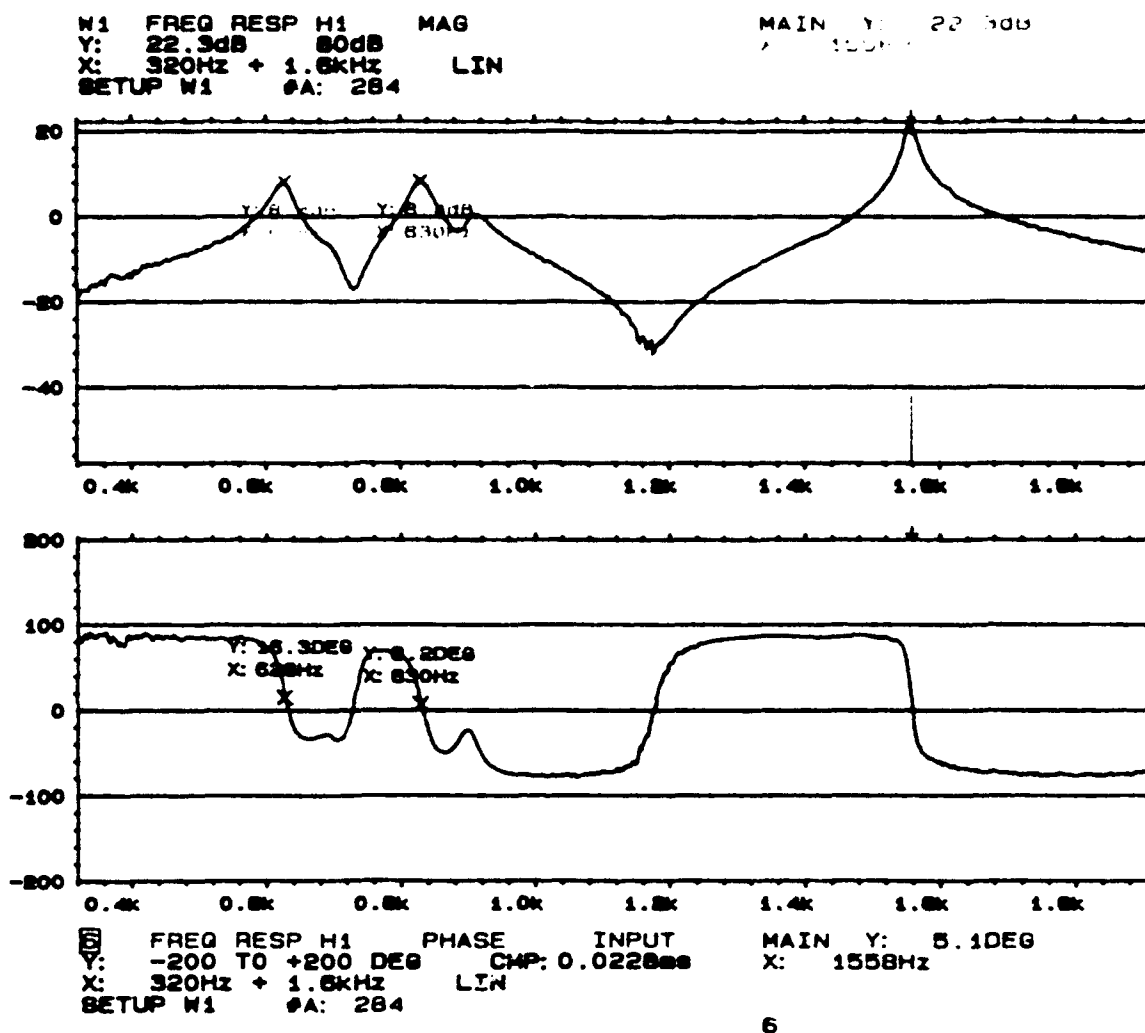
Figure A.14: Drive point mobility of 0.25 inch cantilever
composite plate in air (320-1920 Hz).
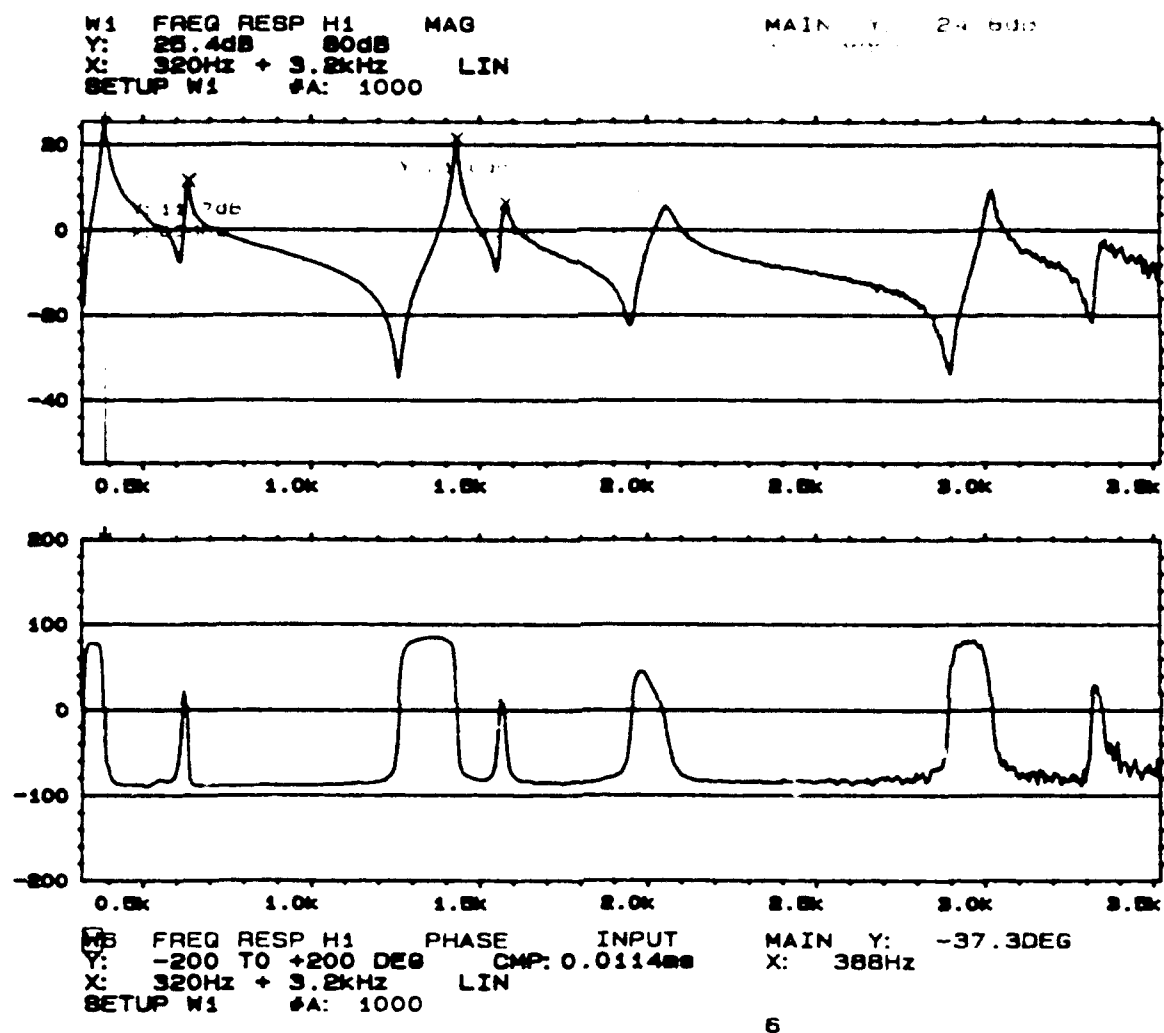
Figure A.15: Drive point mobility of 0.08 inch cantilever
aluminum plate in air (320-3520 Hz).

W1   FREQ RESP H1   MAG   MAIN Y: 18.3dB
Y: 28.4dB   80dB   X: 360Hz
X: 320Hz + 3.2kHz   LIN
SETUP W1   #A: 627

Y: 22.1dB
X: 56Hz

Y: 25.7dB
X: 1348Hz

Y: 14dB
X: 2470Hz

Y: 3.dB
X: 1088Hz

Y: 4.dB
X: 3028Hz

80

0

-20

-40

0.5k   1.0k   1.5k   2.0k   2.5k   3.0k   3.5k

200

100

0

-100

-200

0.5k   1.0k   1.5k   2.0k   2.5k   3.0k   3.5k

W6   FREQ RESP H1   PHASE   INPUT   MAIN Y: -23.1DEG
Y: -200 TO +200 DEG   CMP: 0.0114ms   X: 360Hz
X: 320Hz + 3.2kHz   LIN
SETUP W1   #A: 627
--OVERLOAD IN CH.B--   6
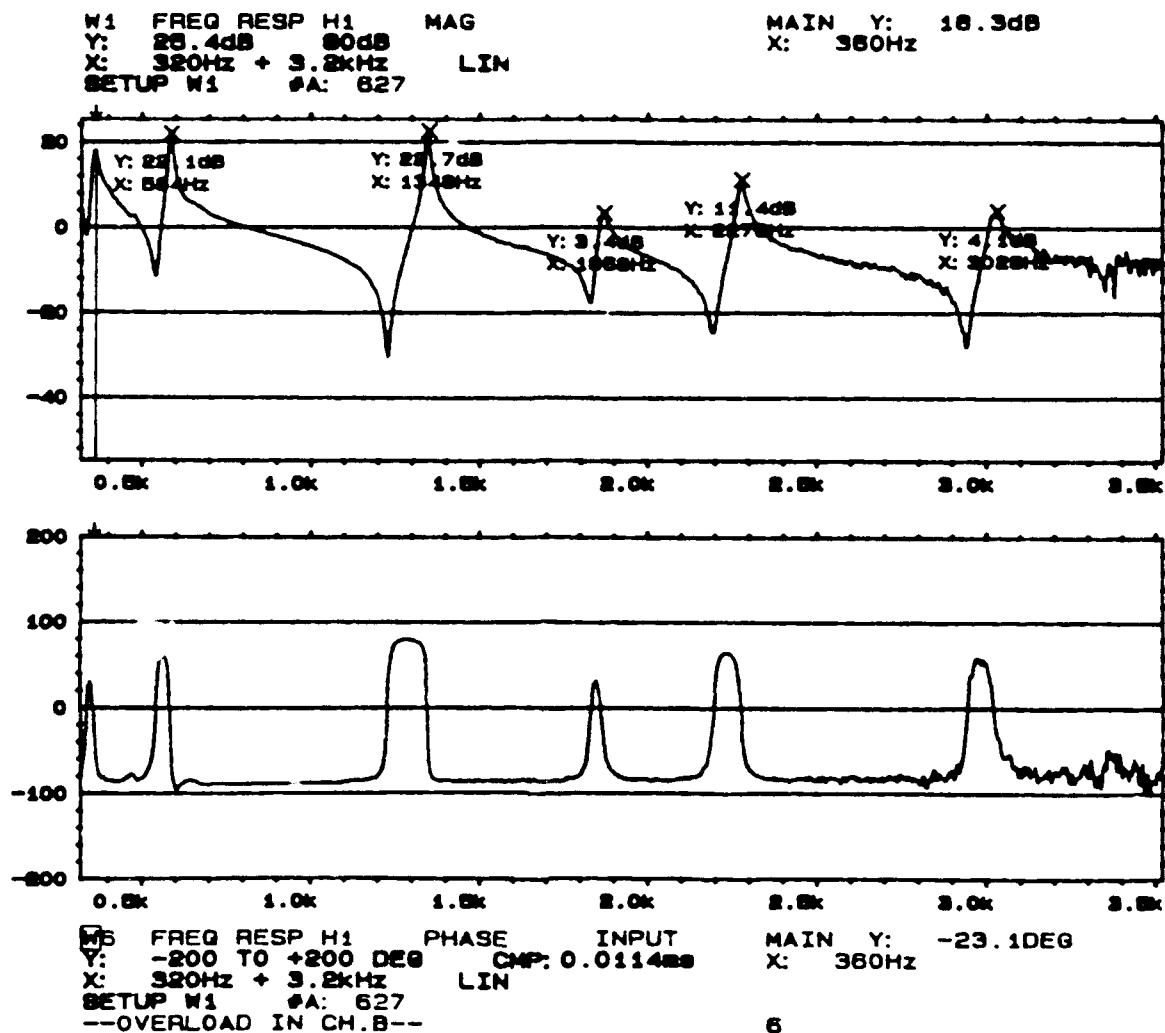
Figure A.16: Drive point mobility of 0.08 inch cantilever
composite plate in air (320-3520 Hz).

W1   FREQ RESP H1   MAG   MAIN   Y: 21.3dB
Y: 46.2dB   60dB   X: 464Hz
X: 320Hz + 3.2kHz   LIN
SETUP W1   #A: 506

```
 40 ┤
    │
    │           Y: 19.8&20.5dB              Y: 17.3dB
    │           X: 896Hz 1064Hz             X: 2968Hz
 20 ┤
    │
  0 ┤
    │
-20 ┤
    │
      0.5k      1.0k      1.5k     2.0k     2.5k      3.0k     3.5k
```

```
200 ┤
    │
100 ┤
    │
  0 ┤
    │
-100┤
    │
-200┤
      0.5k      1.0k      1.5k     2.0k     2.5k      3.0k     3.5k
```

W6   FREQ RESP H1   PHASE   INPUT   MAIN   Y: 7.5DEG
Y: -200 TO +200 DEG   CMP: 0.0114ms   X: 464Hz
X: 320Hz + 3.2kHz   LIN
SETUP W1   #A: 506

6
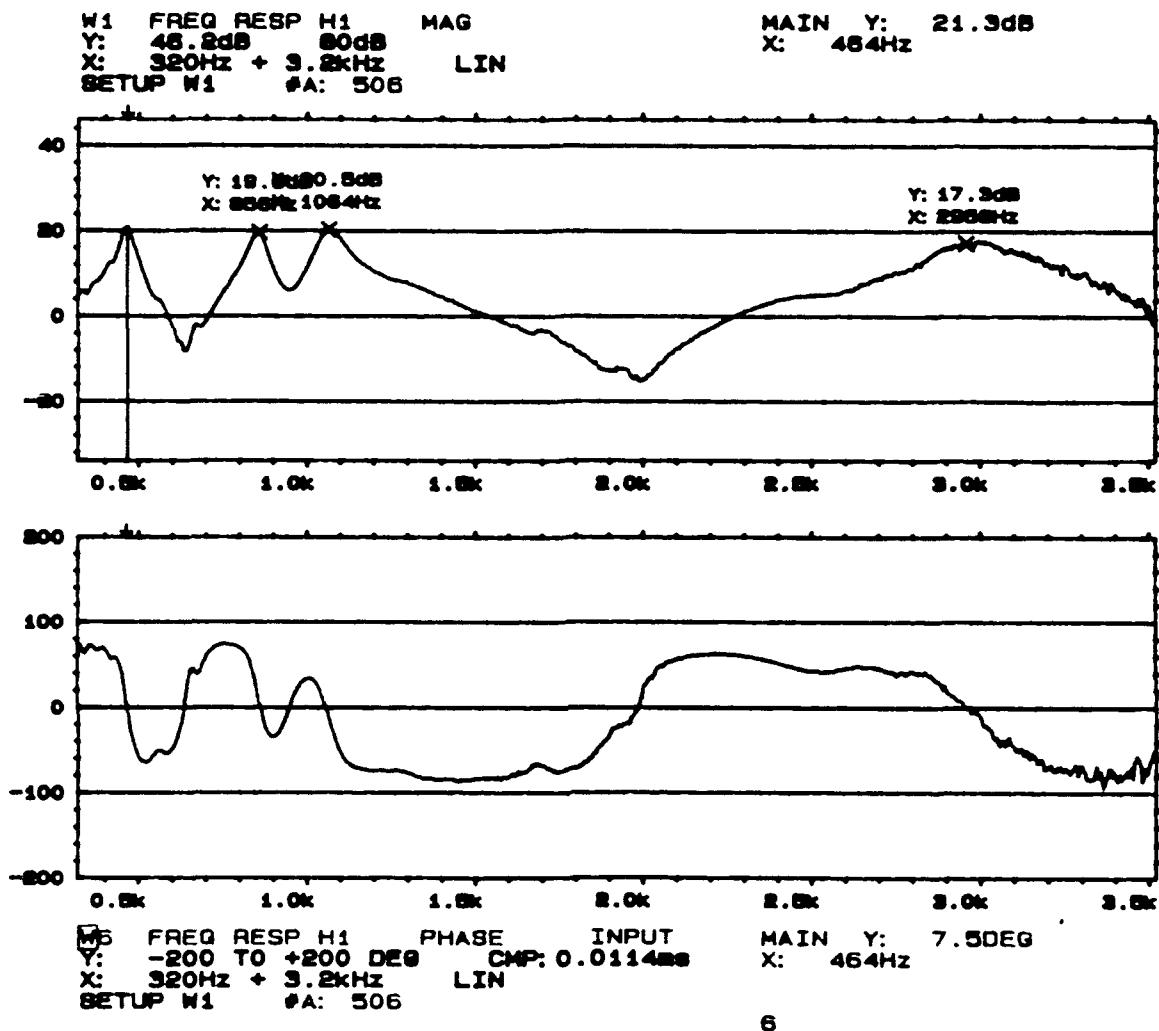
Figure A.17: Drive point mobility of 0.25 inch cantilever
aluminum plate underwater (320-3520 Hz).
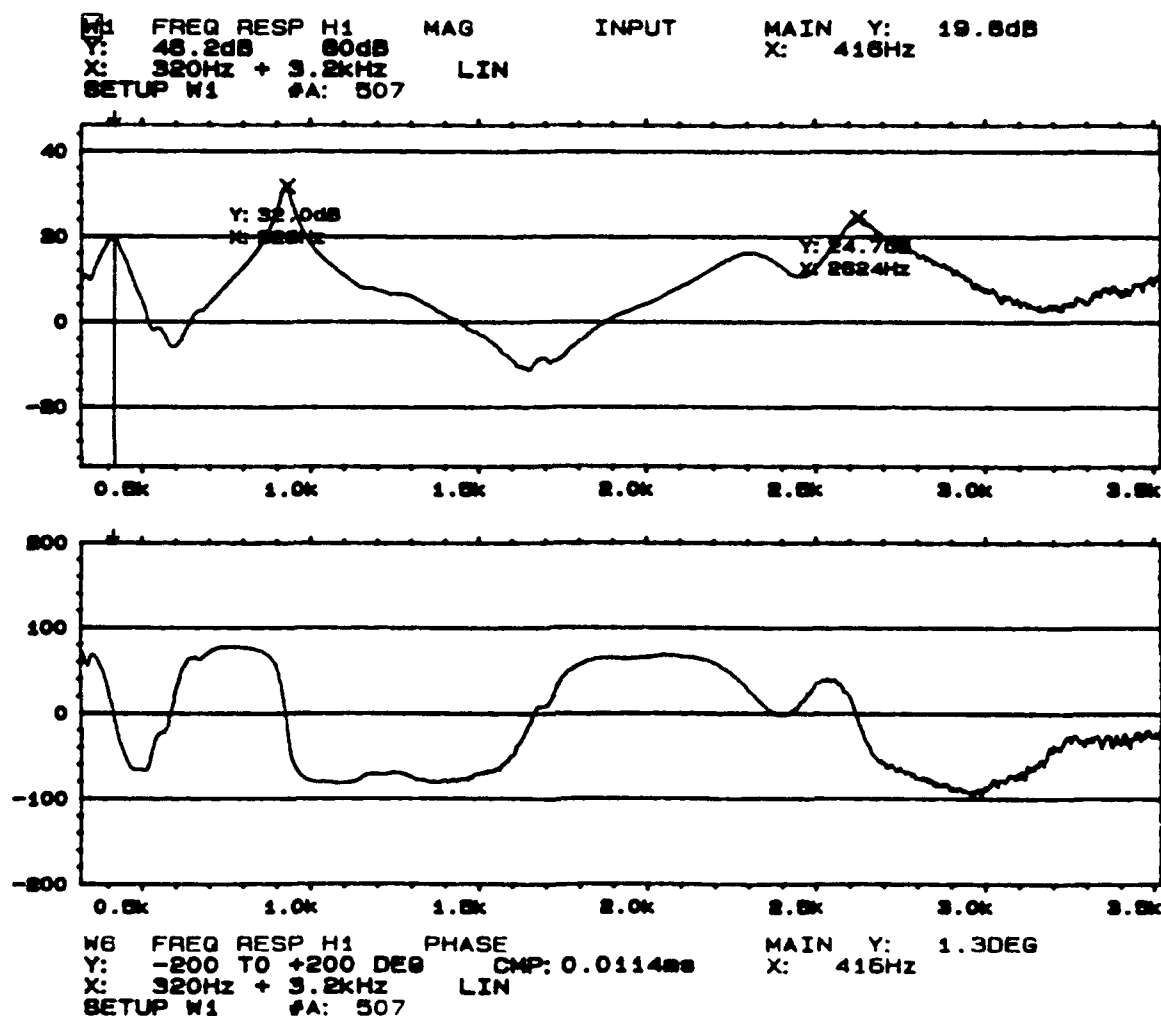
Figure A.18: Drive point mobility of 0.25 inch cantilever
composite plate underwater (320-3520 Hz).
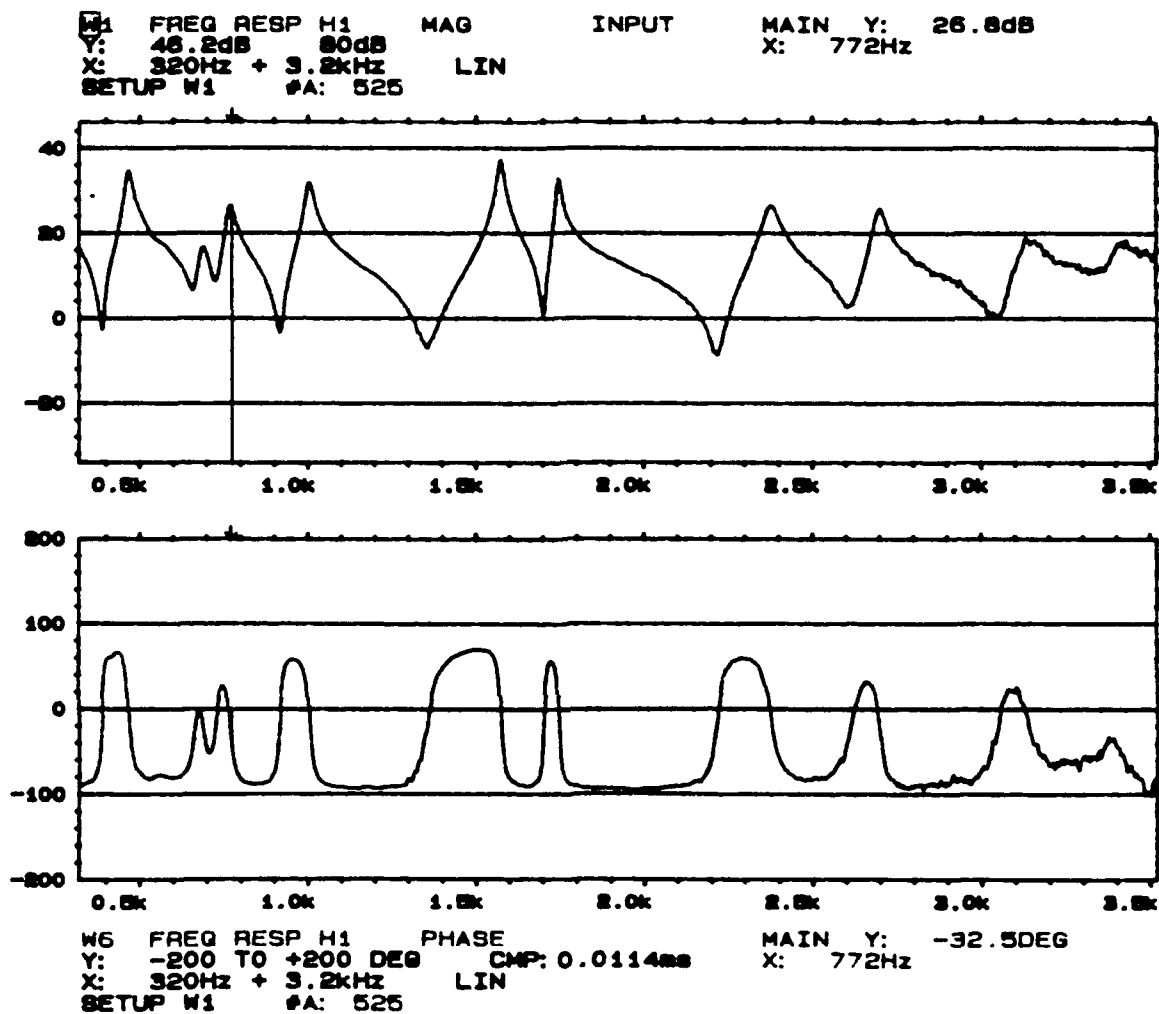
Figure A.19: Drive point mobility of 0.08 inch cantilever
aluminum plate underwater (320-3520 Hz).

W1   FREQ RESP H1   MAG   MAIN   Y: 31.3dB
Y: 46.2dB   80dB   X: 612Hz
X: 320Hz + 3.2kHz   LIN
SETUP W1   #A: 516

W5   FREQ RESP H1   PHASE   INPUT   MAIN   Y: -12.1DEG
Y: -200 TO +200 DEG   CMP: 0.0114ms   X: 612Hz
X: 320Hz + 3.2kHz   LIN
SETUP W1   #A: 516

6
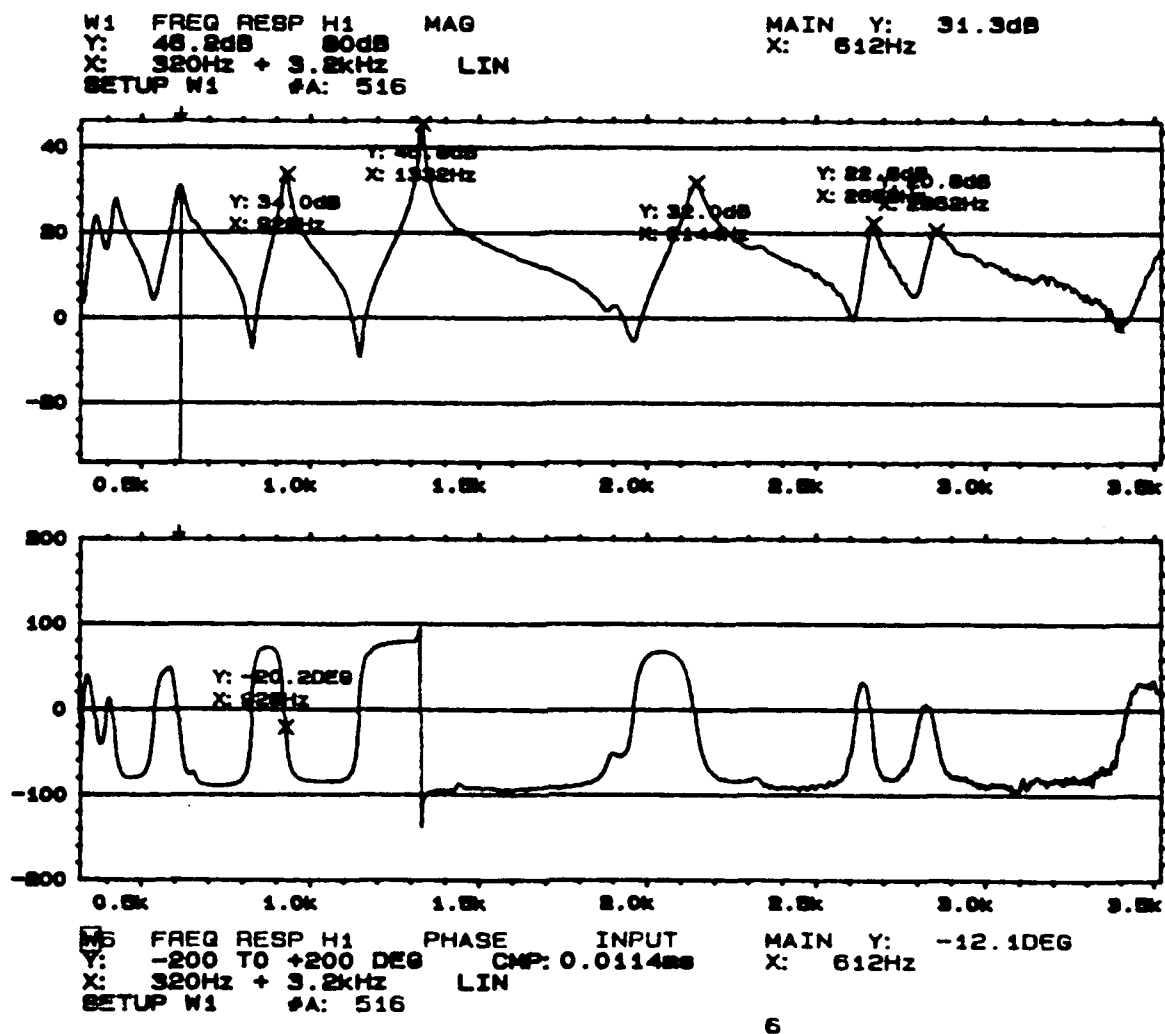
Figure A.20: Drive point mobility of 0.08 inch cantilever
composite plate underwater (320-3520 Hz).

APPENDIX B

EXPERIMENTALLY DETERMINED MODE SHAPES FROM DSPI

The mode shapes obtained from the DSPI experiments in the form of fringe patterns are presented in this appendix. The mode shapes correspond to the frequency data given in section 3.3.3 of this thesis. The correspondence is as follows:

FIGURE NUMBER	CORRESPONDING TABLE OF RESULTS
B.1 - B.3	Table 3.2
B.4 - B.13	Table 3.3
B.14 - B.18	Table 3.4
B.19 - B.32	Table 3.5
B.33 - B.37	Table 3.6
B.38 - B.49	Table 3.7
B.50 - B.54	Table 3.8
B.55 - B.68	Table 3.9
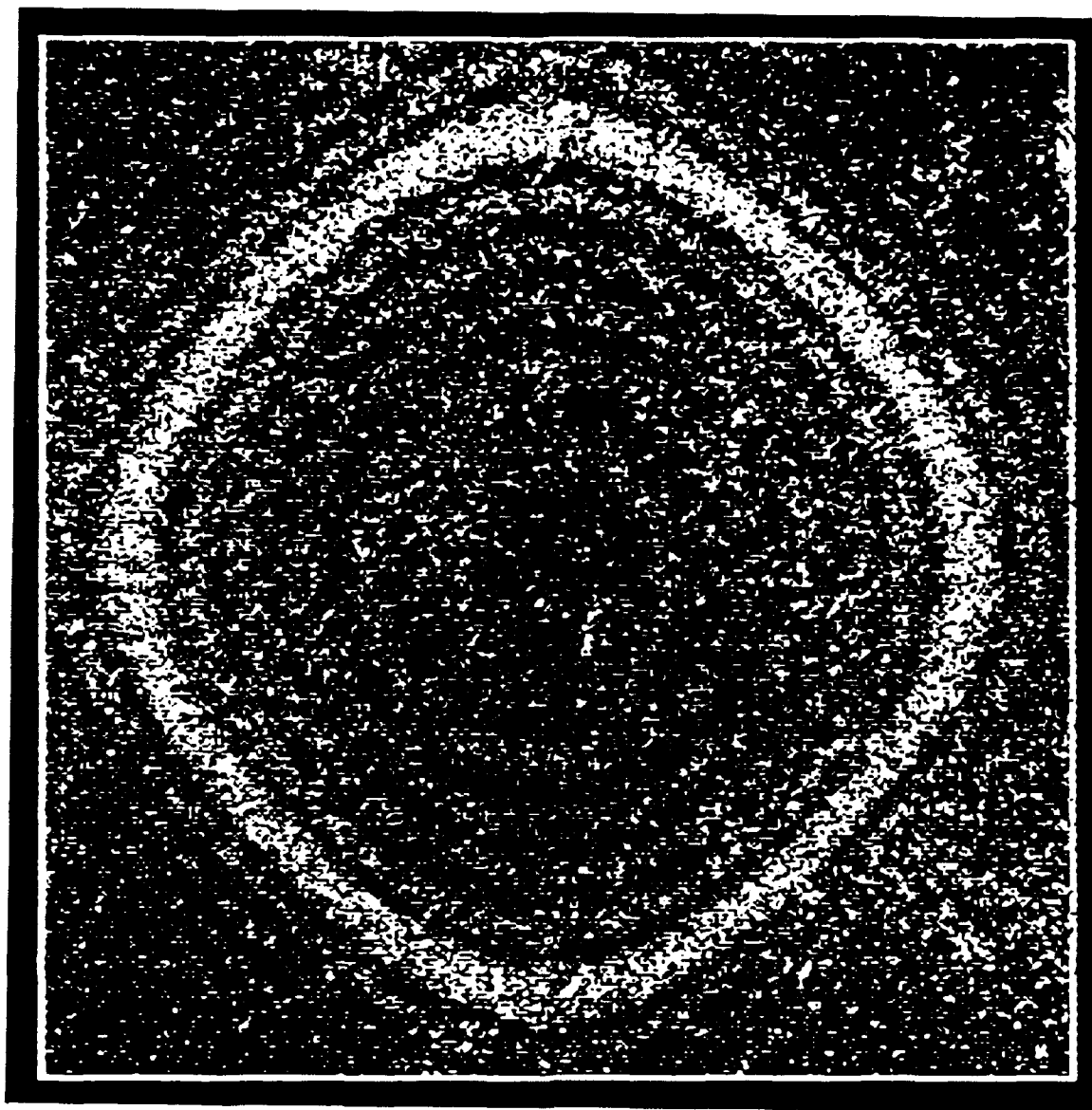
Figure B.1: A 0.25" free aluminum plate in air: vibrating at
3912 Hz (0,2 mode).
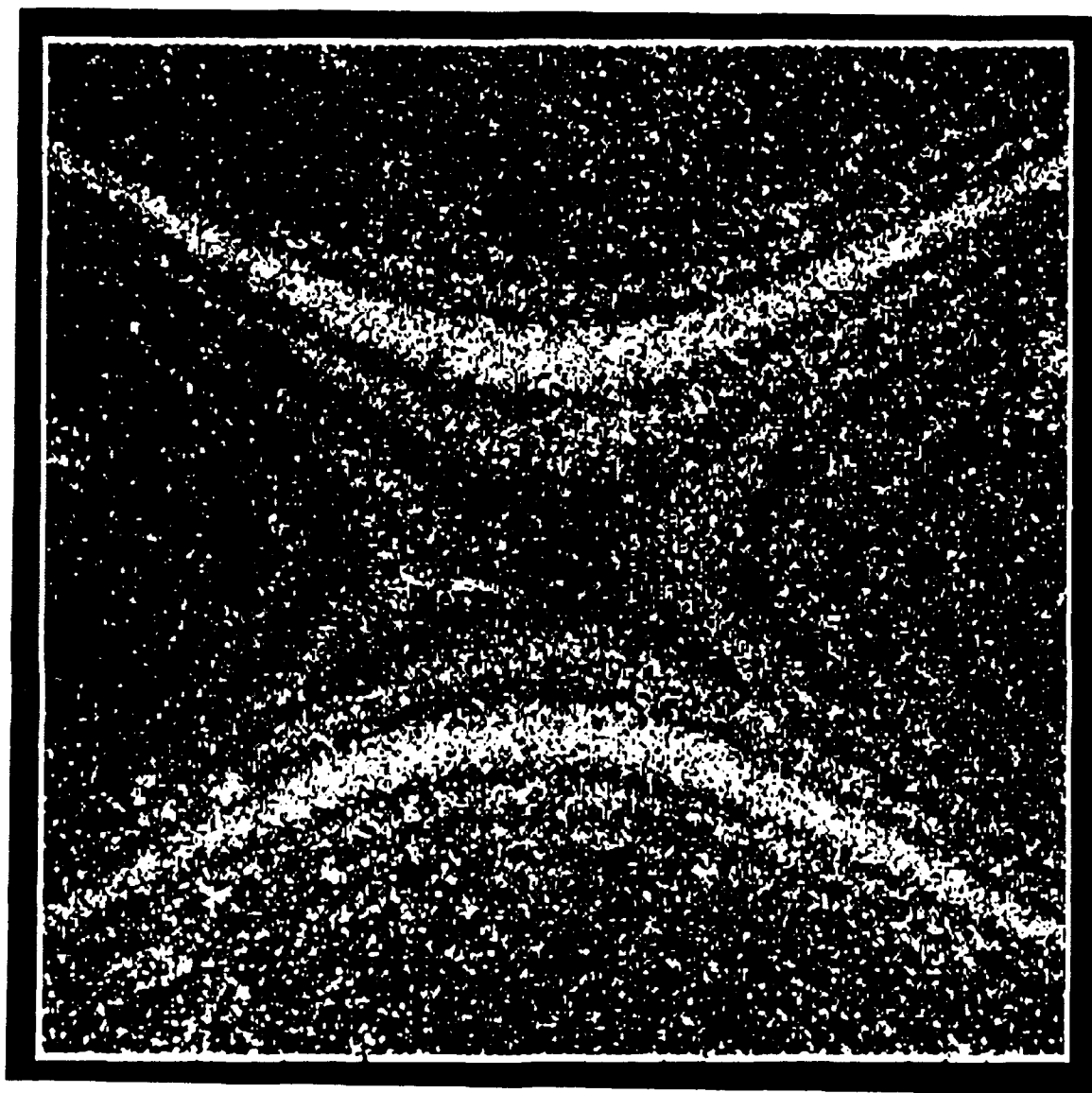
Figure B.2: A 0.25" free composite plate in air: vibrating at 3592 Hz.
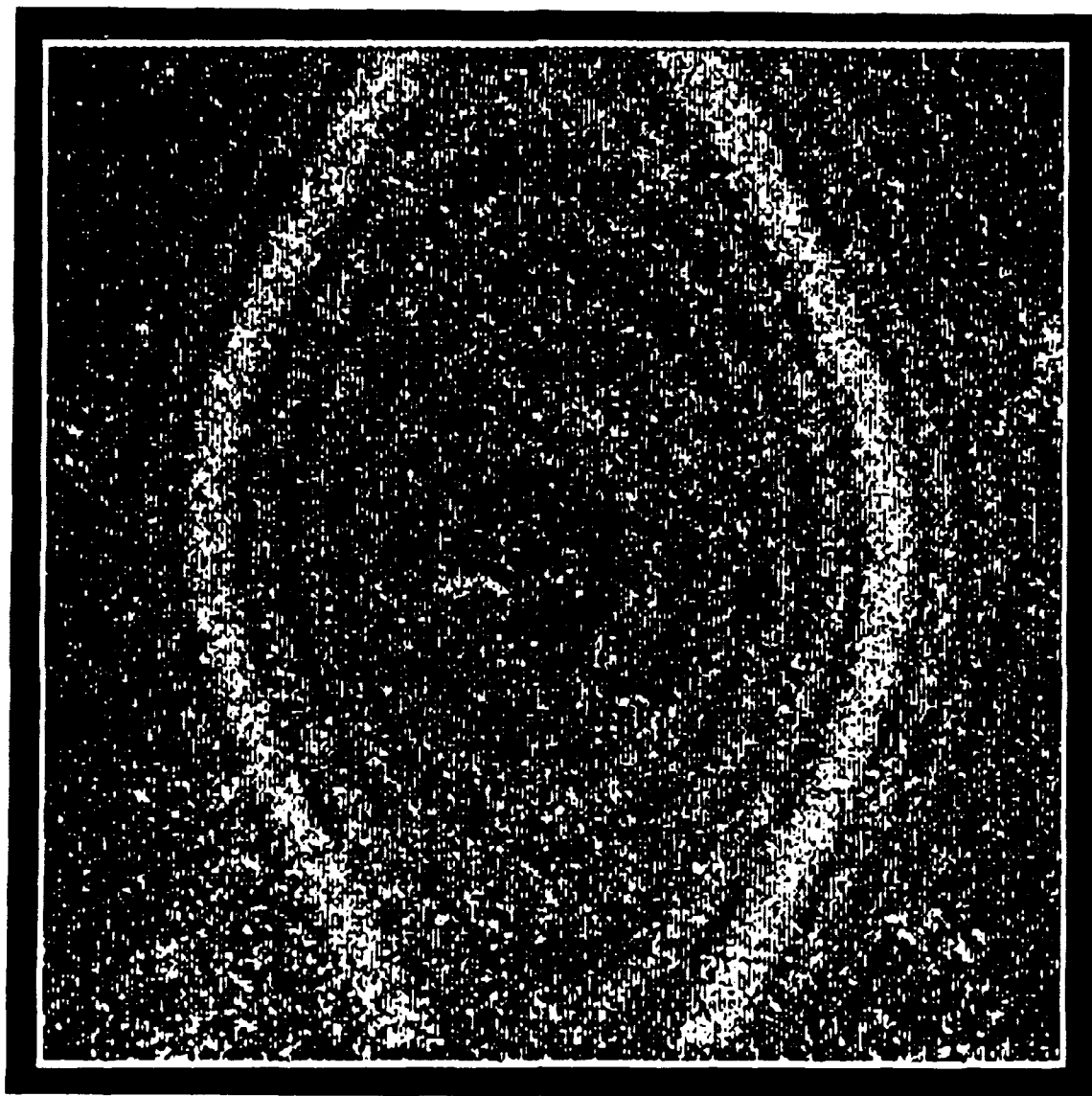
Figure B.3: A 0.25" free composite plate in air: vibrating at 4314 Hz.
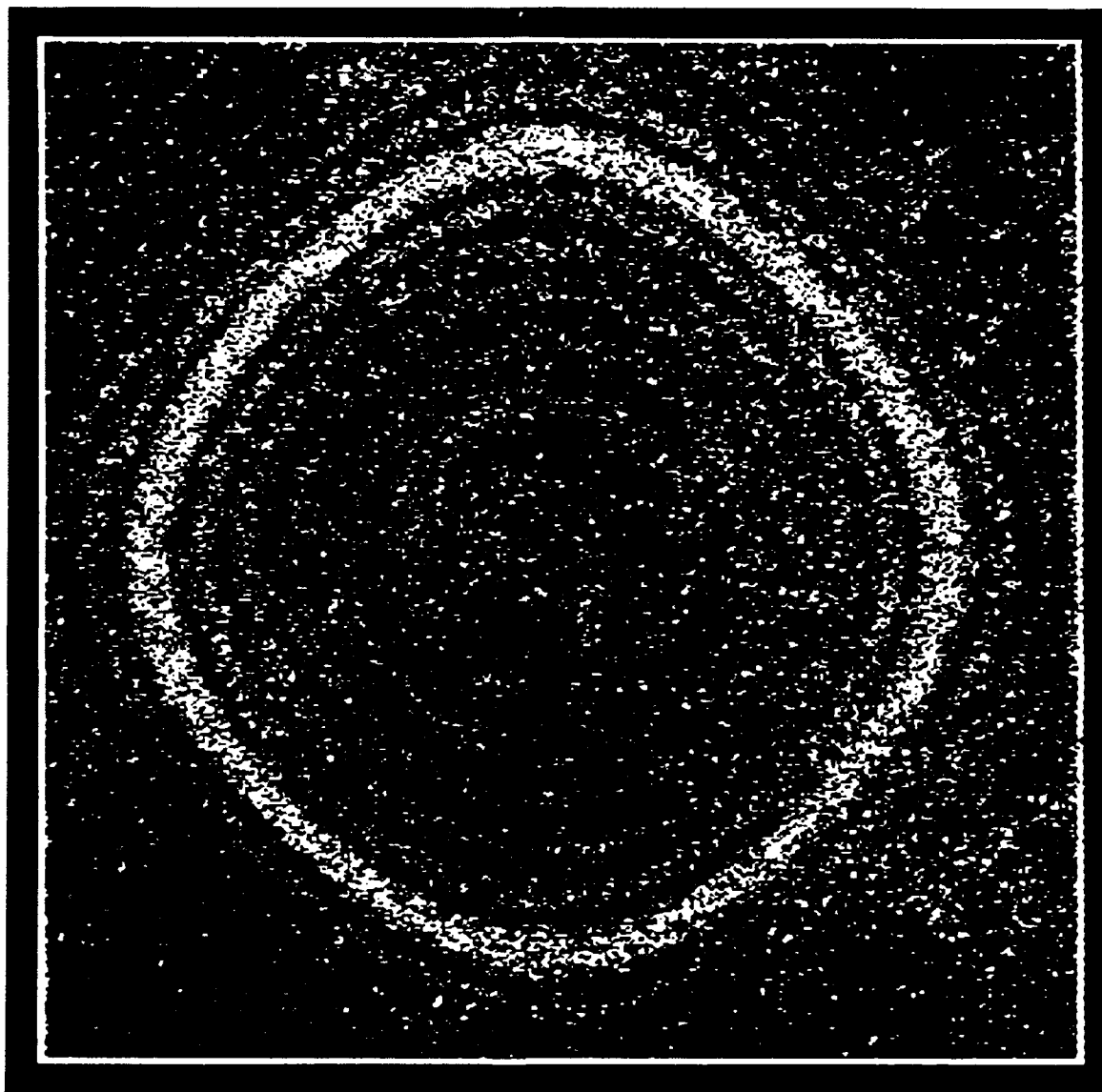
Figure B.4: A 0.08" free aluminum plate in air: vibrating at 1089 Hz (0,2 mode).
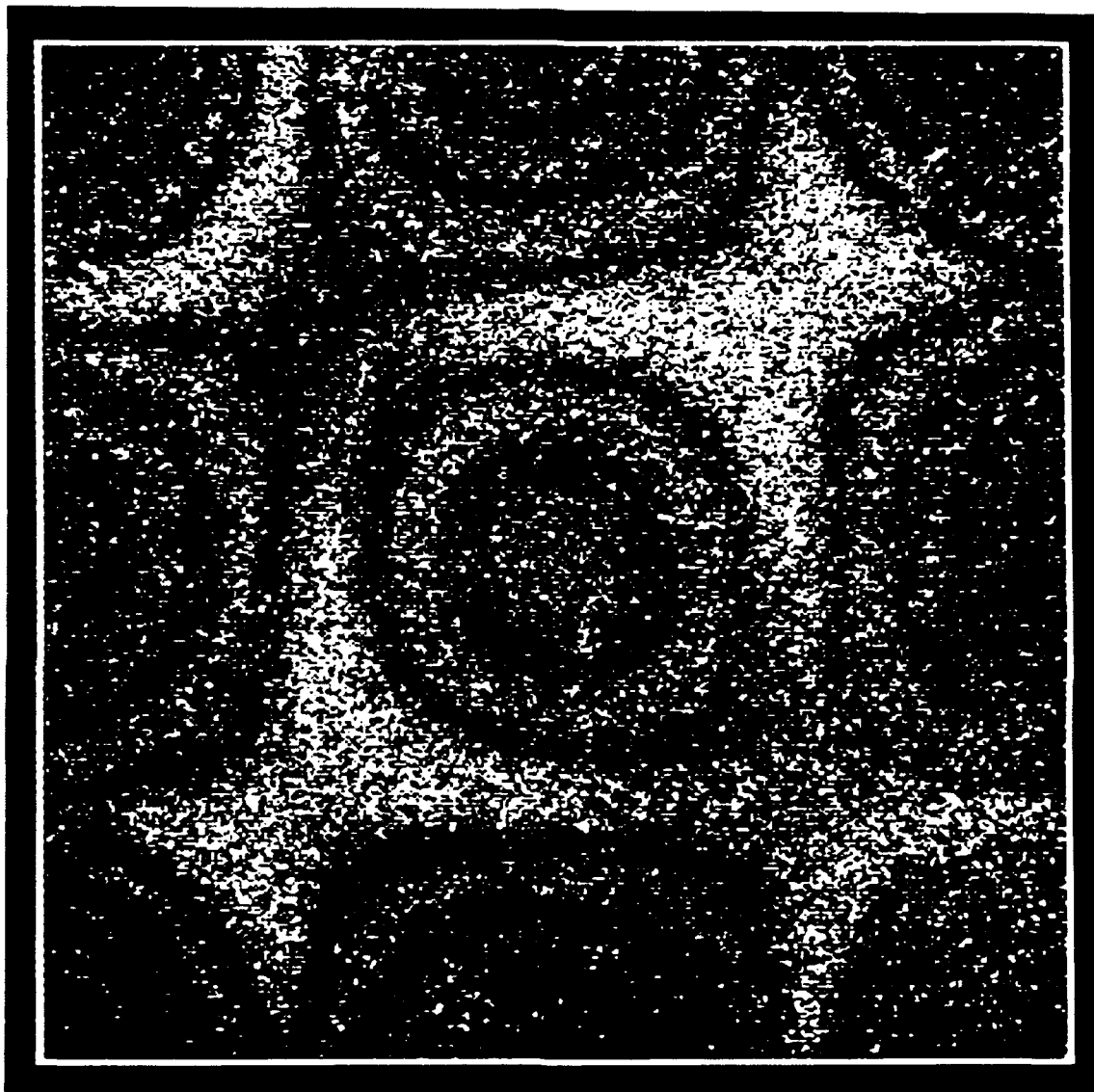
Figure B.5: A 0.08" free aluminum plate in air: vibrating at 2788 Hz (2,2 mode).
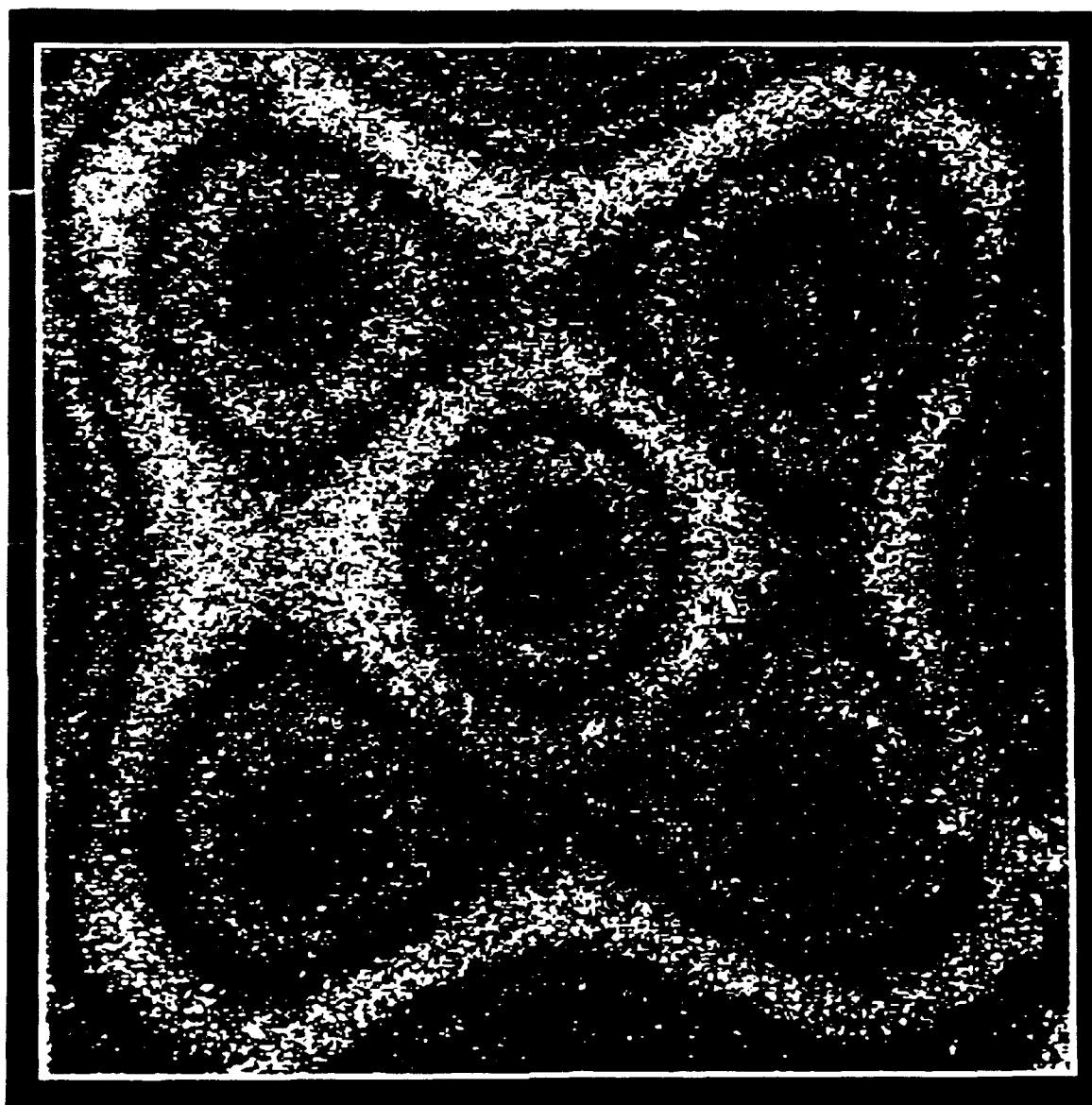
Figure B.6: A 0.08" free aluminum plate in air: vibrating at 5281 Hz (0,4 mode).
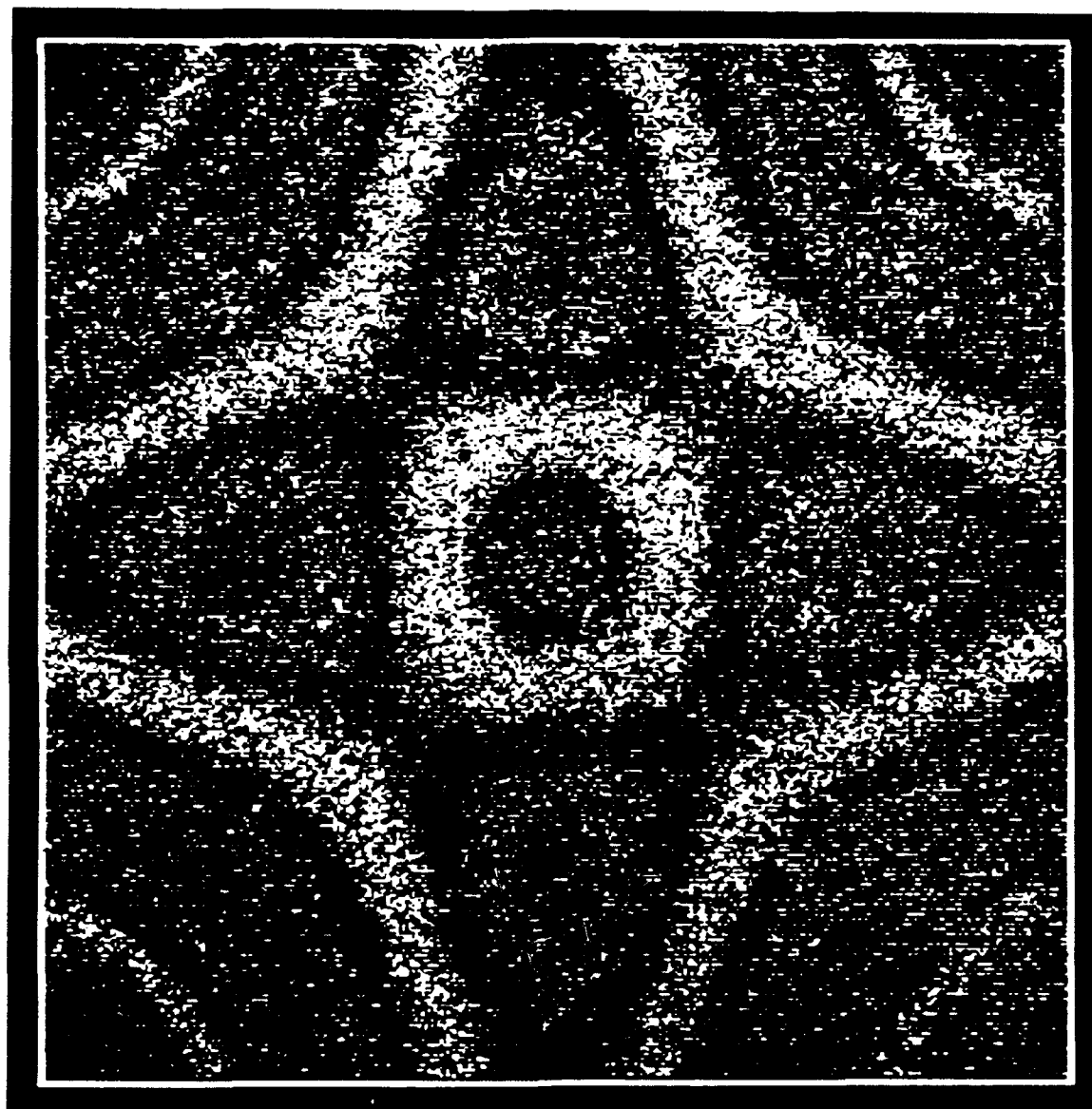
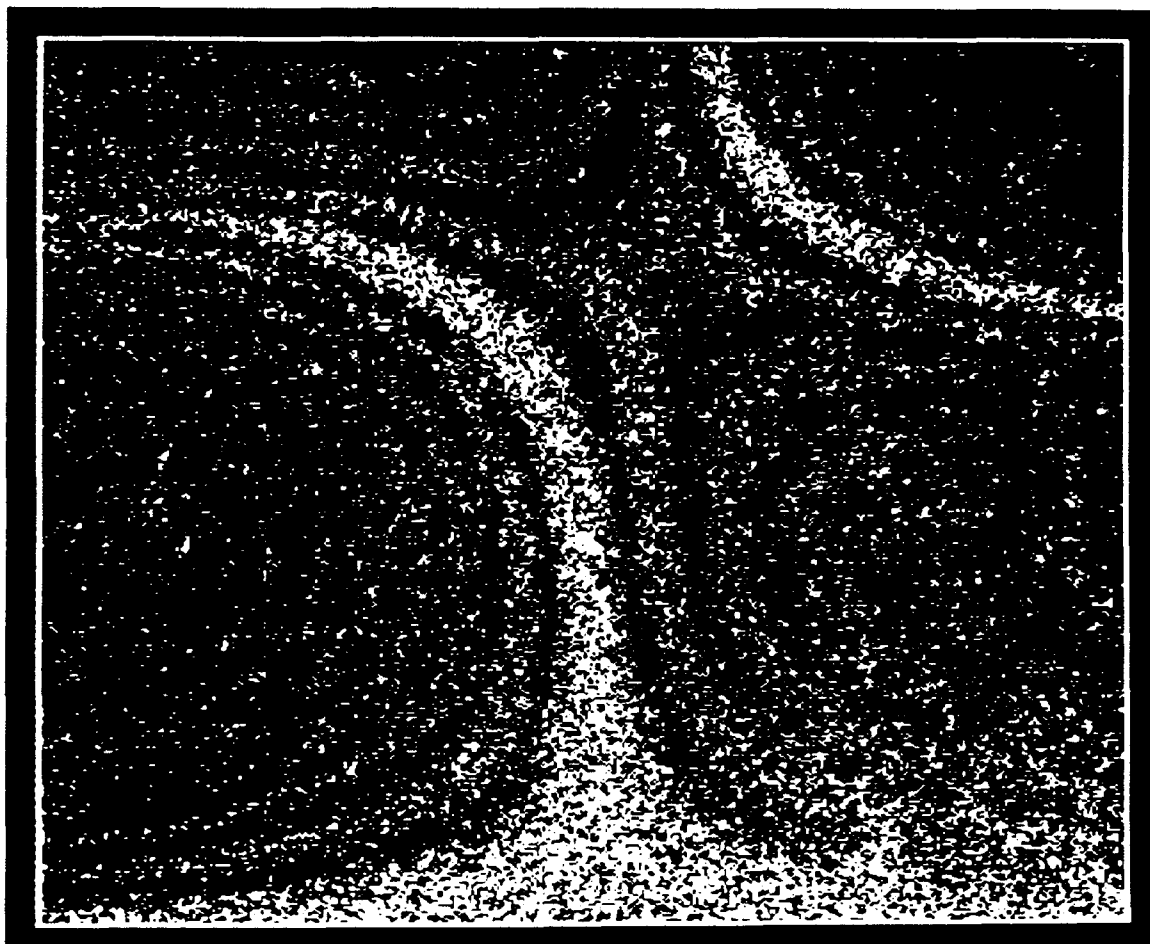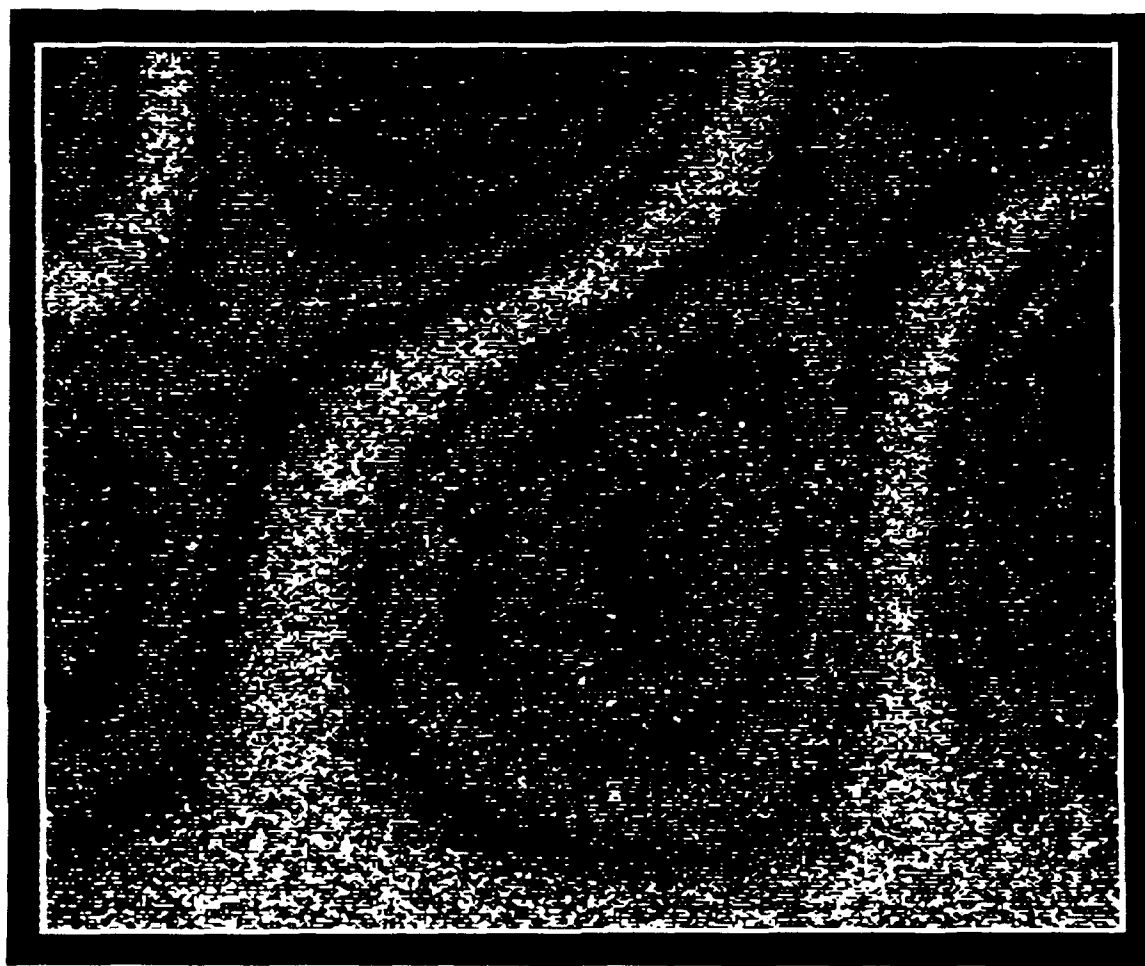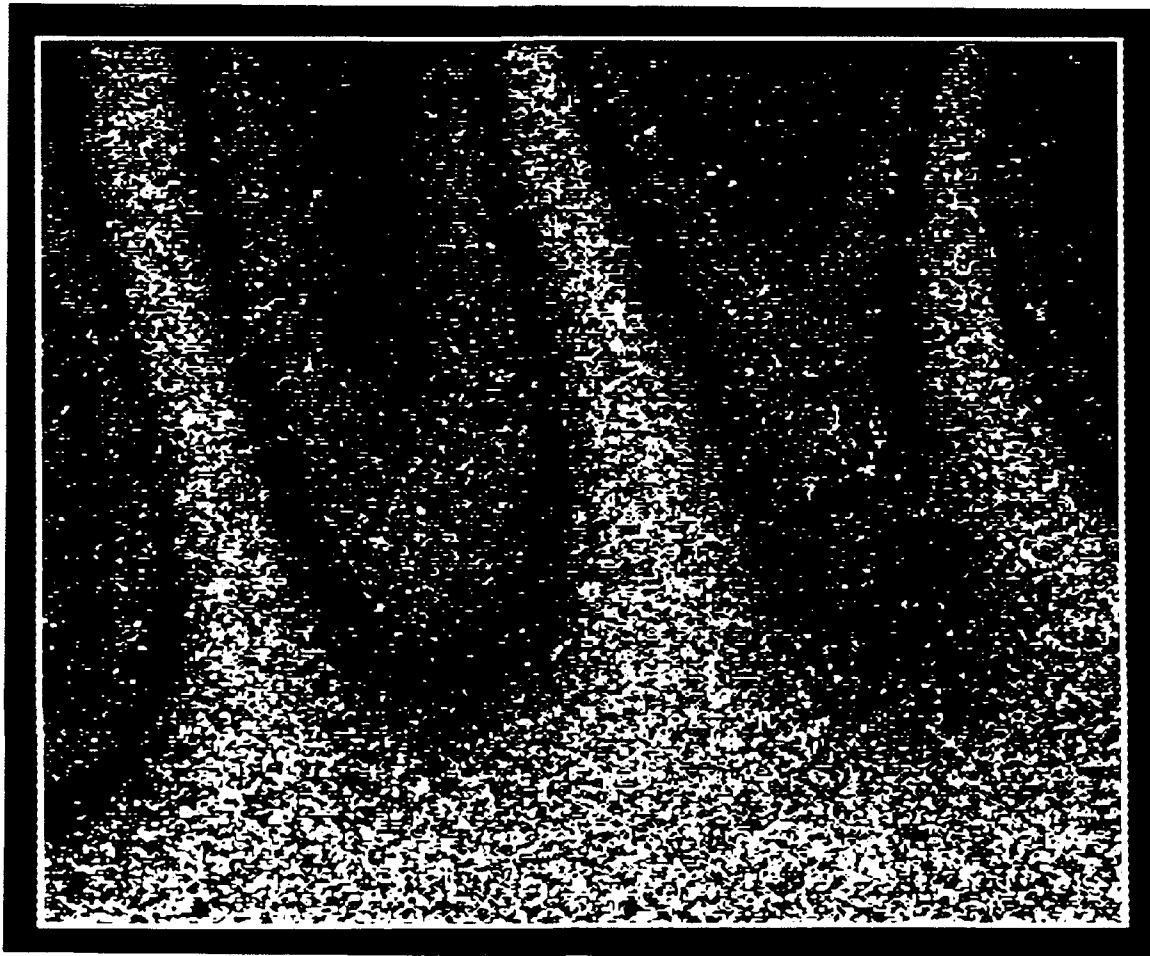Figure B.7: A 0.08" free aluminum plate in air: vibrating at 7335 Hz (2,4 mode).

108
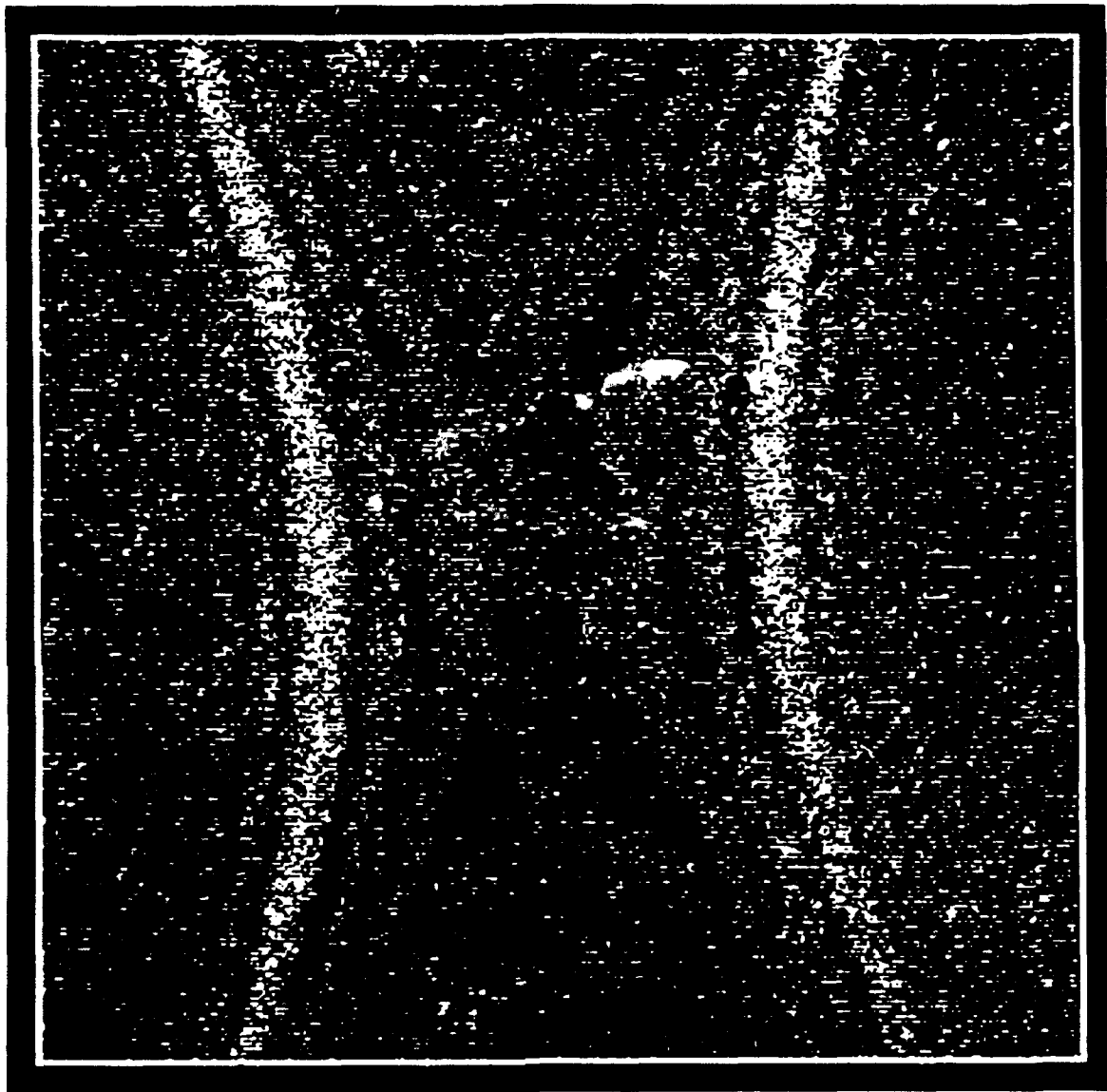
Figure B.8: A 0.08" free composite plate in air: vibrating at 921 Hz.
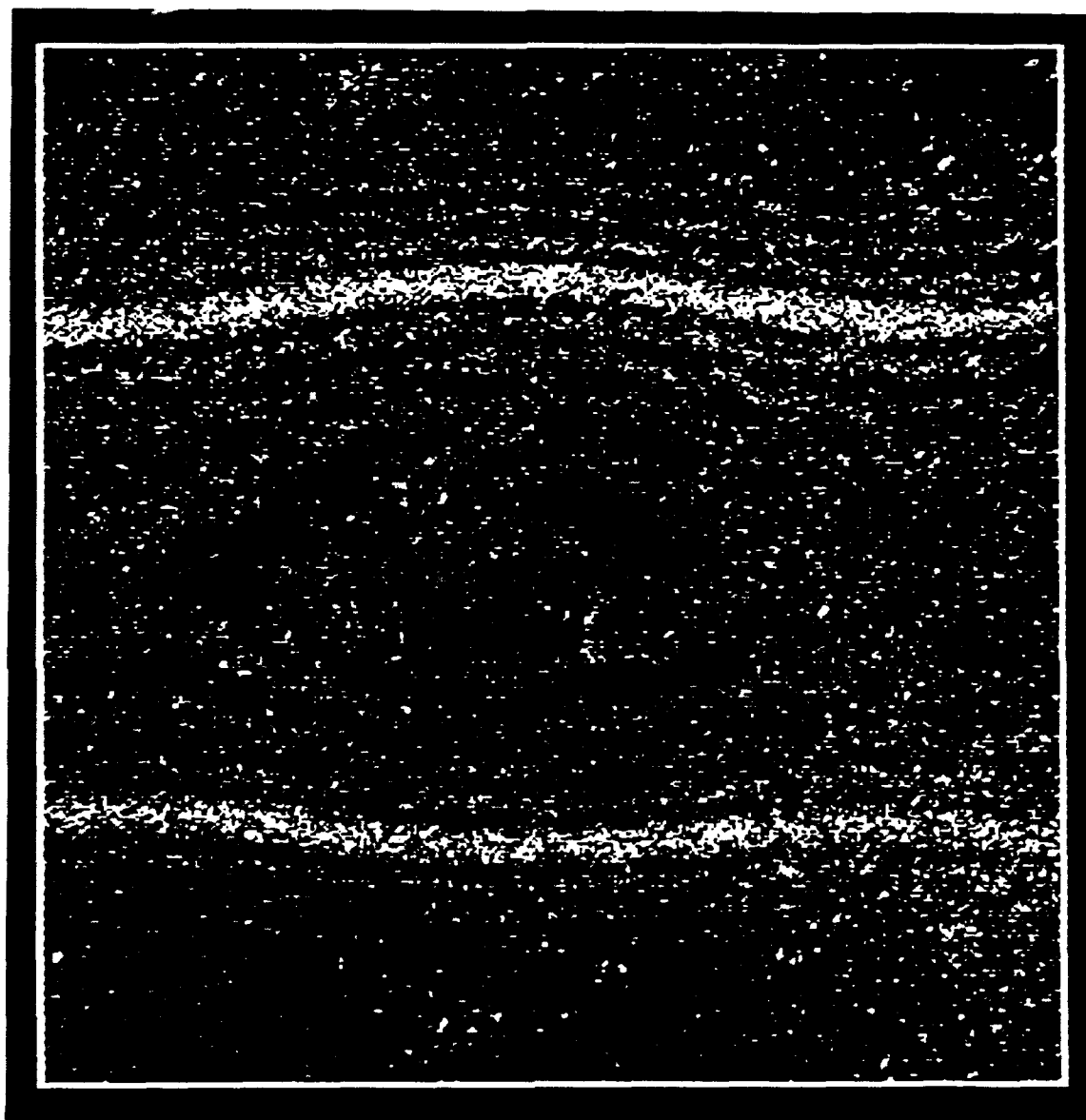
Figure B.9: A 0.08"   free composite plate in air: vibrating at 1240 Hz.
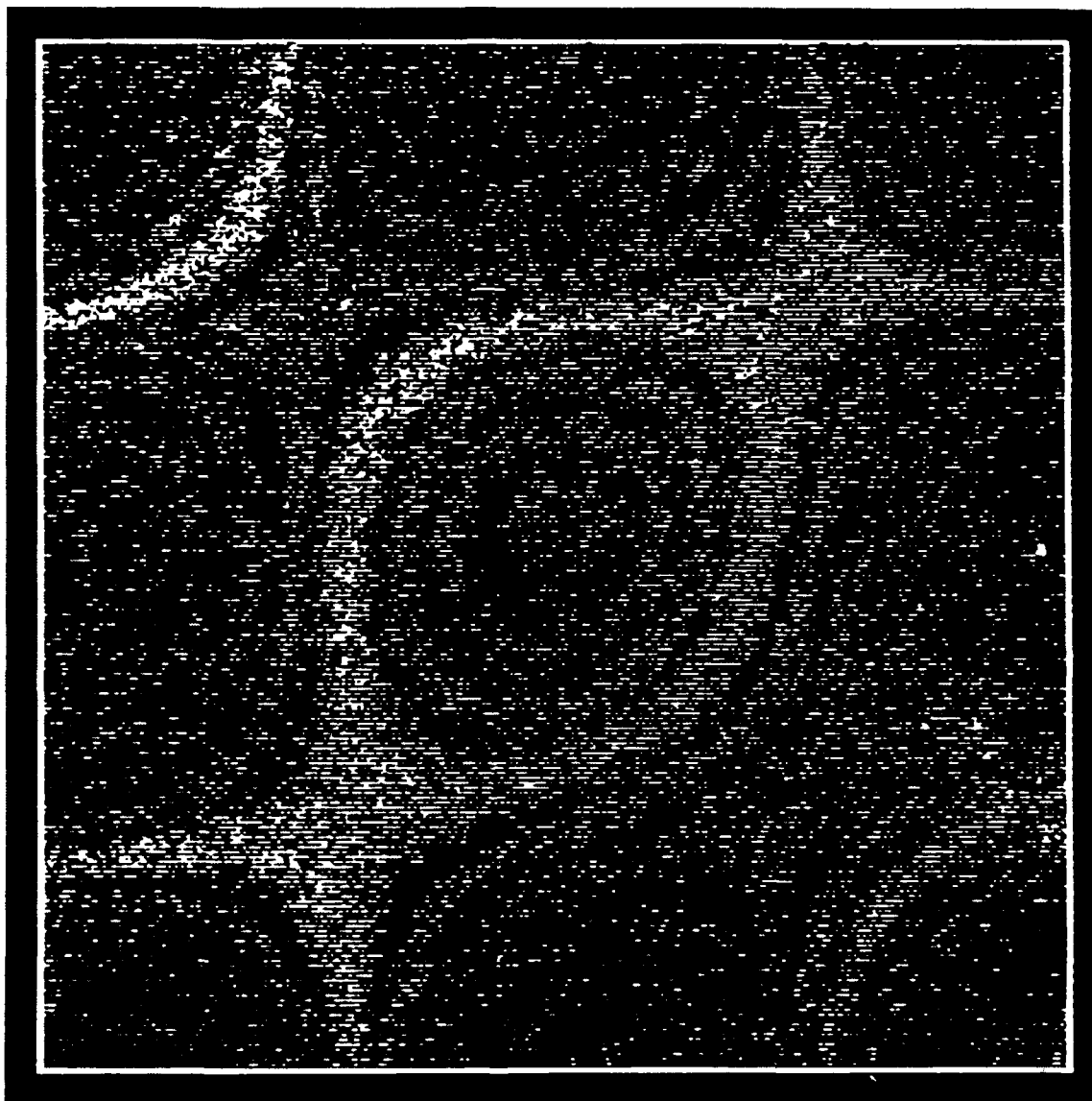
Figure B.10: A 0.08" free composite plate in air: vibrating at 2819 Hz.
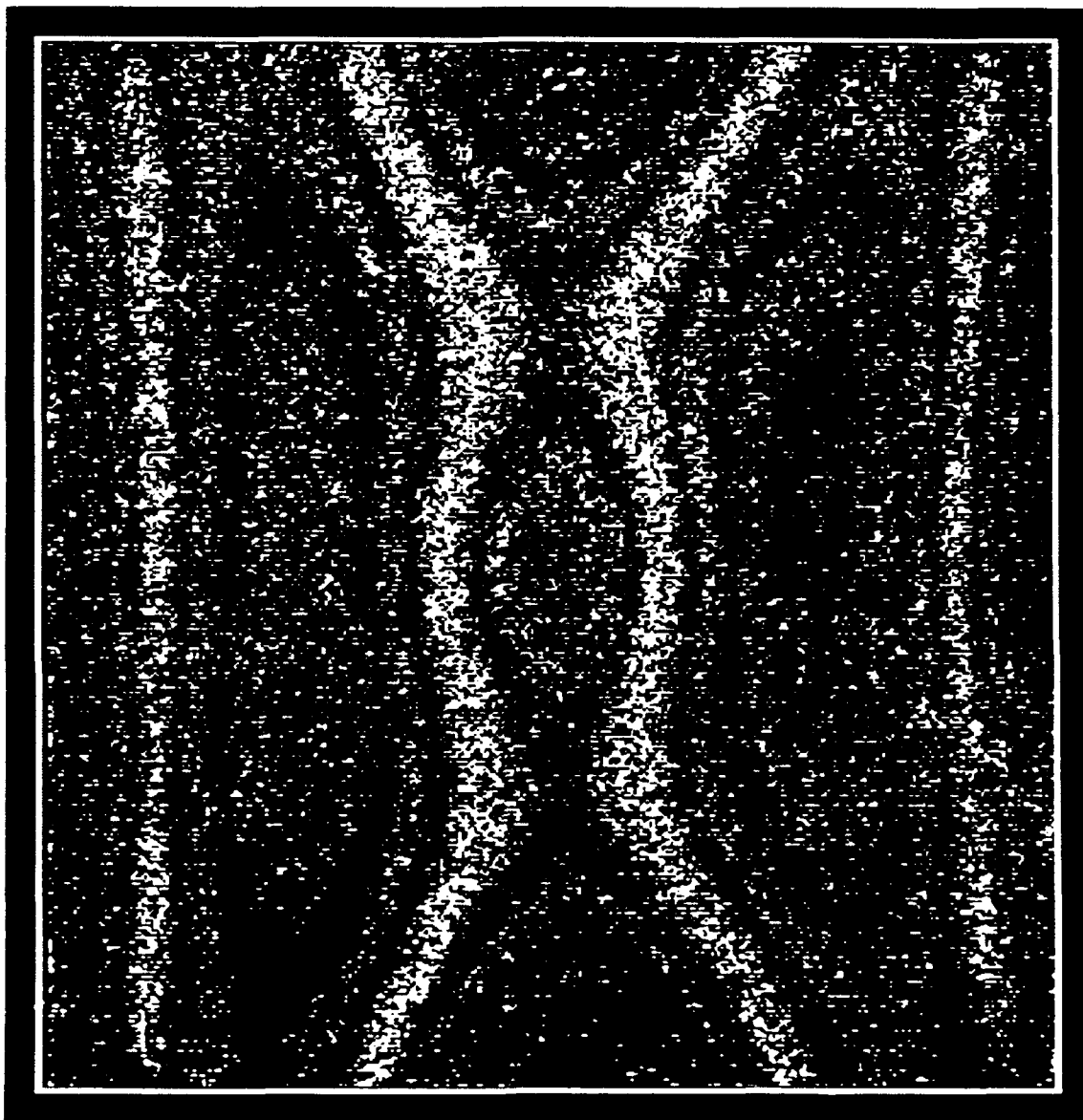
Figure B.11: A 0.08" free composite plate in air: vibrating at 972 Hz.
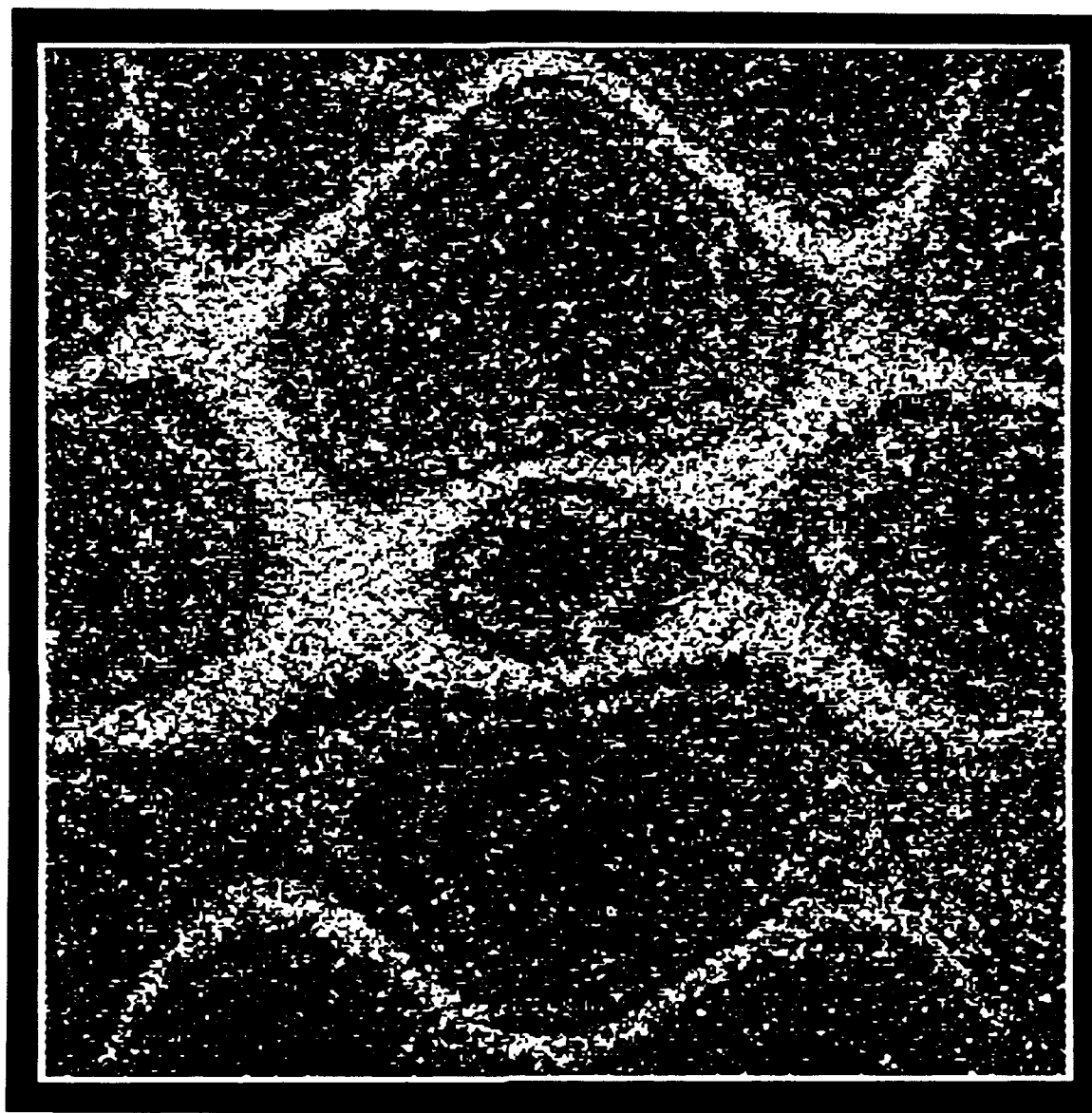
Figure B.12: A 0.08" free composite plate in air: vibrating at 6294 Hz.
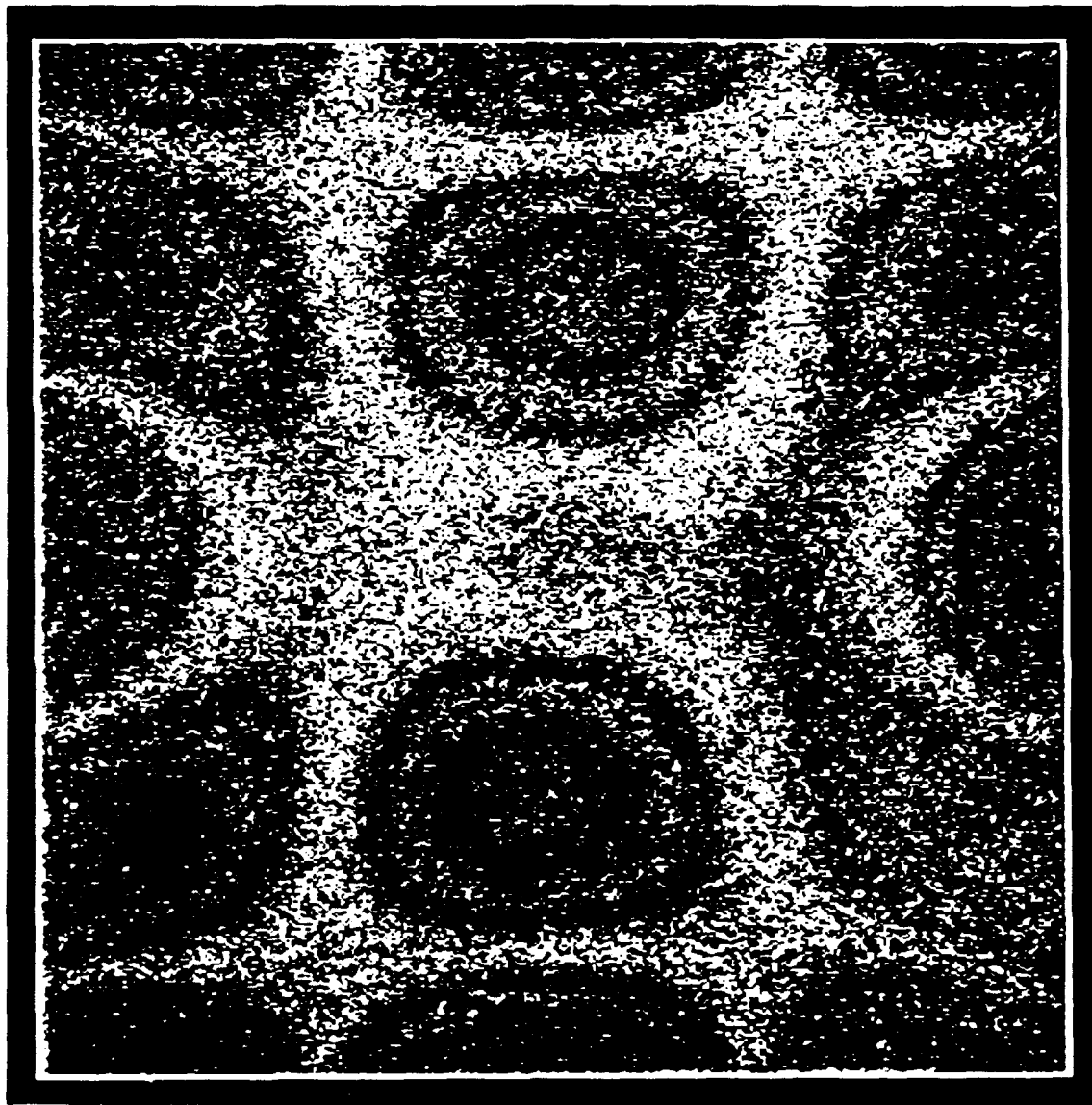
Figure B.13: A 0.08" free composite plate in air: vibrating at 8393 Hz.

114
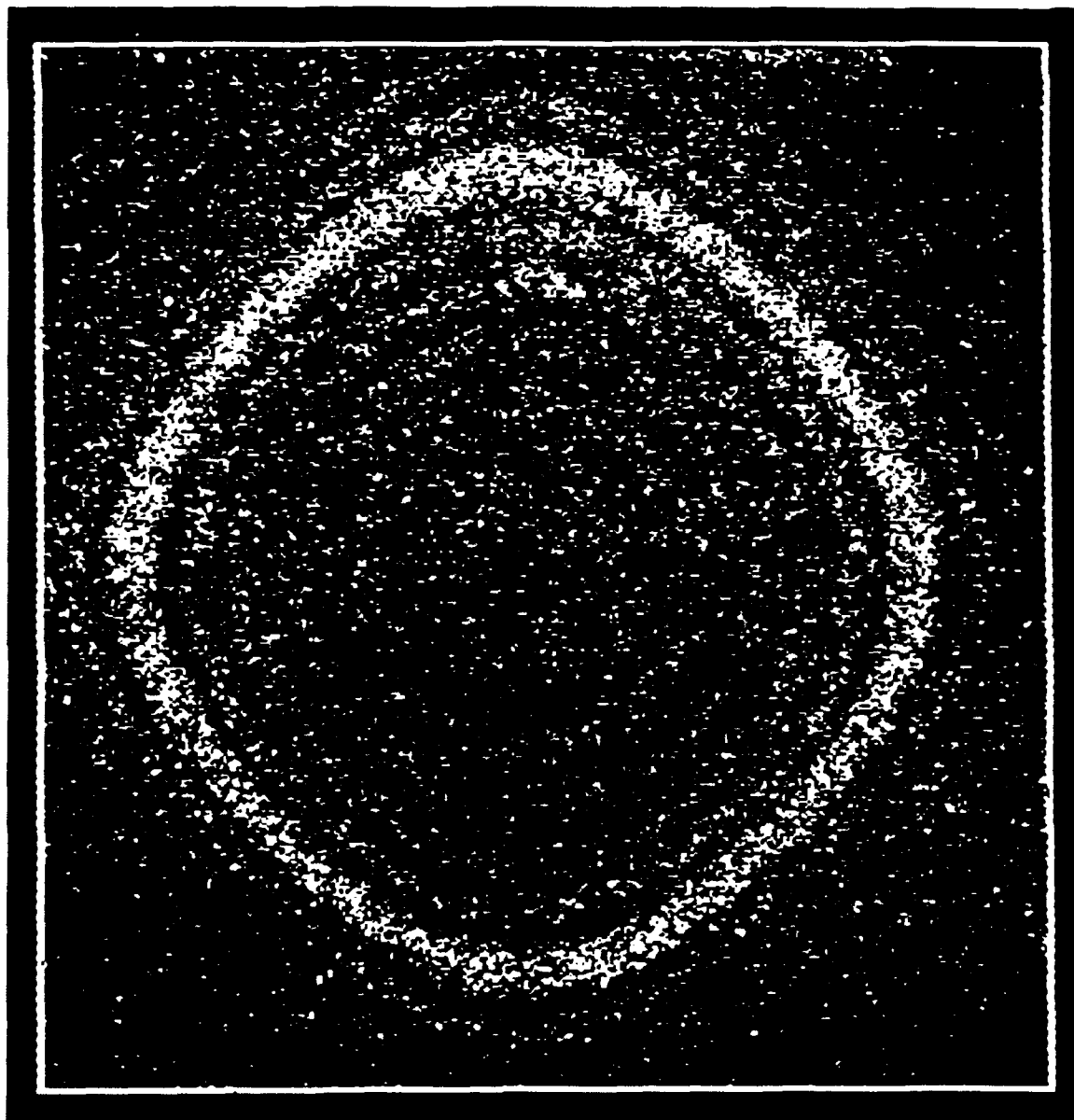
Figure B.14: A 0.25" free aluminum plate underwater: vibrating at 2837 Hz (0,2 mode).
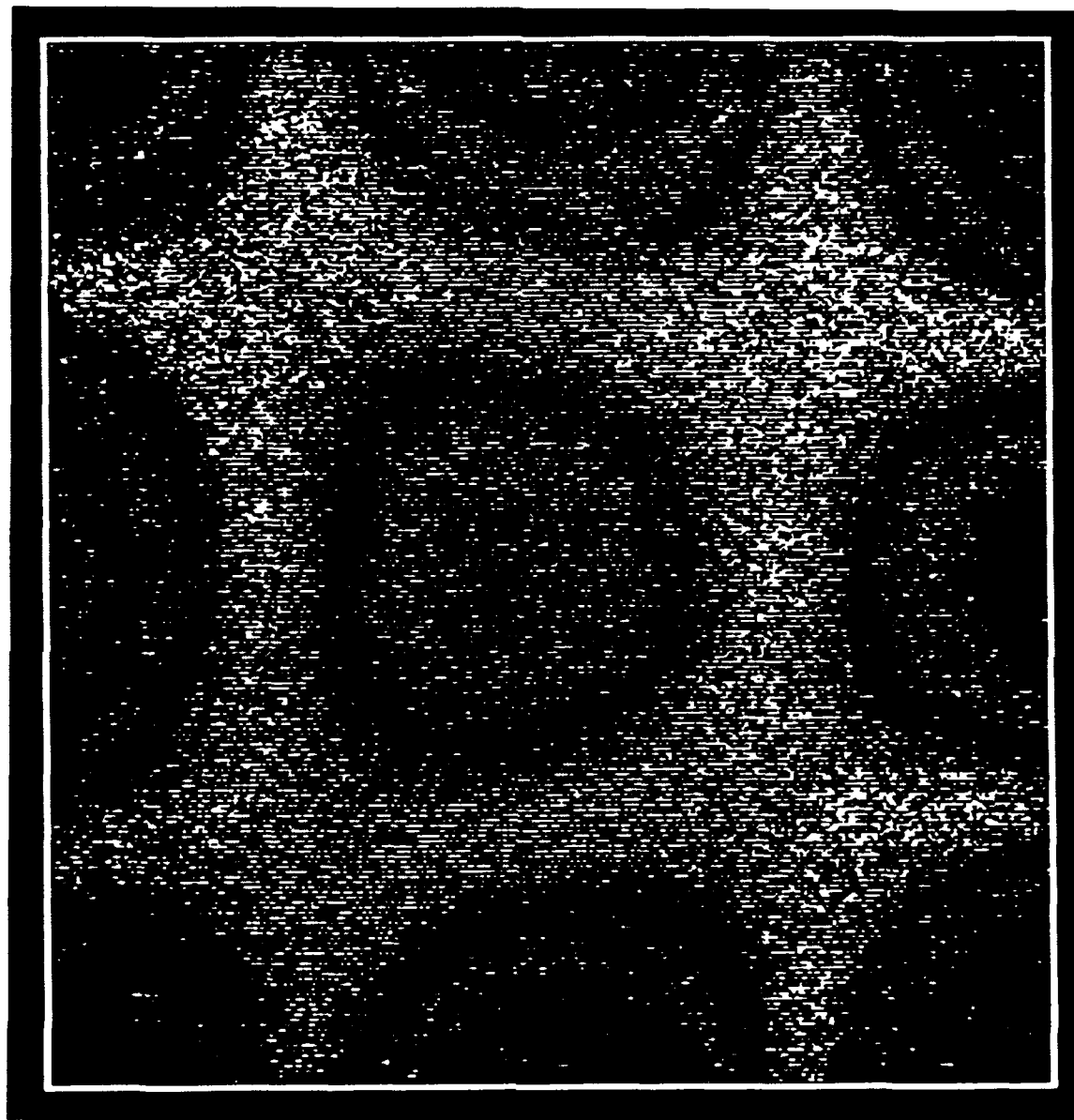
Figure B.15: A 0.25" free aluminum plate underwater: vibrating at 7367 Hz (2,2 mode).
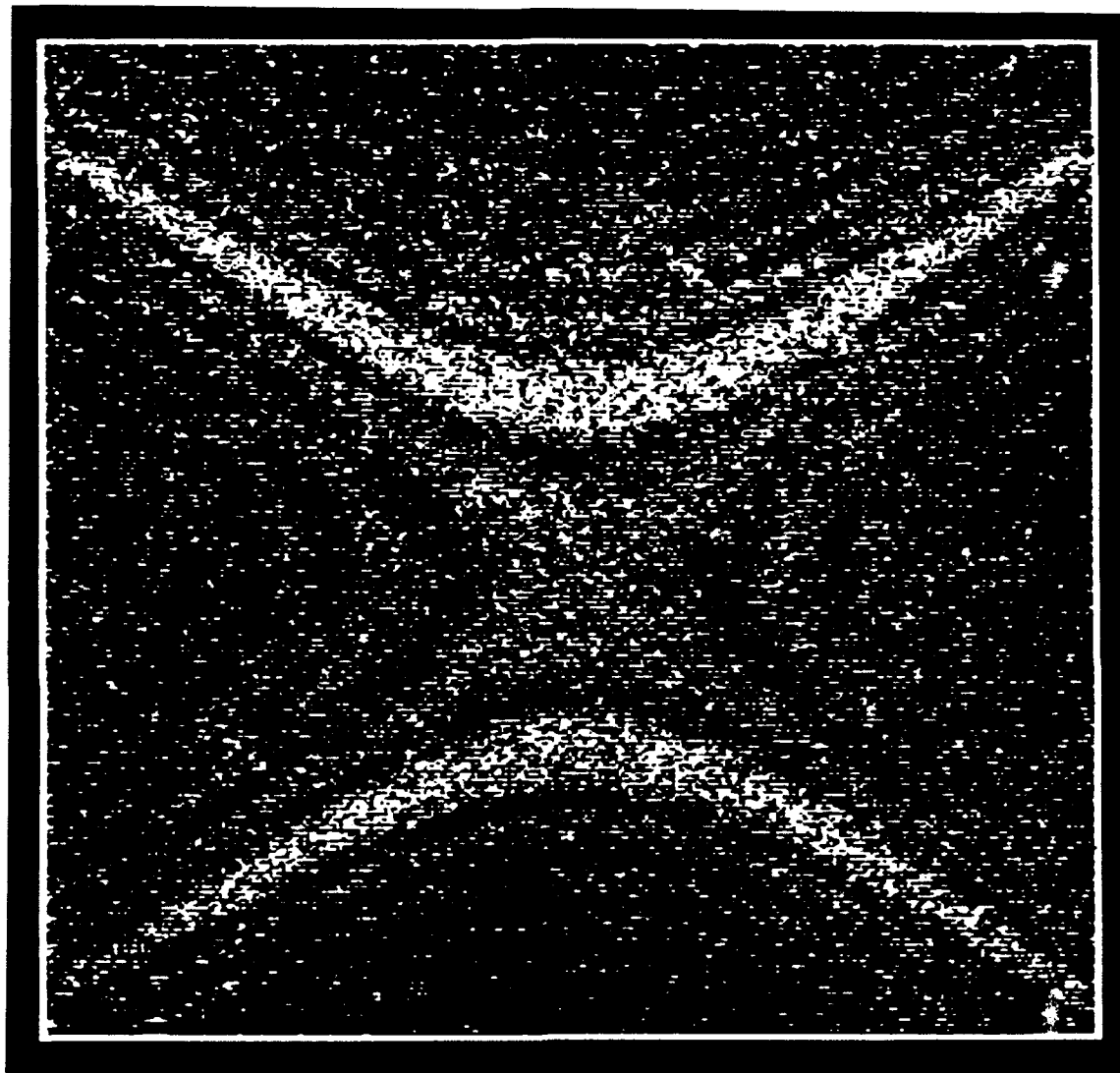
Figure B.16: A 0.25" free composite plate underwater: vibrating at 2171 Hz.
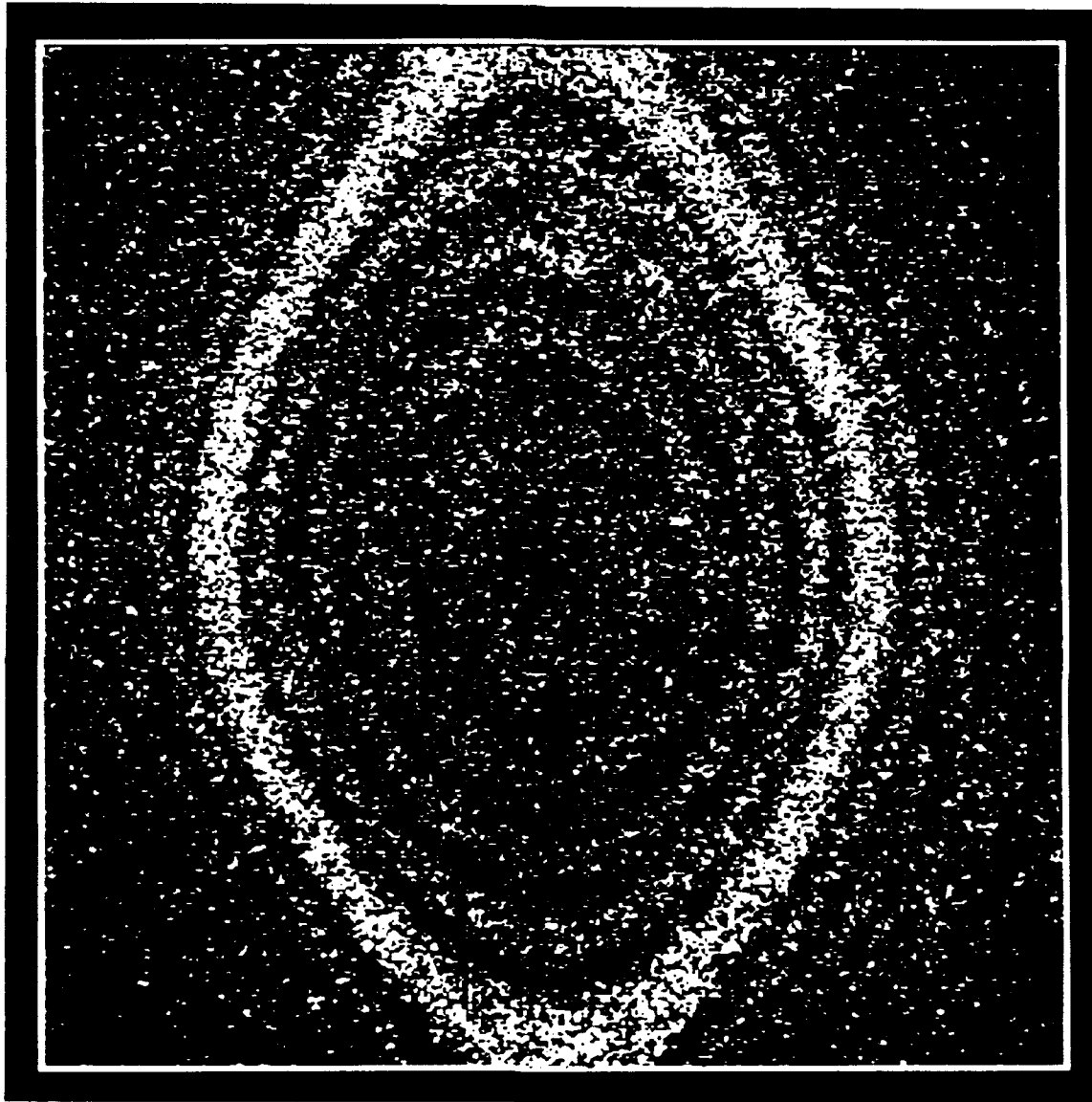
Figure B.17: A 0.25" free composite plate underwater: vibrating at 2695 Hz.
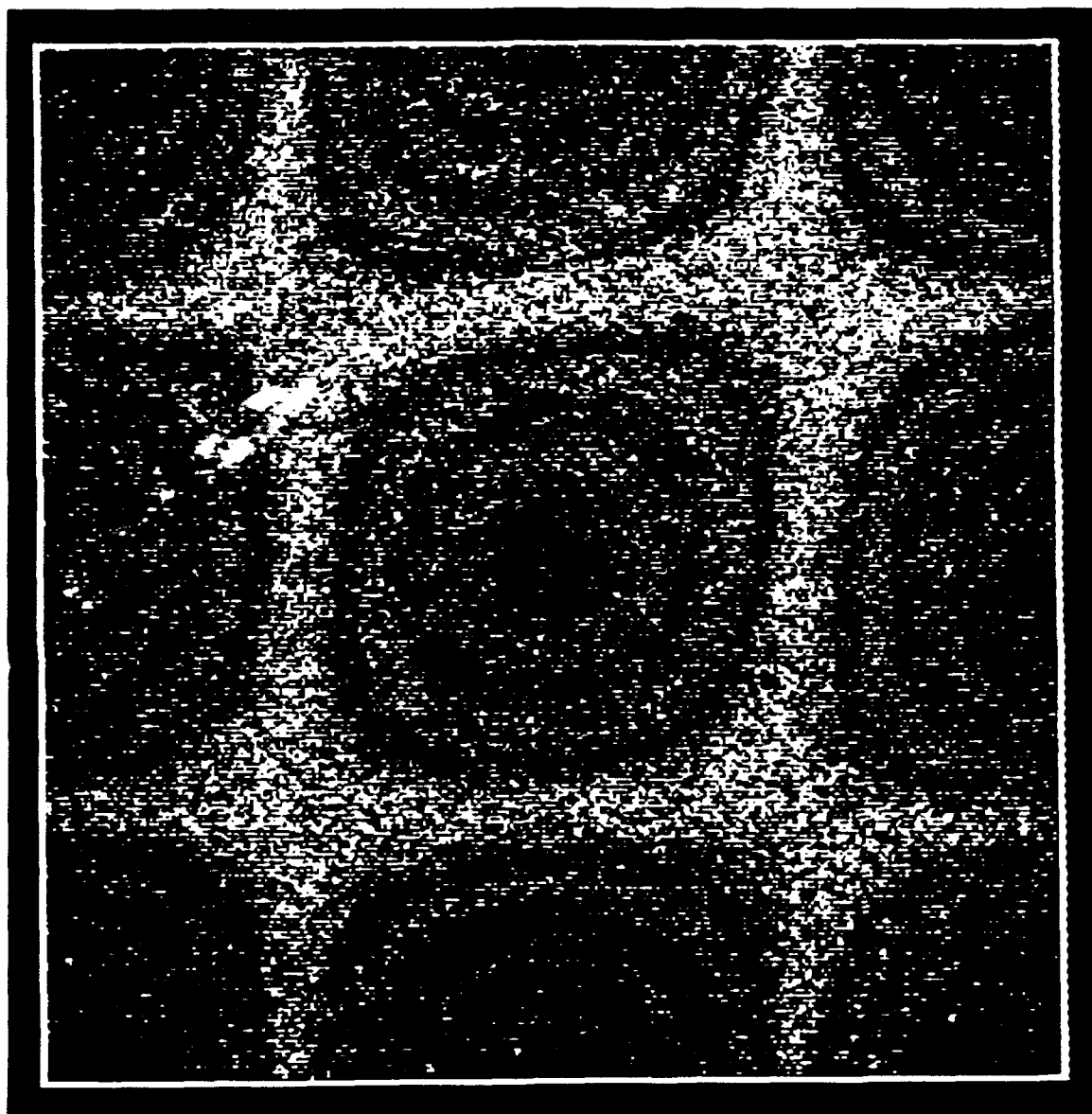
Figure B.18: A 0.25" free composite plate underwater: vibrating at 6525 Hz.
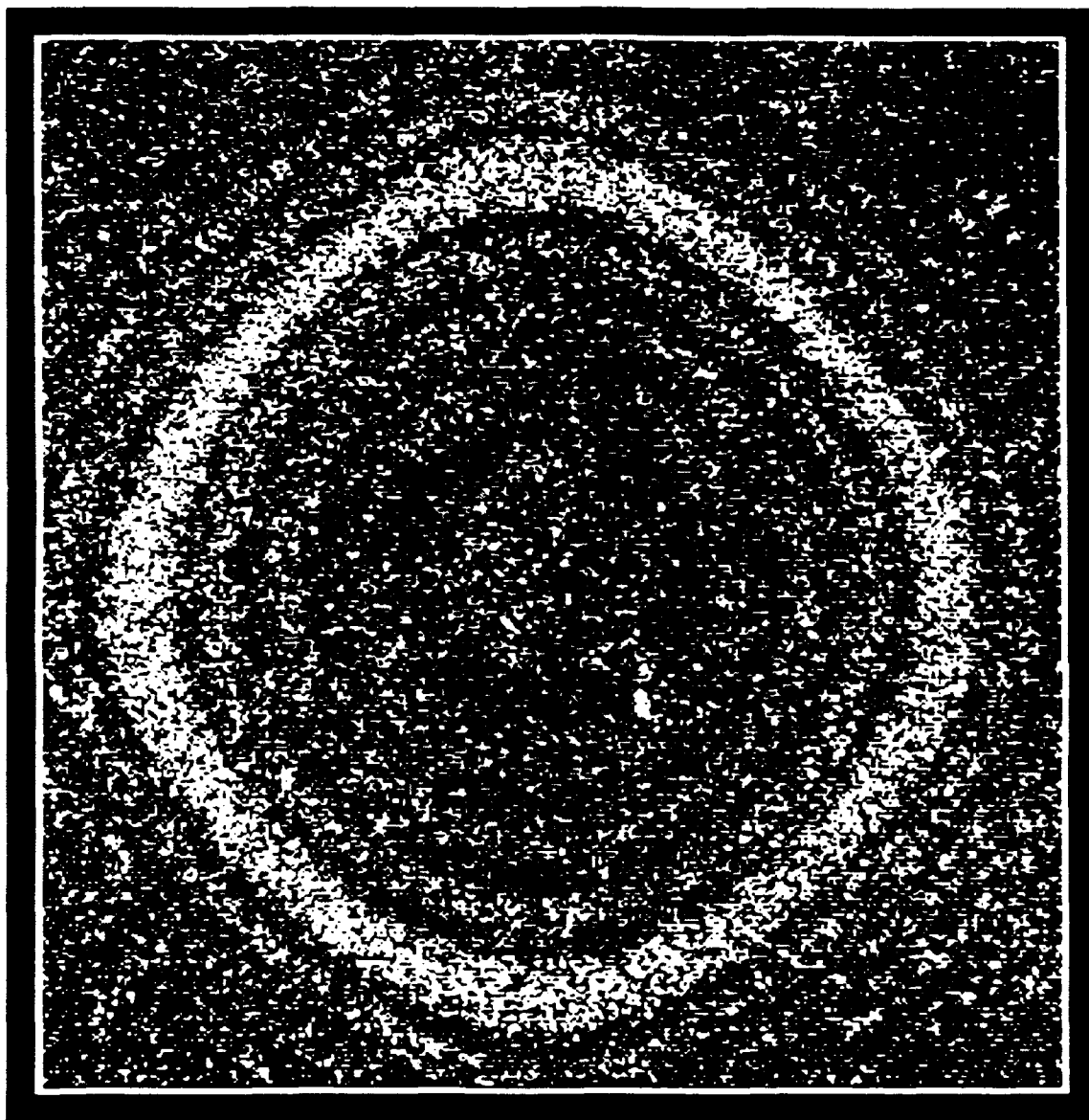
Figure B.19: A 0.08" free aluminum plate underwater: vibrating at 561 Hz (0,2 mode).
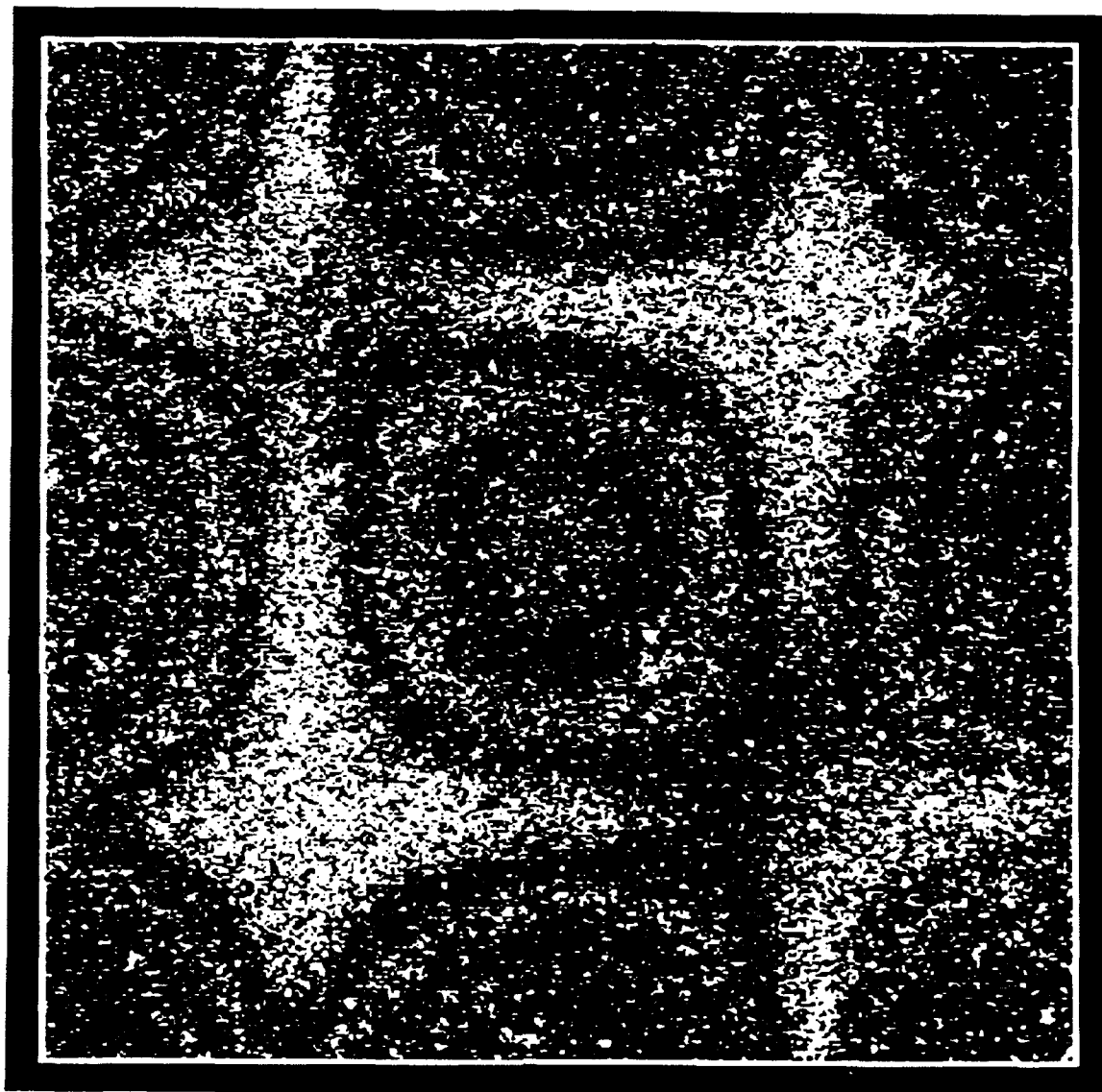
Figure B.20: A 0.08" free aluminum plate underwater: vibrating at 1602 Hz (2,2 mode).
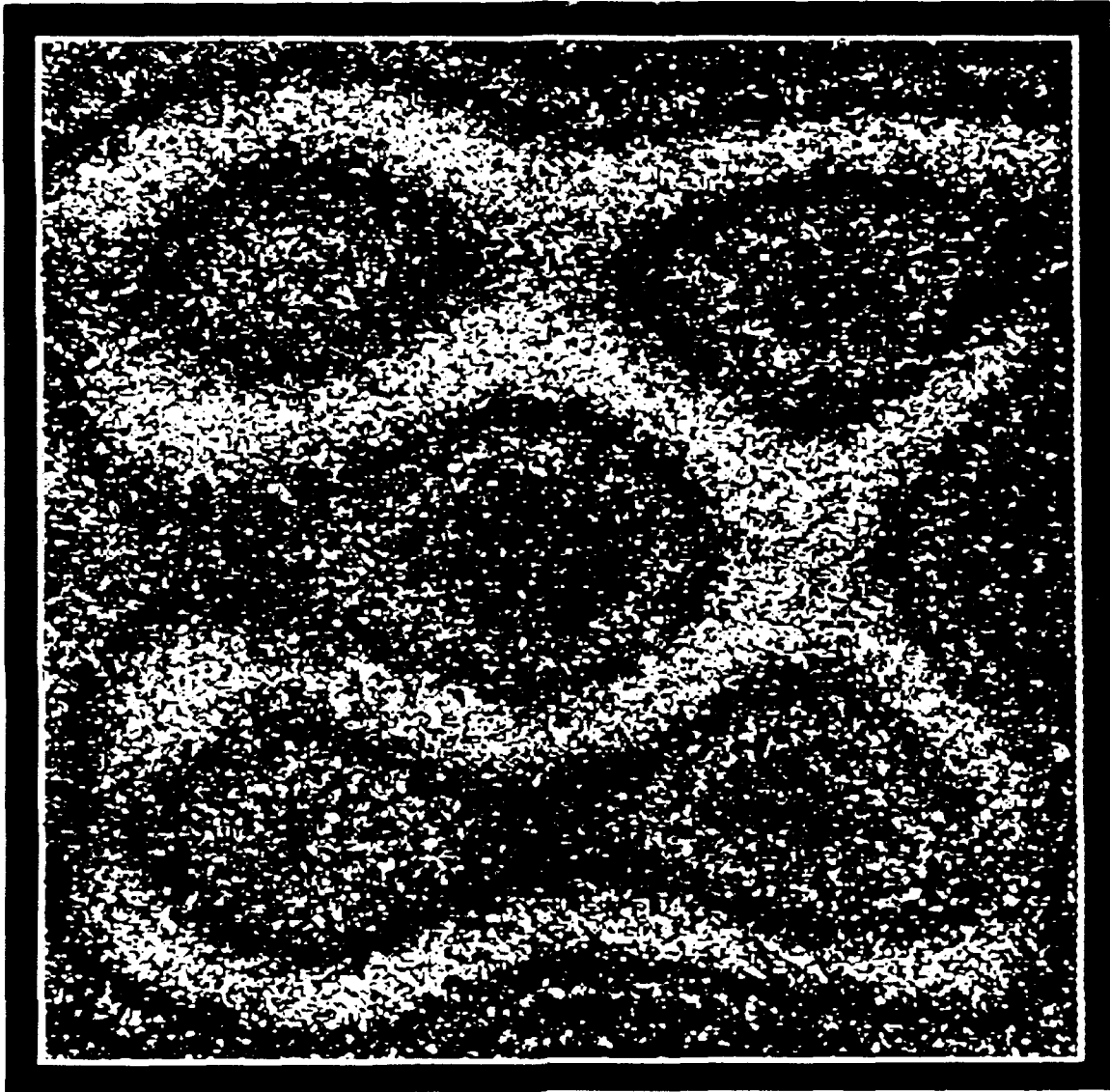
Figure B.21: A 0.08" free aluminum plate underwater: vibrating at 3152 Hz (0,4 mode).
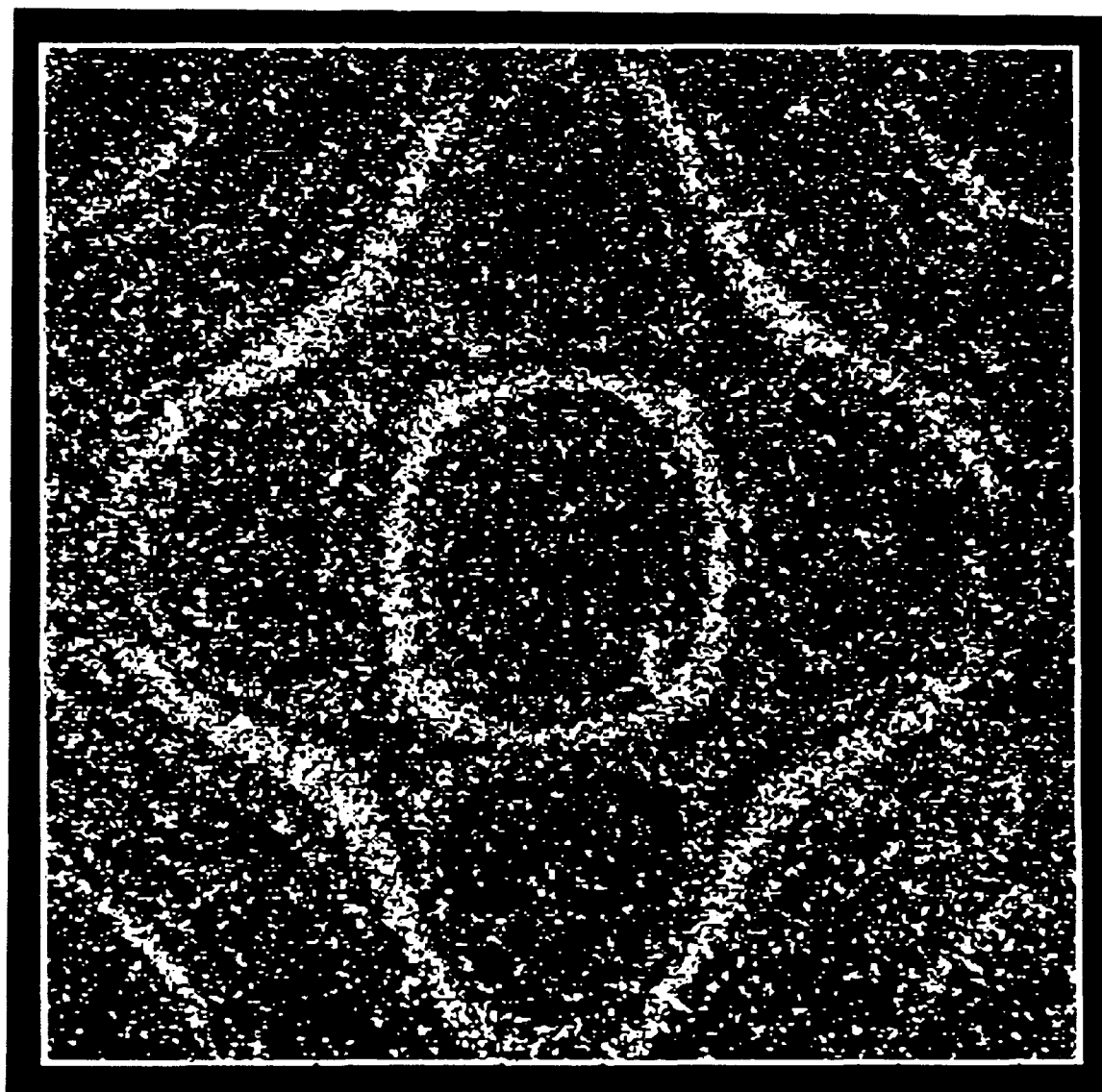
Figure B.22: A 0.08" free aluminum plate underwaters: vibrating at 4436 Hz (2,4 mode).
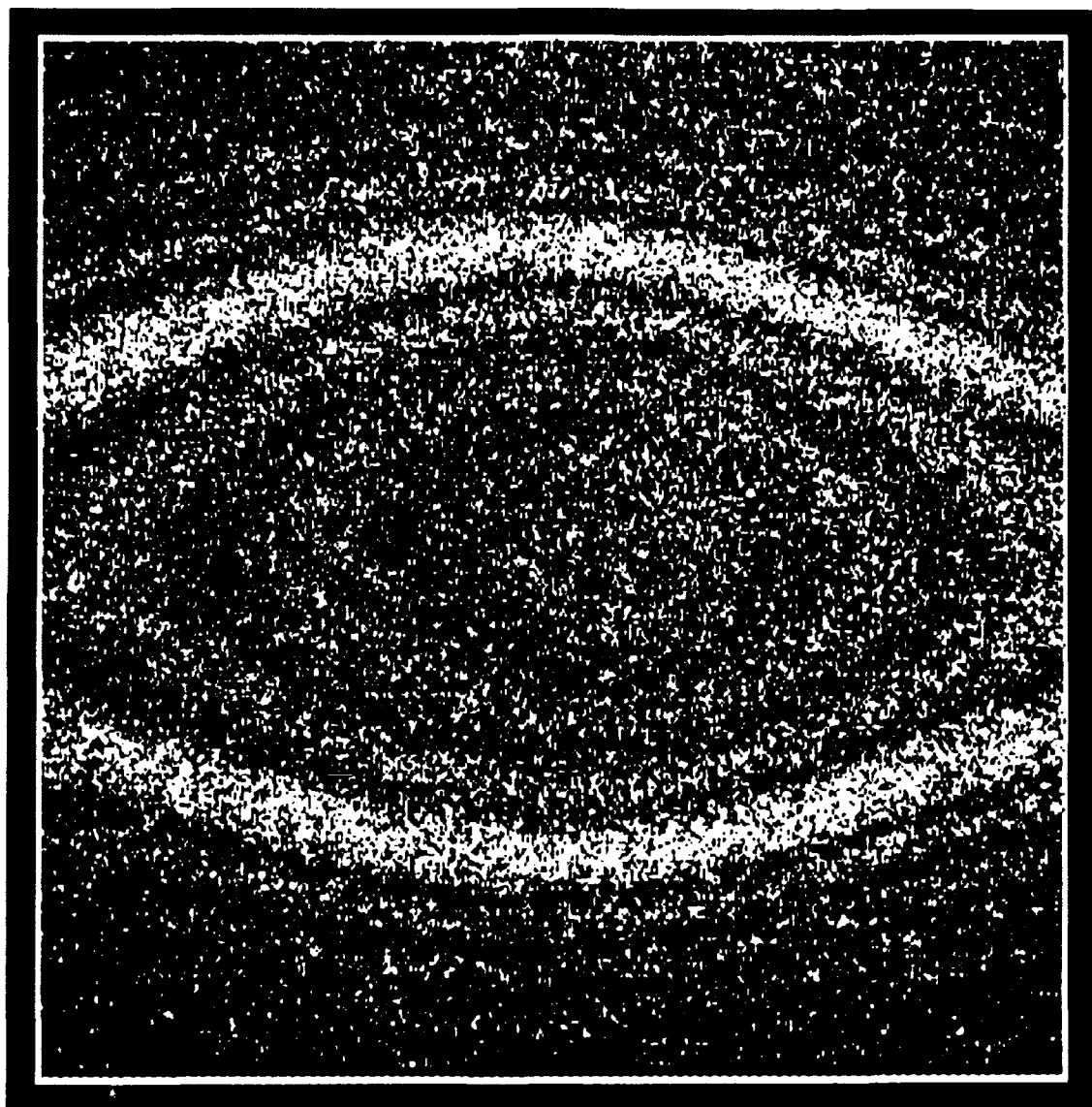
Figure B.23: A 0.08" free composite plate underwater:
vibrating at 525 Hz.
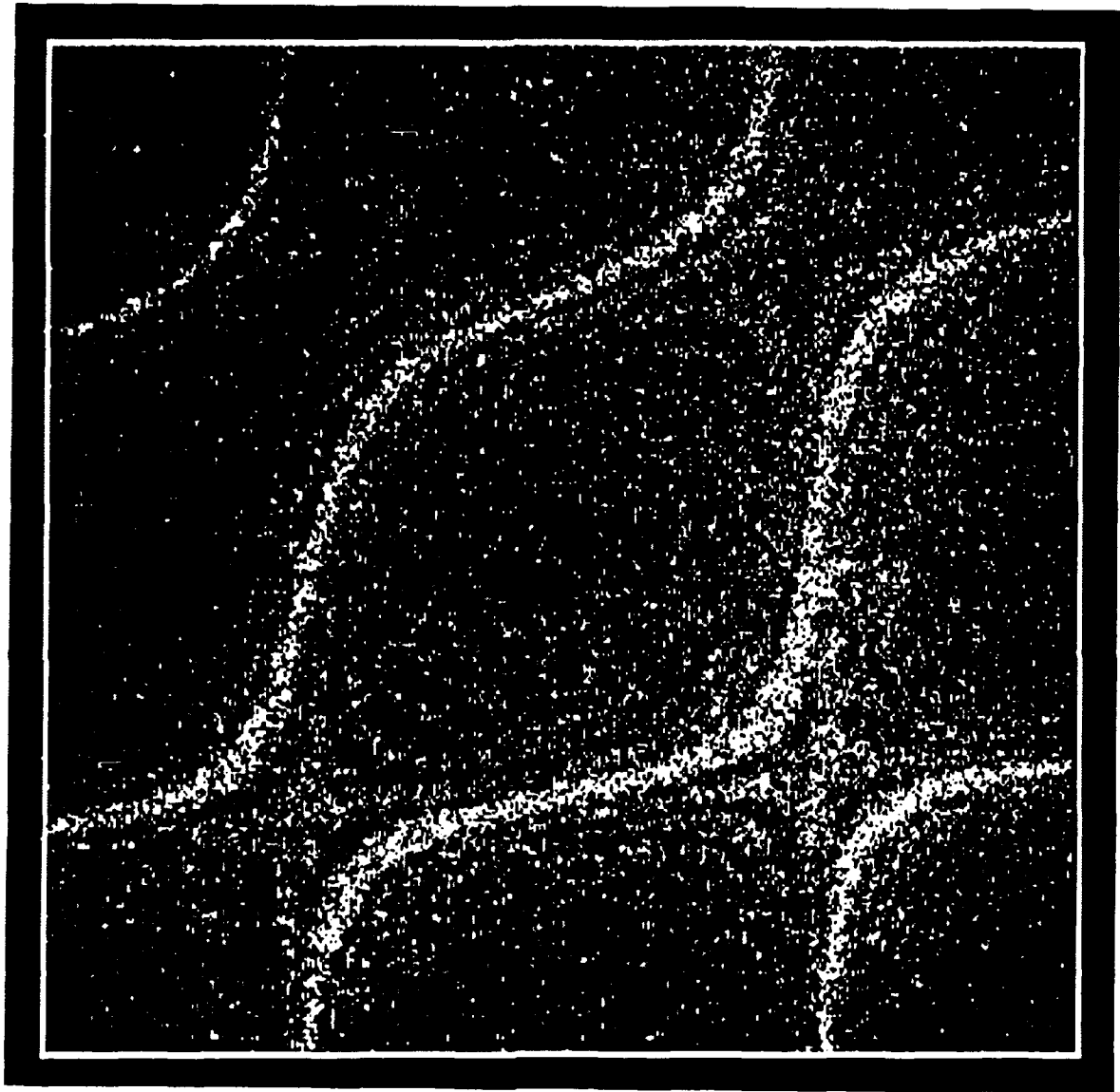
Figure B.24: A 0.08" free composite plate underwater: vibrating at 1380 Hz.
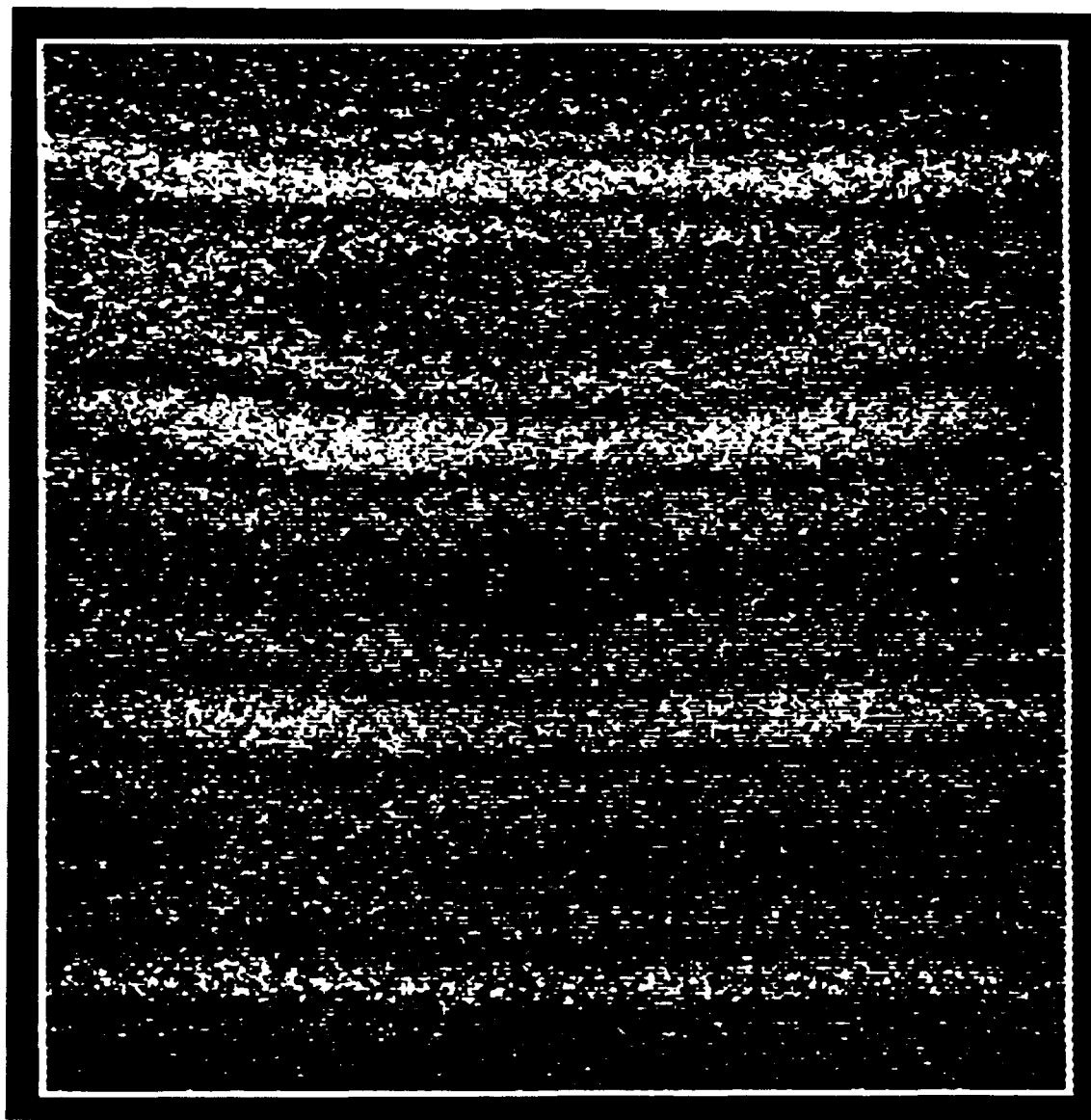
Figure B.25: A 0.08" free composite plate underwater: vibrating at 2423 Hz.
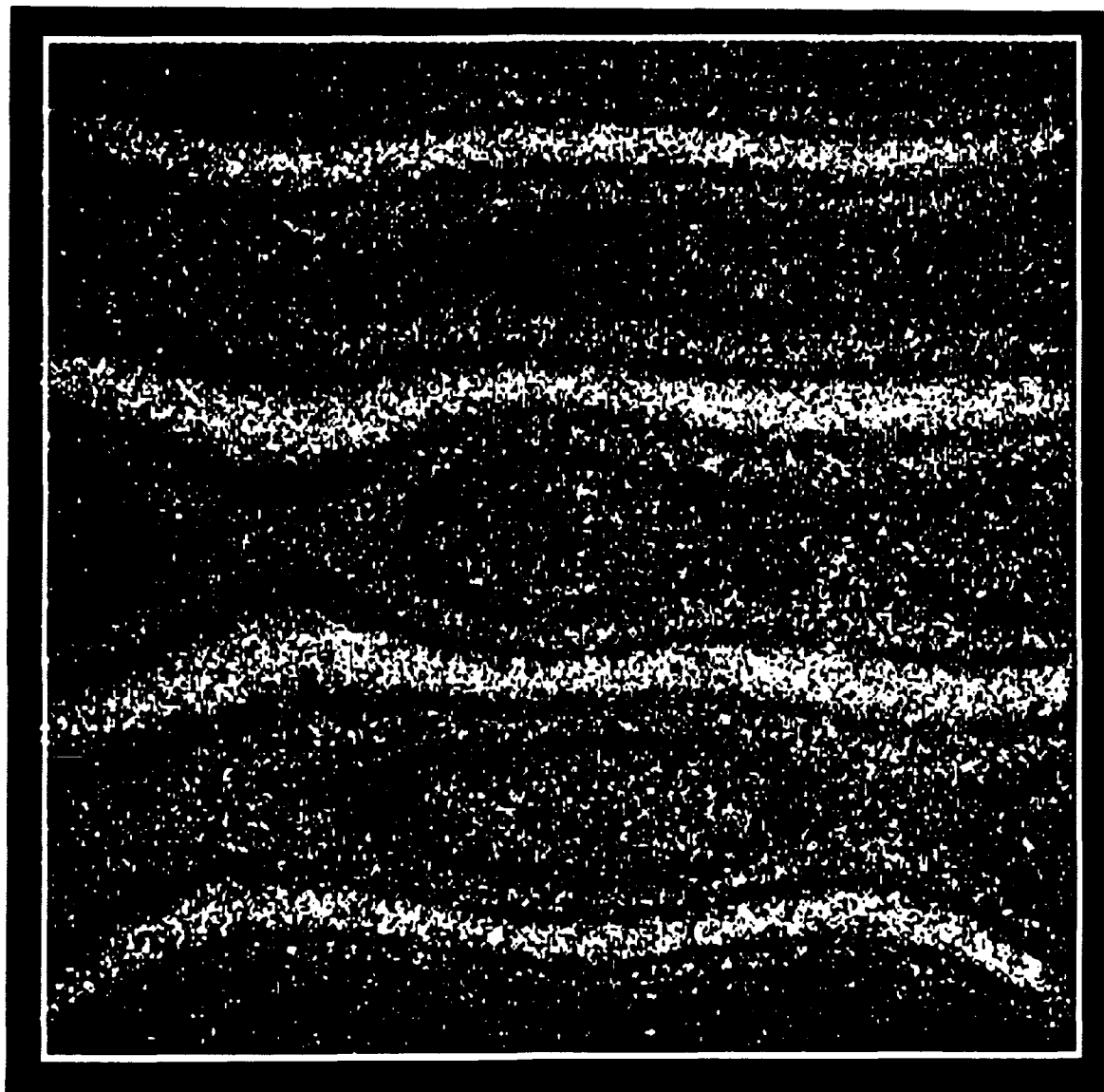
Figure B.26: A 0.08"   free composite plate underwater:
vibrating at 3142 Hz.
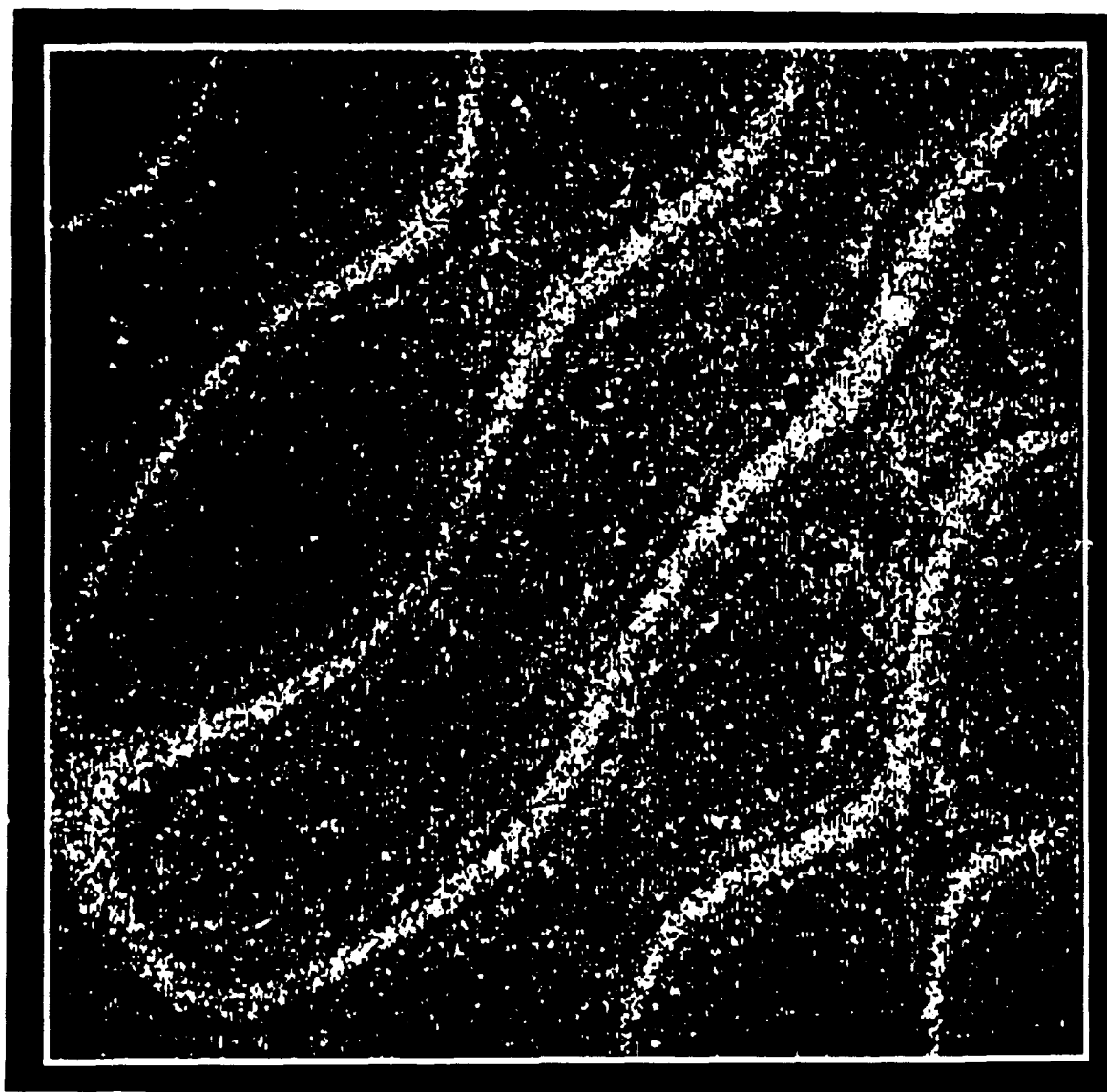
Figure B.27: A 0.08"   free composite plate underwater:
vibrating at 3592 Hz.
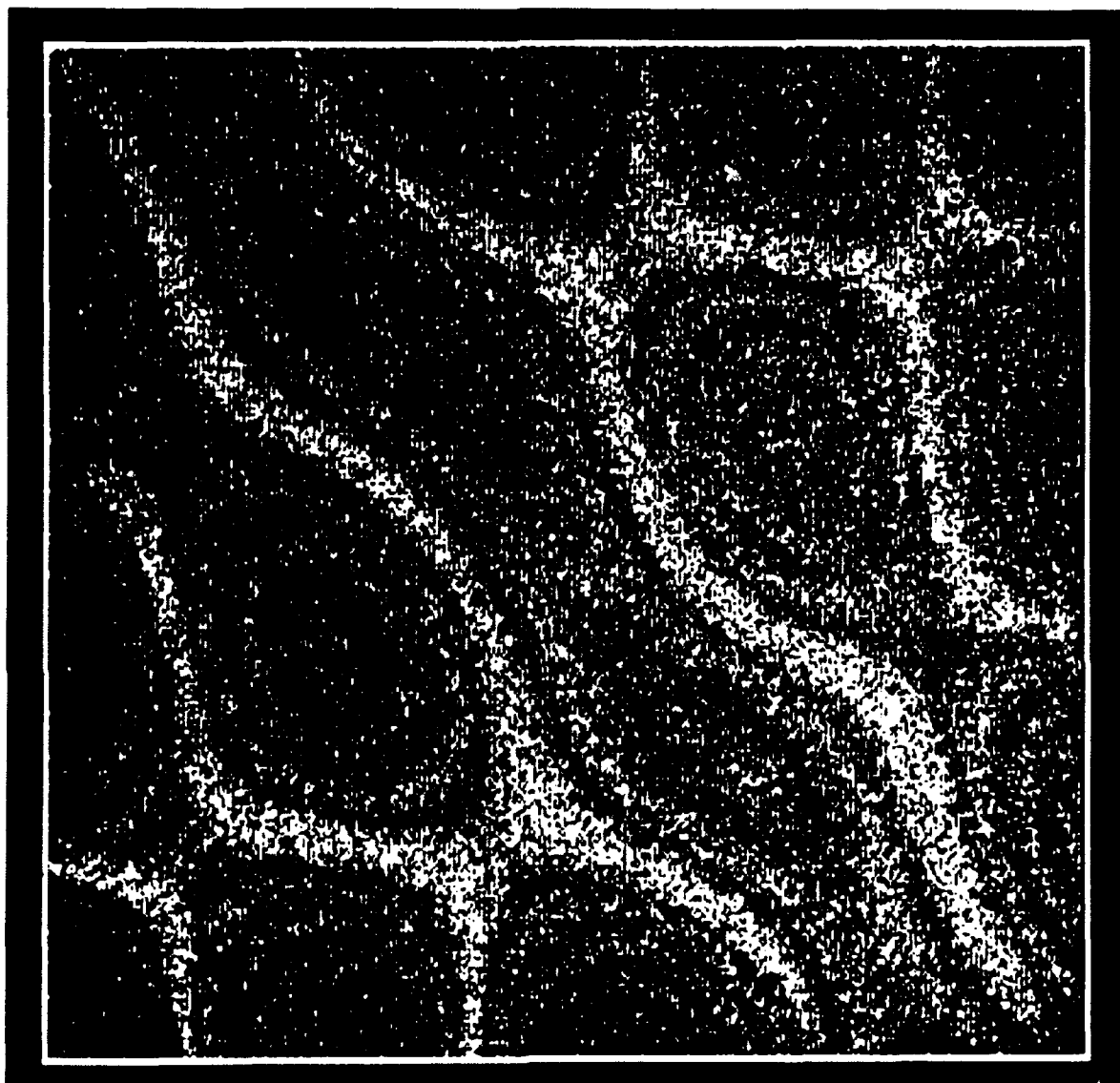
Figure B.28: A 0.08"   free composite plate underwater:
vibrating at 3788 Hz.
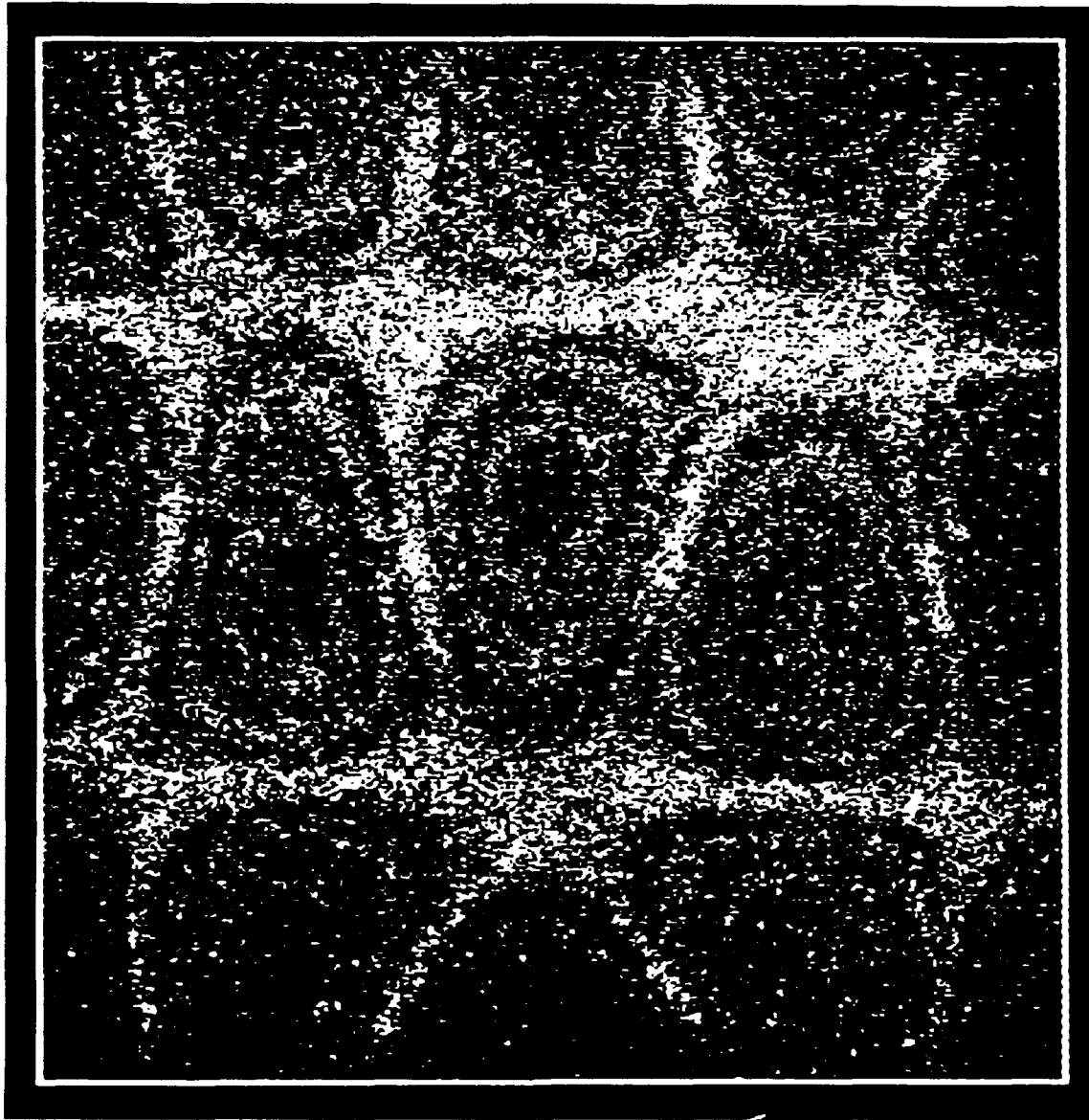
Figure B.29: A 0.08" free composite plate underwater: vibrating at 4250 Hz.
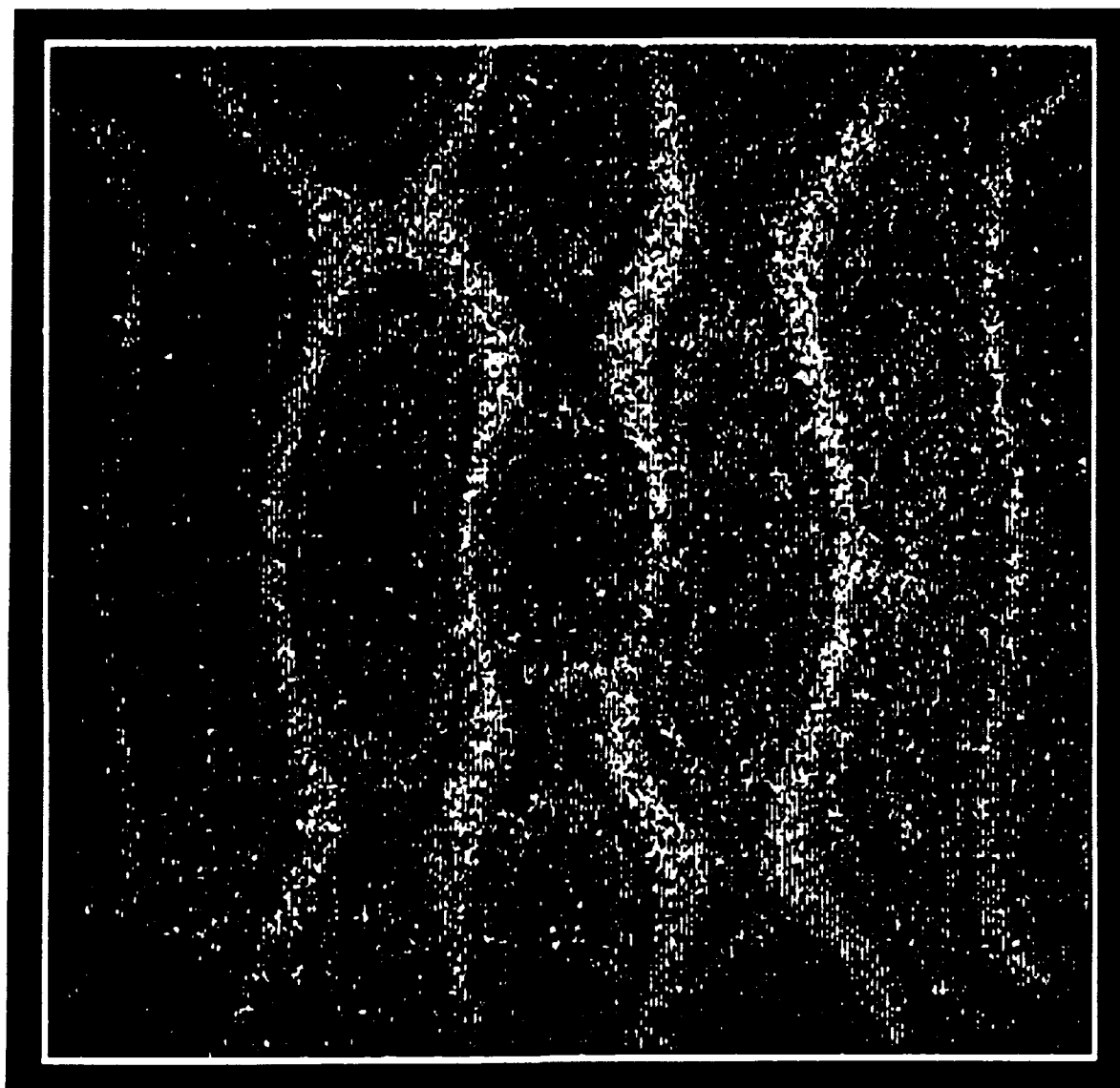
Figure B.30: A 0.08" free composite plate underwater: vibrating at 6398 Hz.
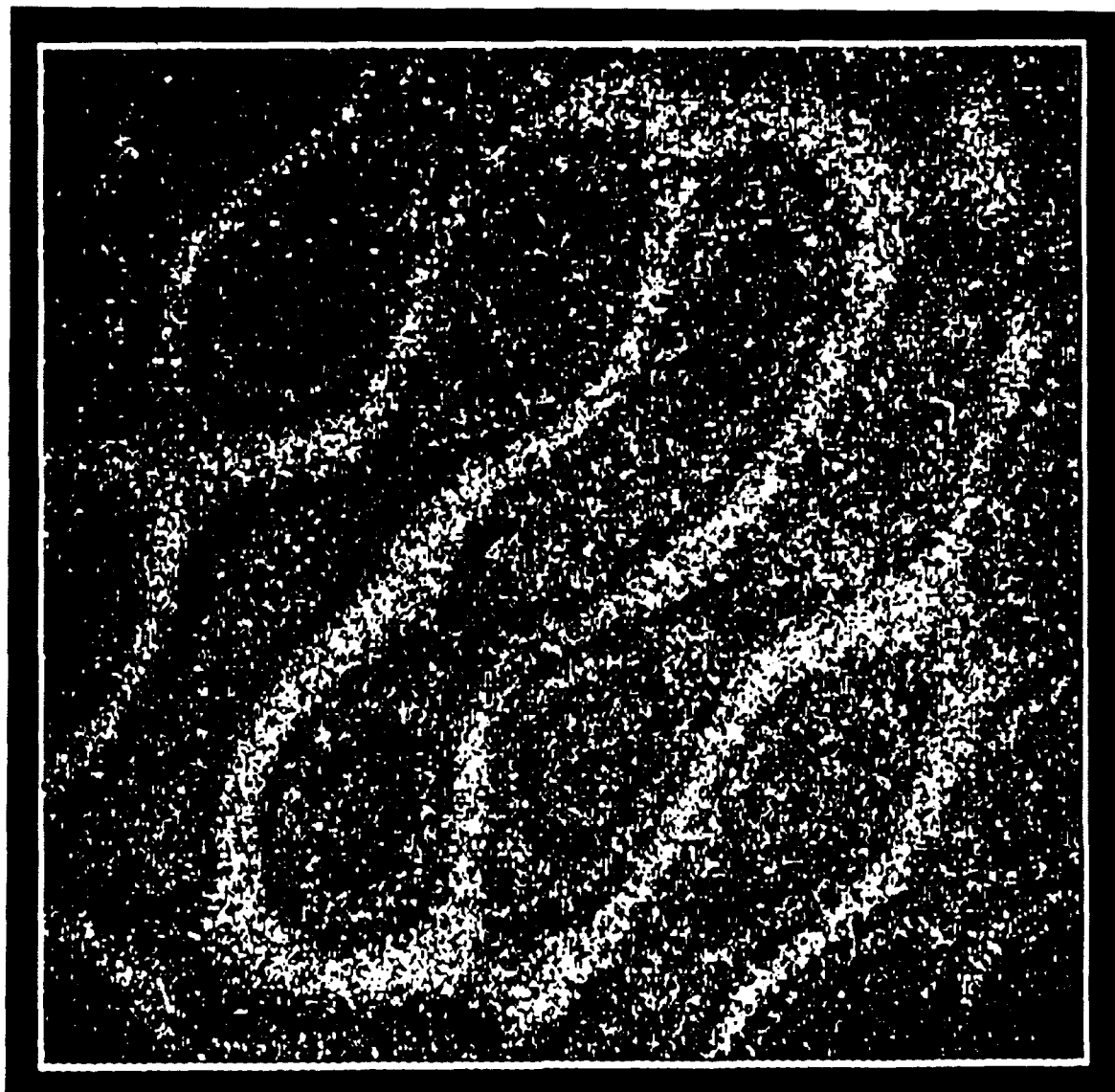
Figure B.31: A 0.08" free composite plate underwater: vibrating at 6831 Hz.
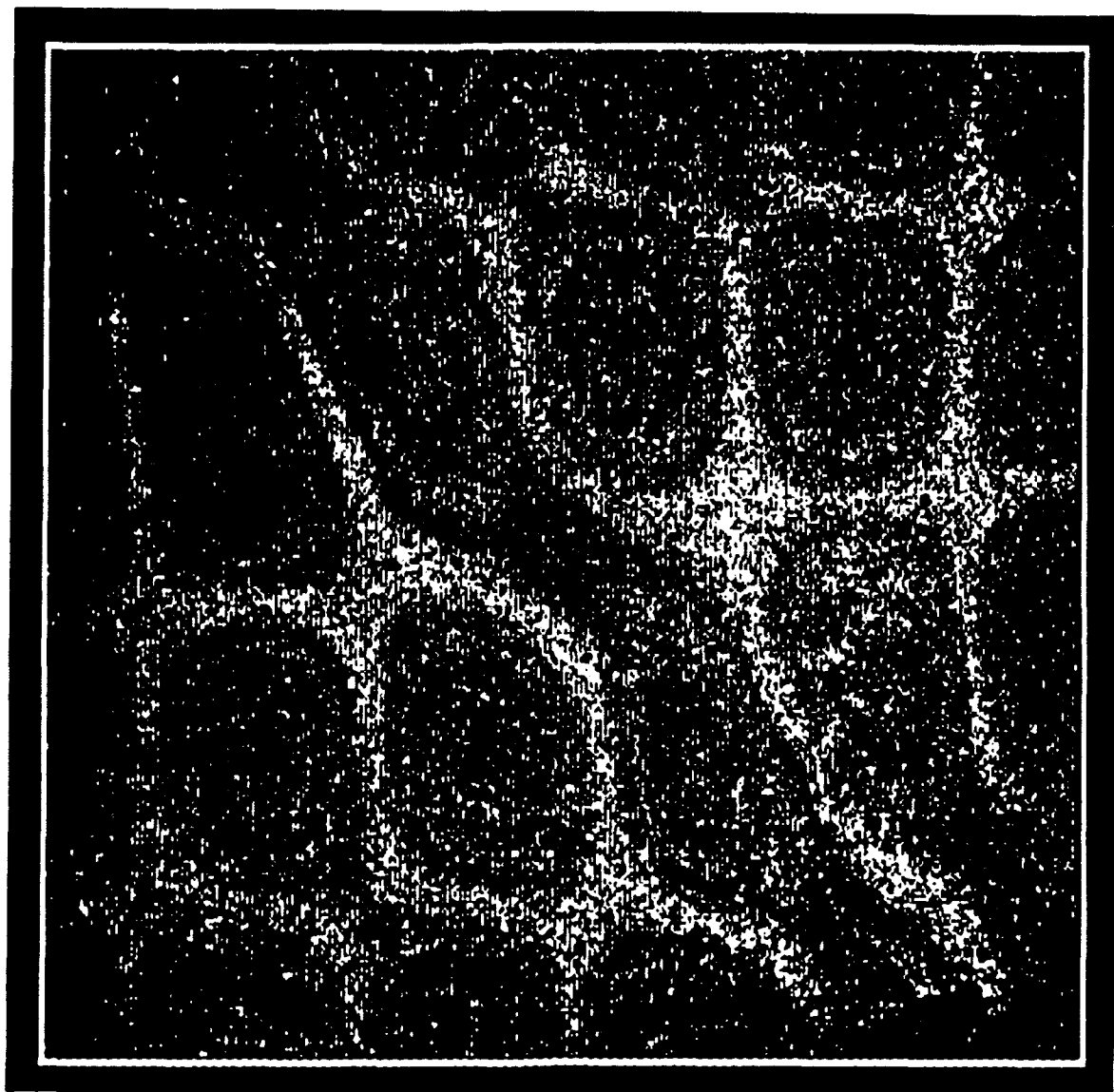
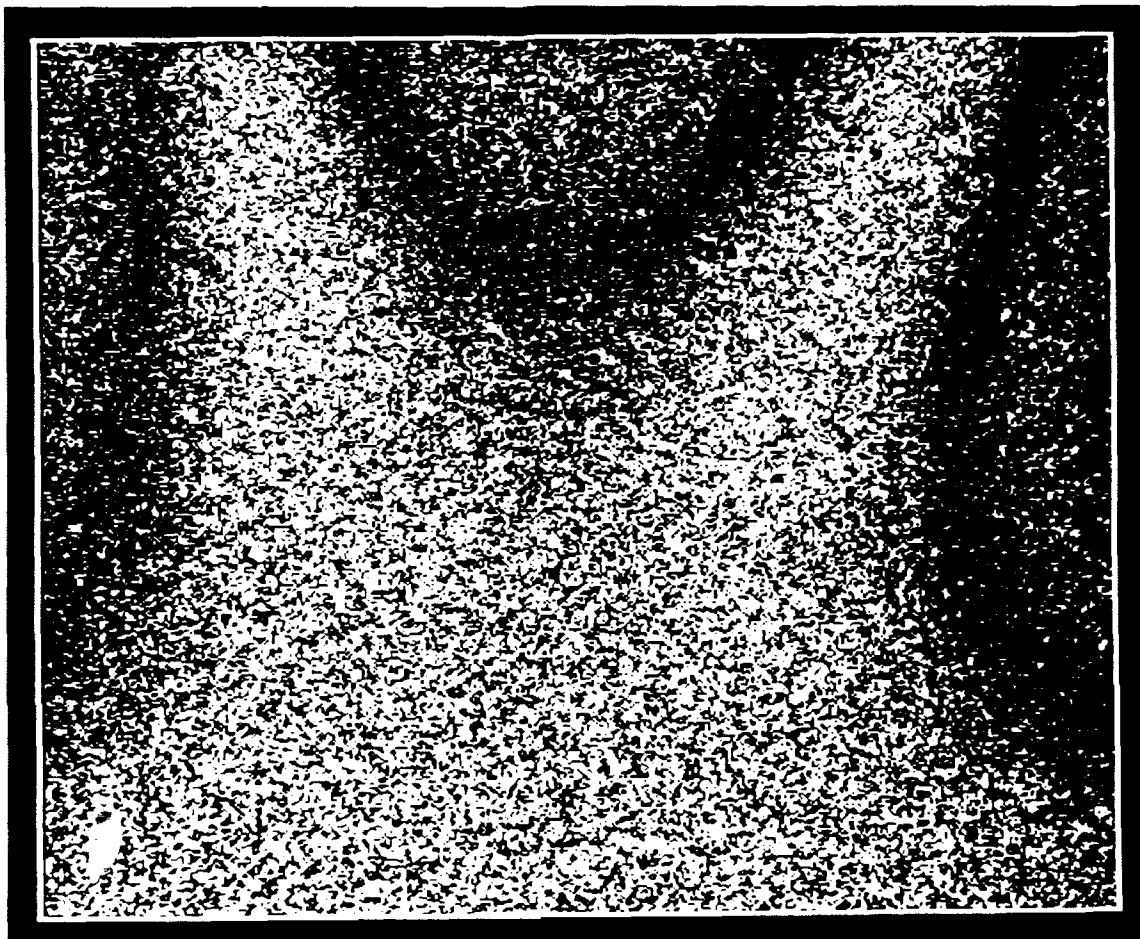Figure B.32: A 0.08" free composite plate underwater: vibrating at 7258 Hz.
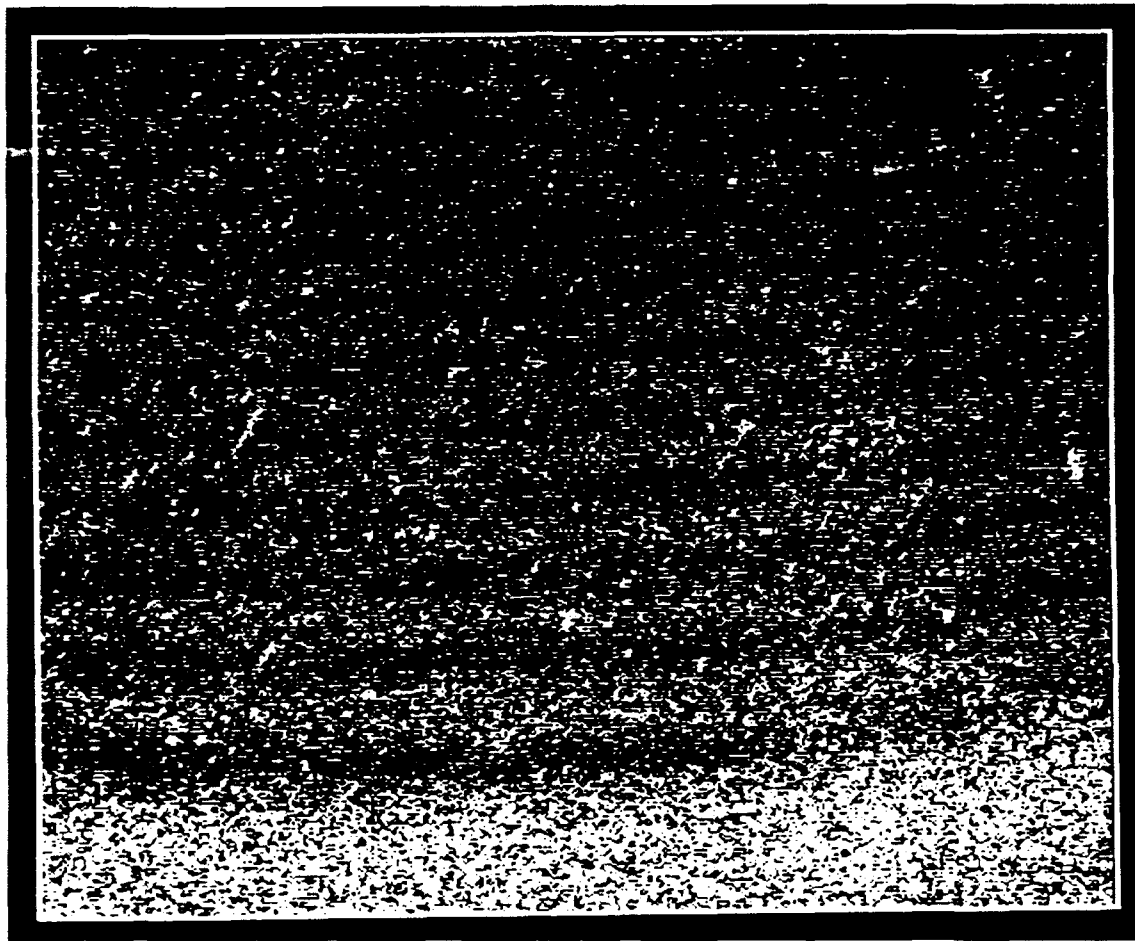
Figure B.33: A 0.25" cantilever aluminum plate in air: vibrating at 665 Hz (0,0 mode).
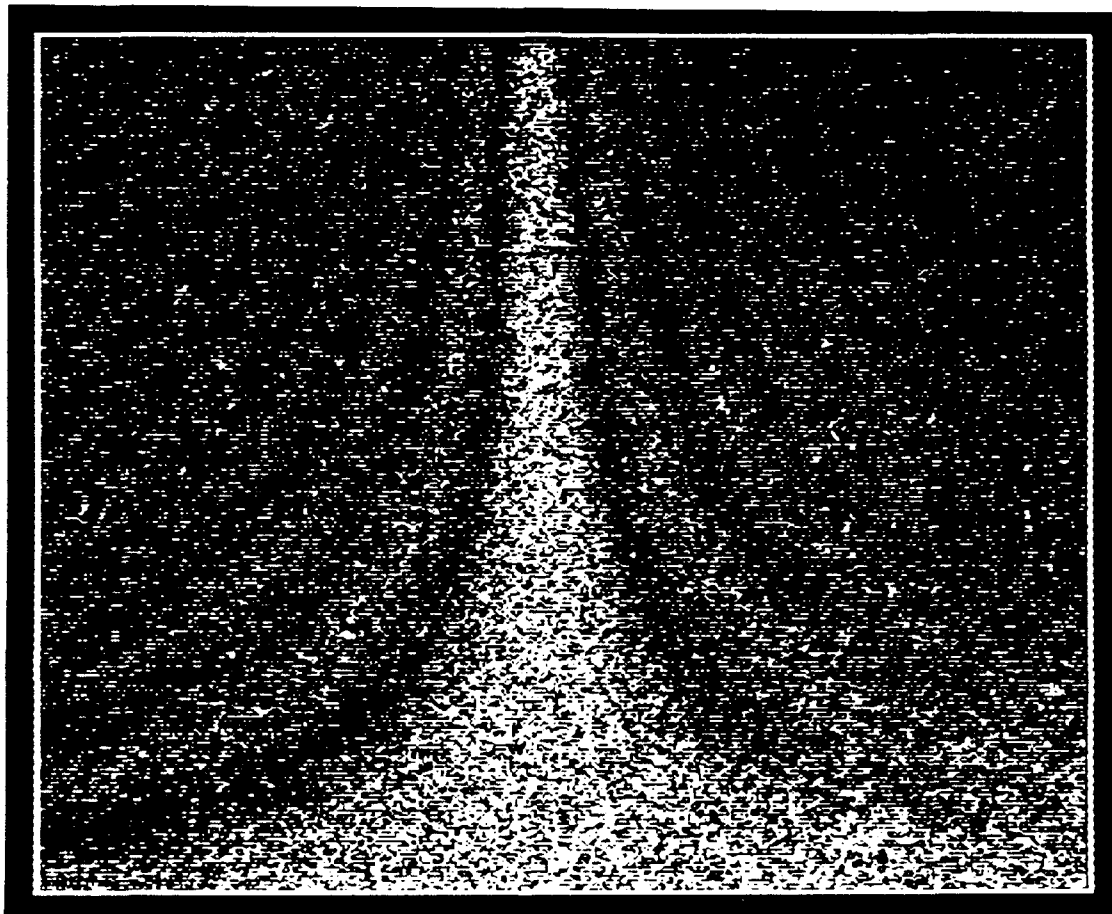
Figure B.34: A 0.25" cantilever aluminum plate in air: vibrating at 1518 Hz (1,0 mode).
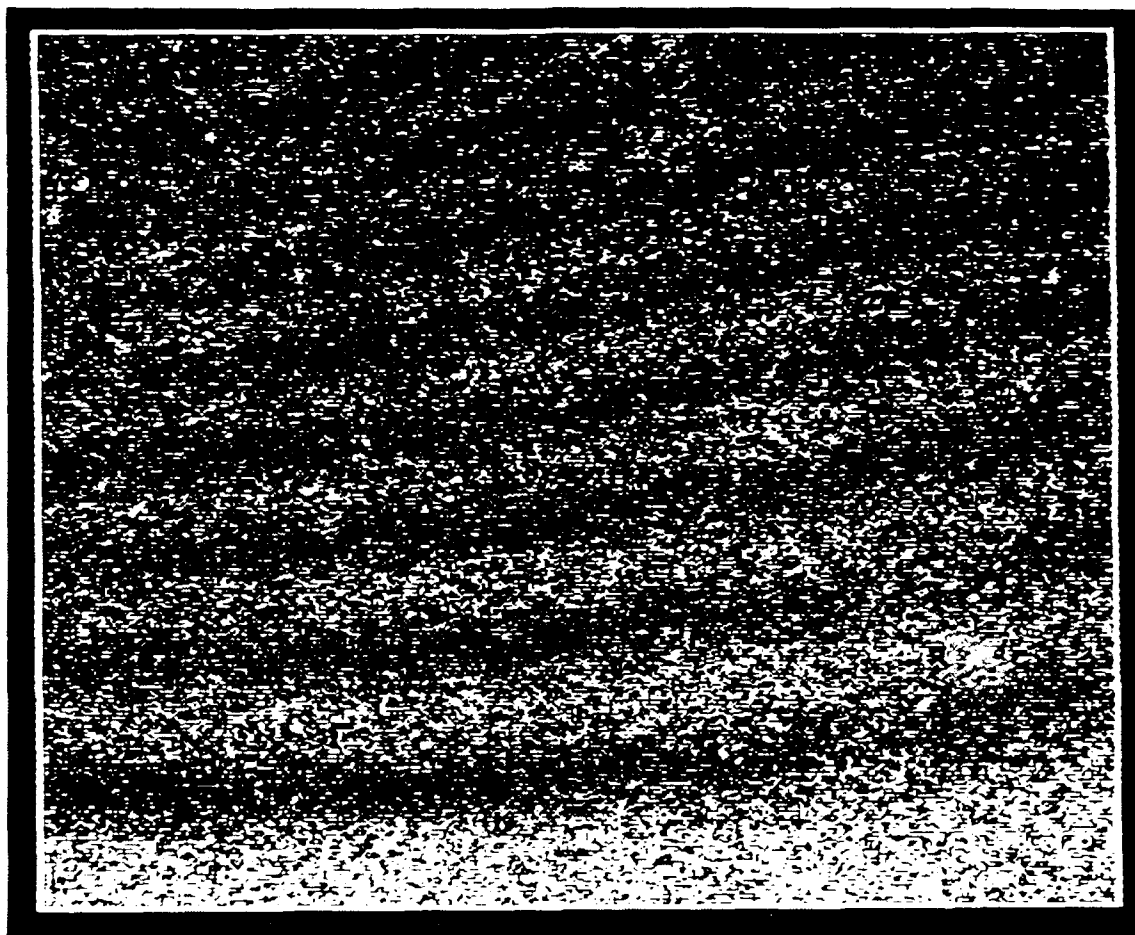
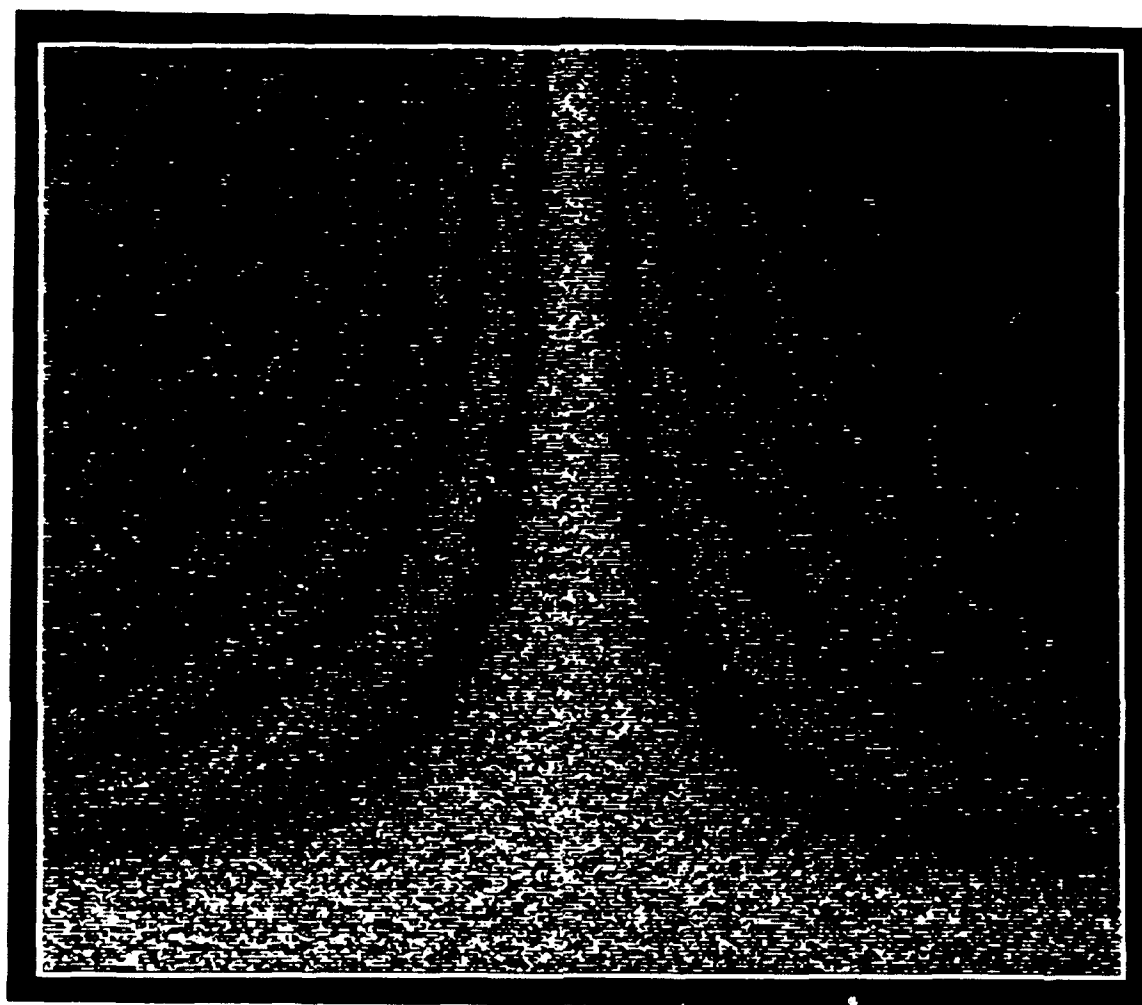Figure B.35: **A 0.25"** cantilever composite plate in air: vibrating at 601 Hz.
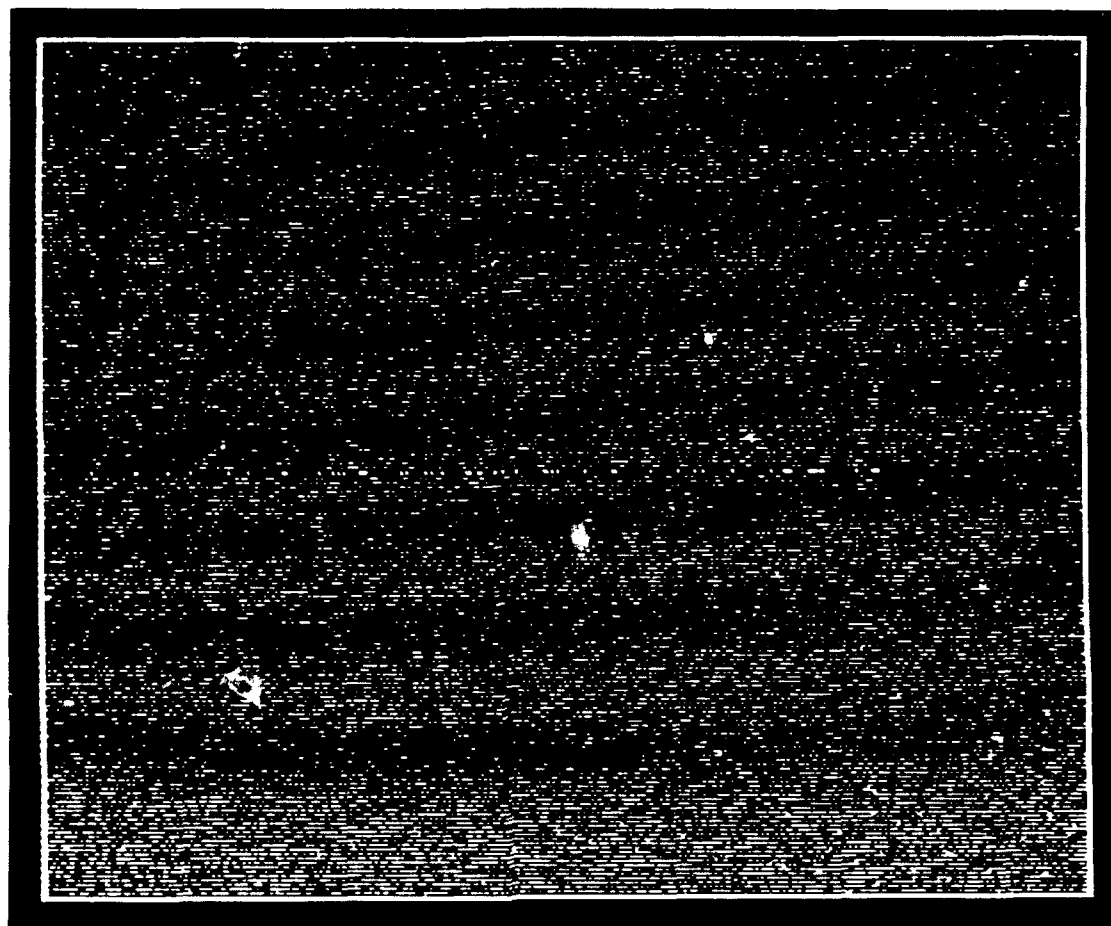
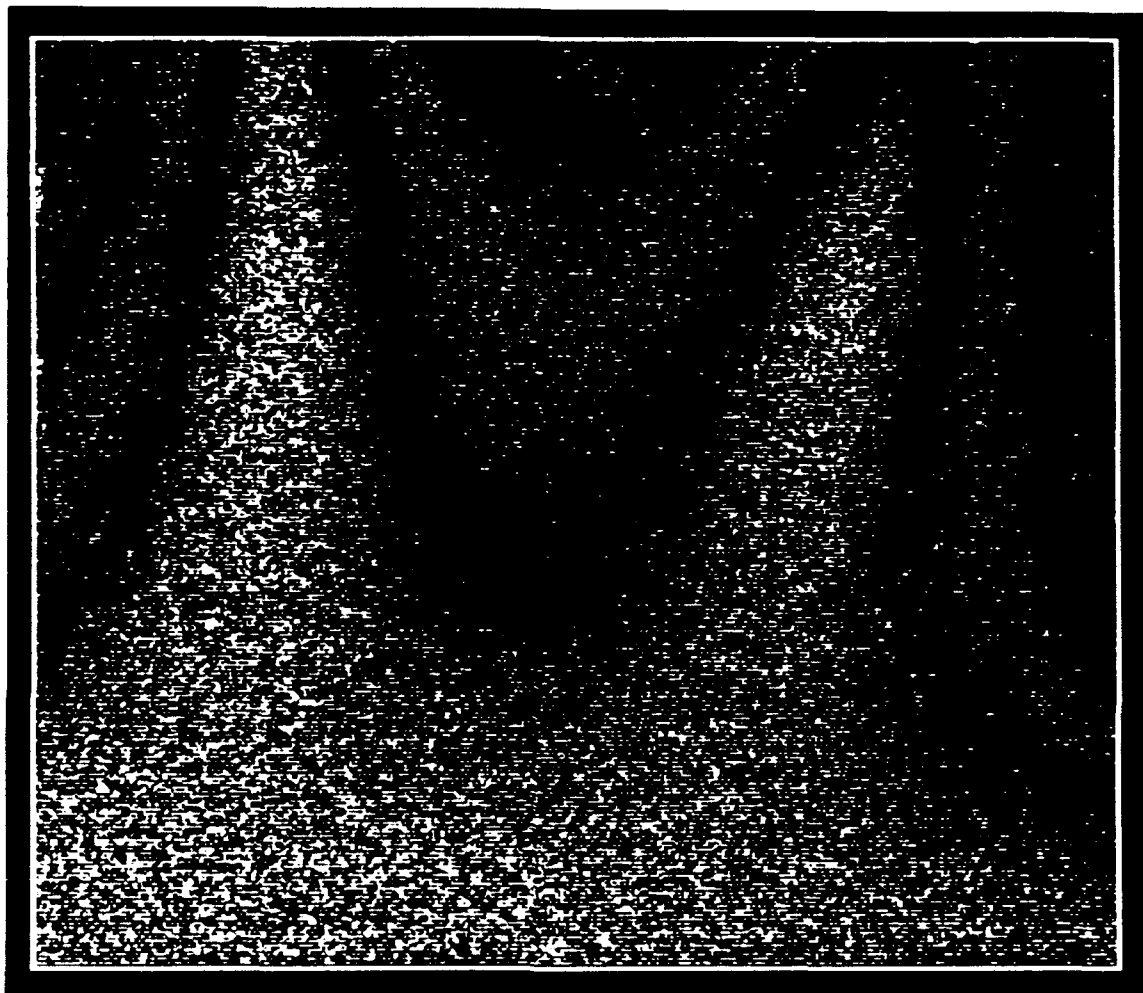Figure B.36: A 0.25" cantilever composite plate in air: vibrating at 789 Hz (0,0 mode).
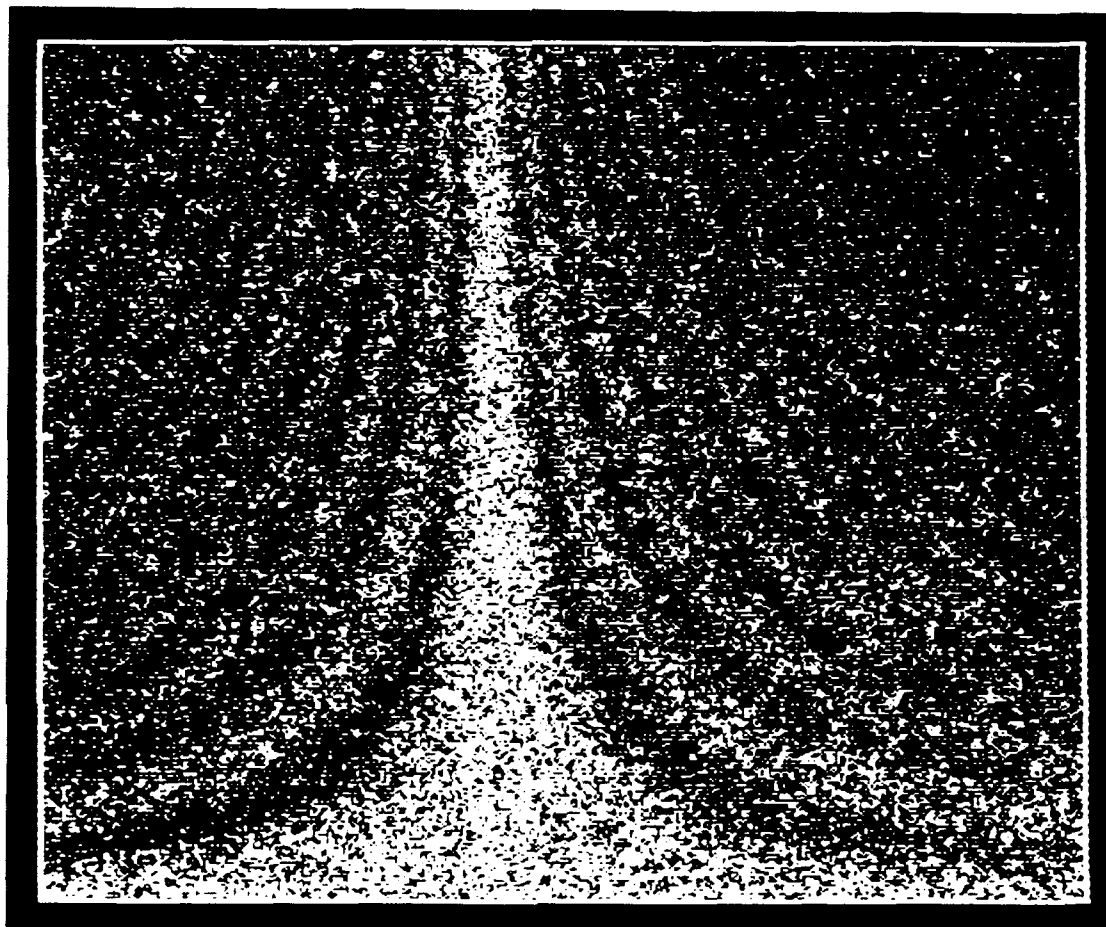
Figure B.37: A 0.25" cantilever composite plate in air: vibrating at 1565 Hz (1,0 mode).
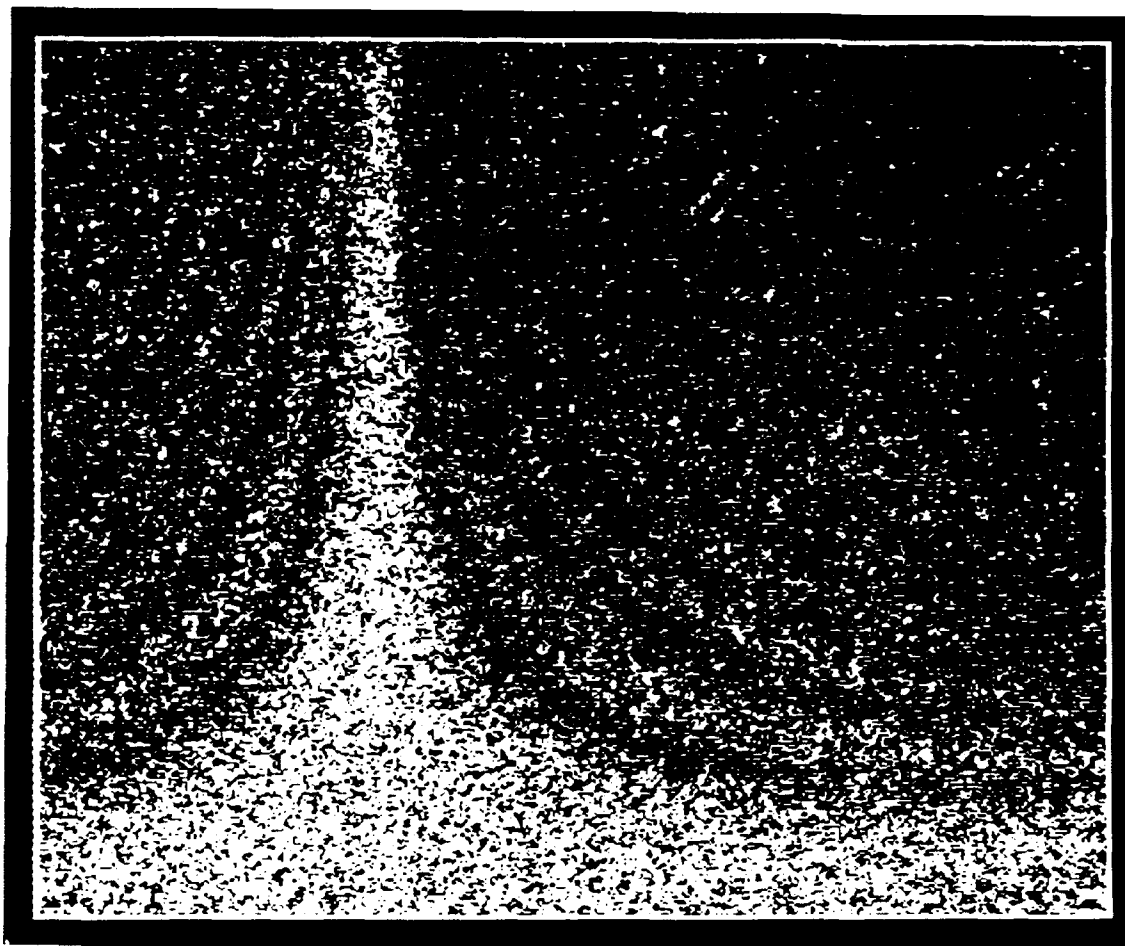
Figure B.38: A 0.08" cantilever aluminum plate in air: vibrating at 402 Hz.
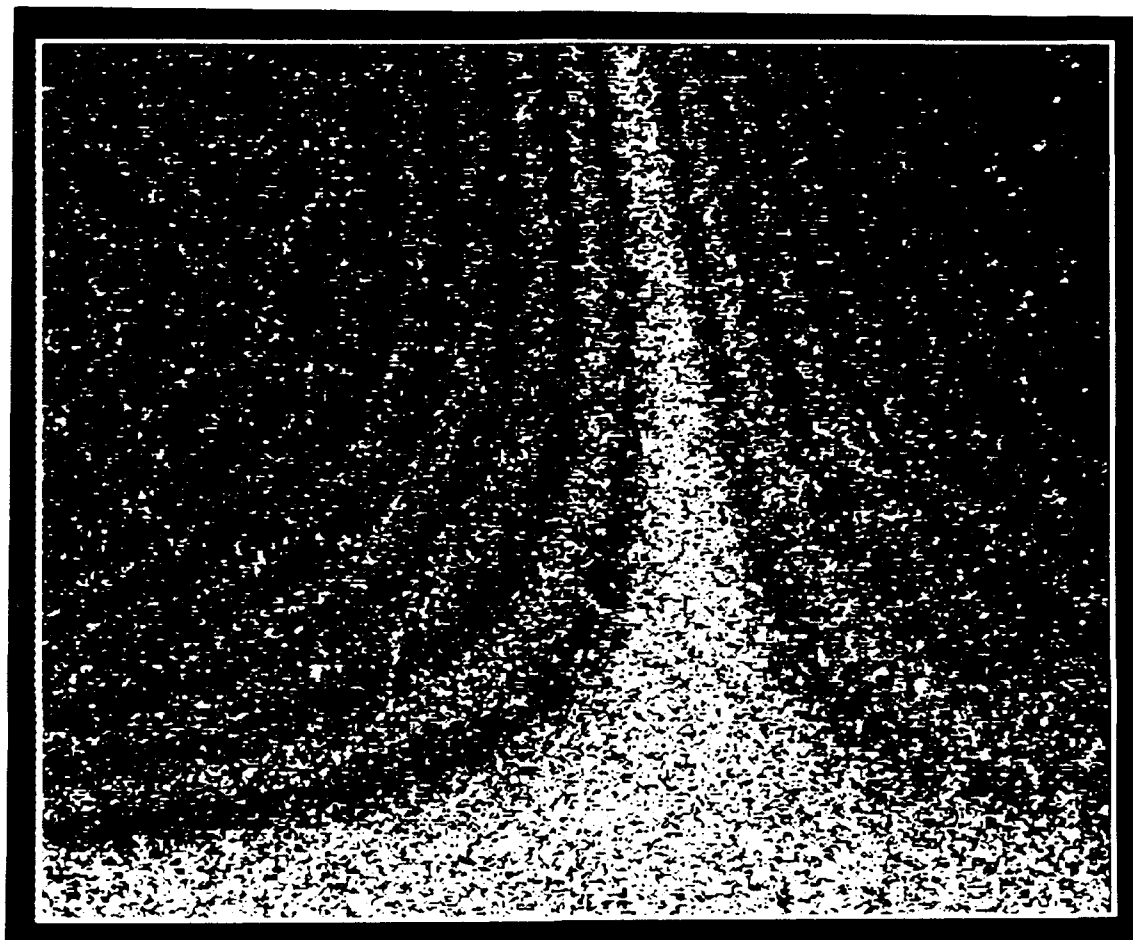
Figure B.39: A 0.08" cantilever aluminum plate in air: vibrating at 595 Hz (1,0 mode).
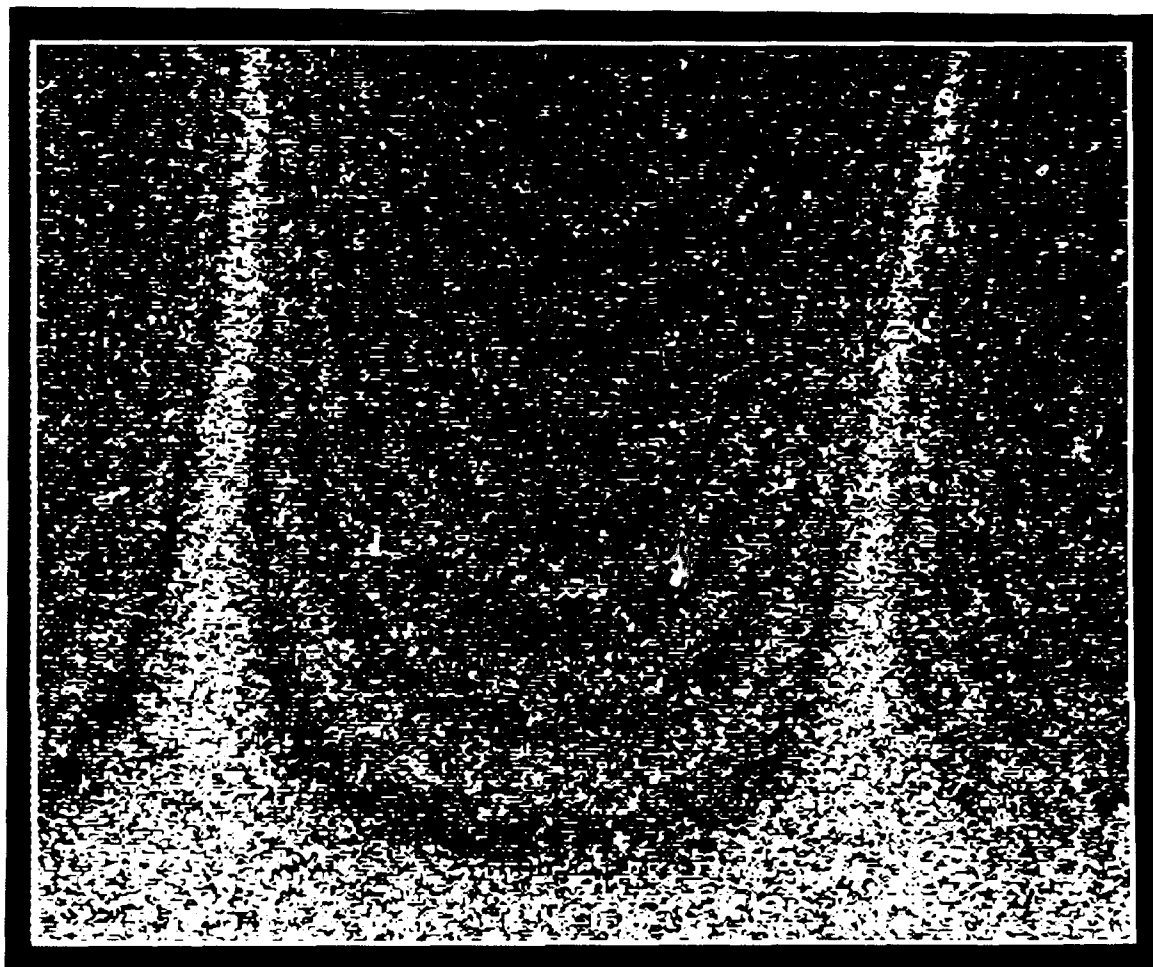
Figure B.40: A 0.08" cantilever aluminum plate in air: vibrating at 1367 Hz (2,0 mode).
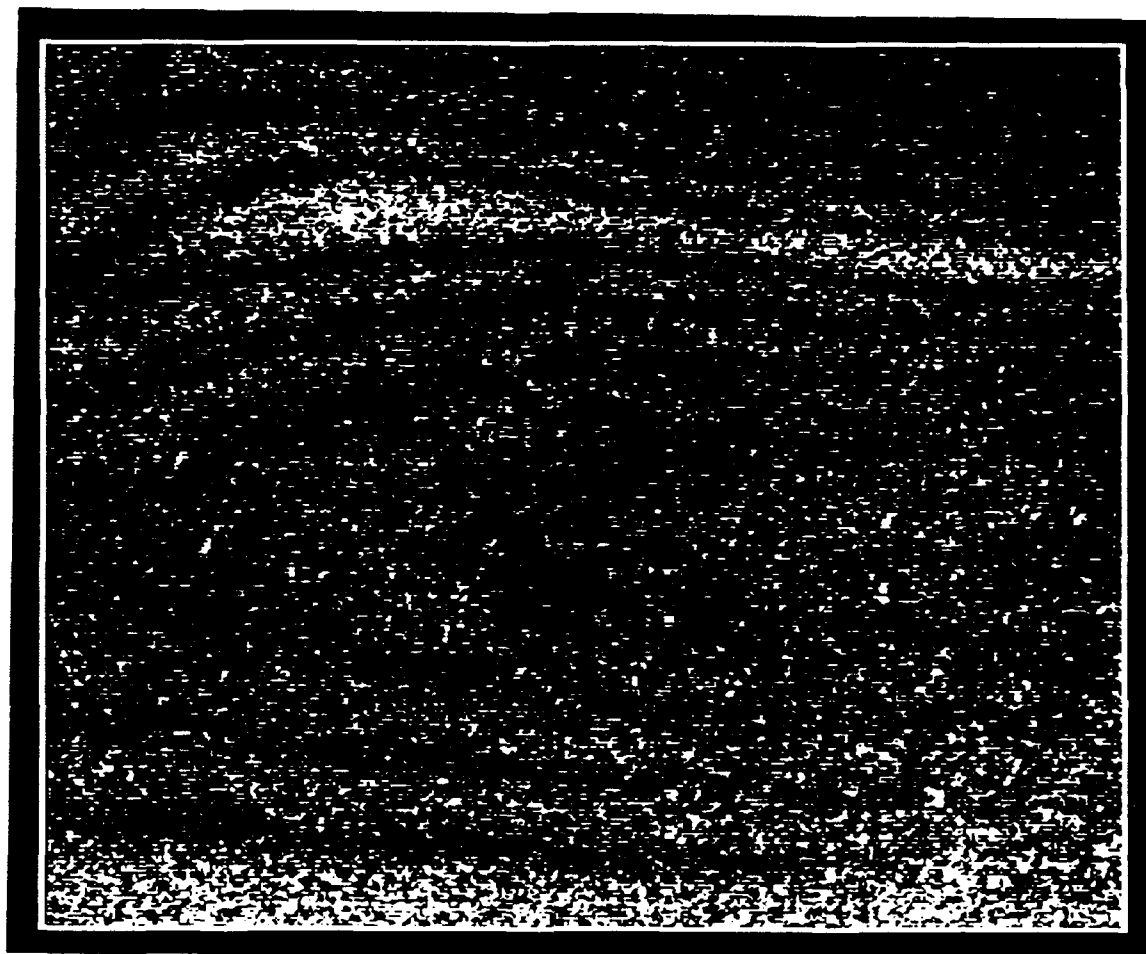
Figure B.41: A 0.08" cantilever aluminum plate in air: vibrating at 1568 Hz (0,1 mode).
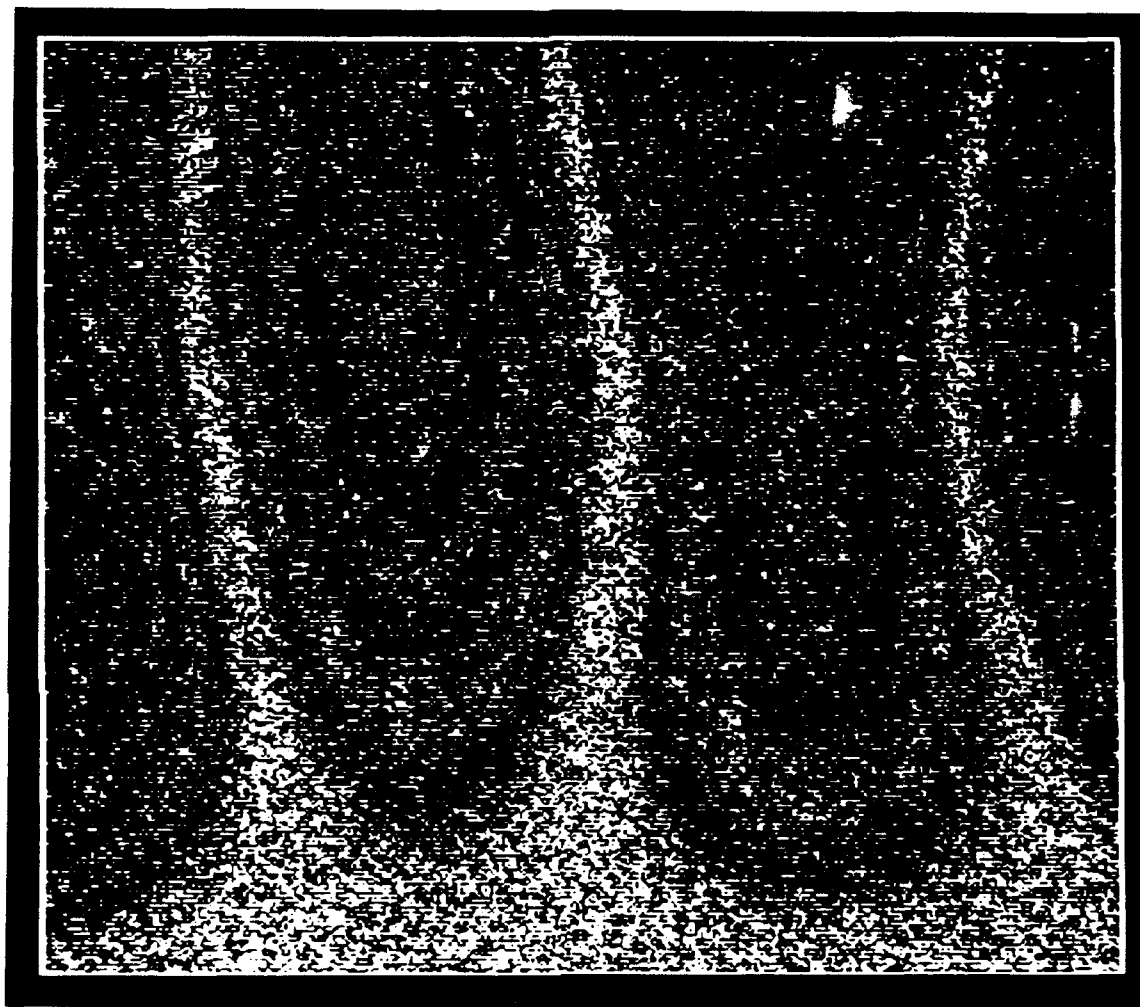
Figure B.42: A 0.08" cantilever aluminum plate in air: vibrating at 2035 Hz (1,1 mode).

Figure B.43: A   0.08"   cantilever aluminum plate in air: vibrating at 2931 Hz.

Figure B.44: A 0.08" cantilever aluminum plate in air: vibrating at 3280 Hz (3,0 mode).
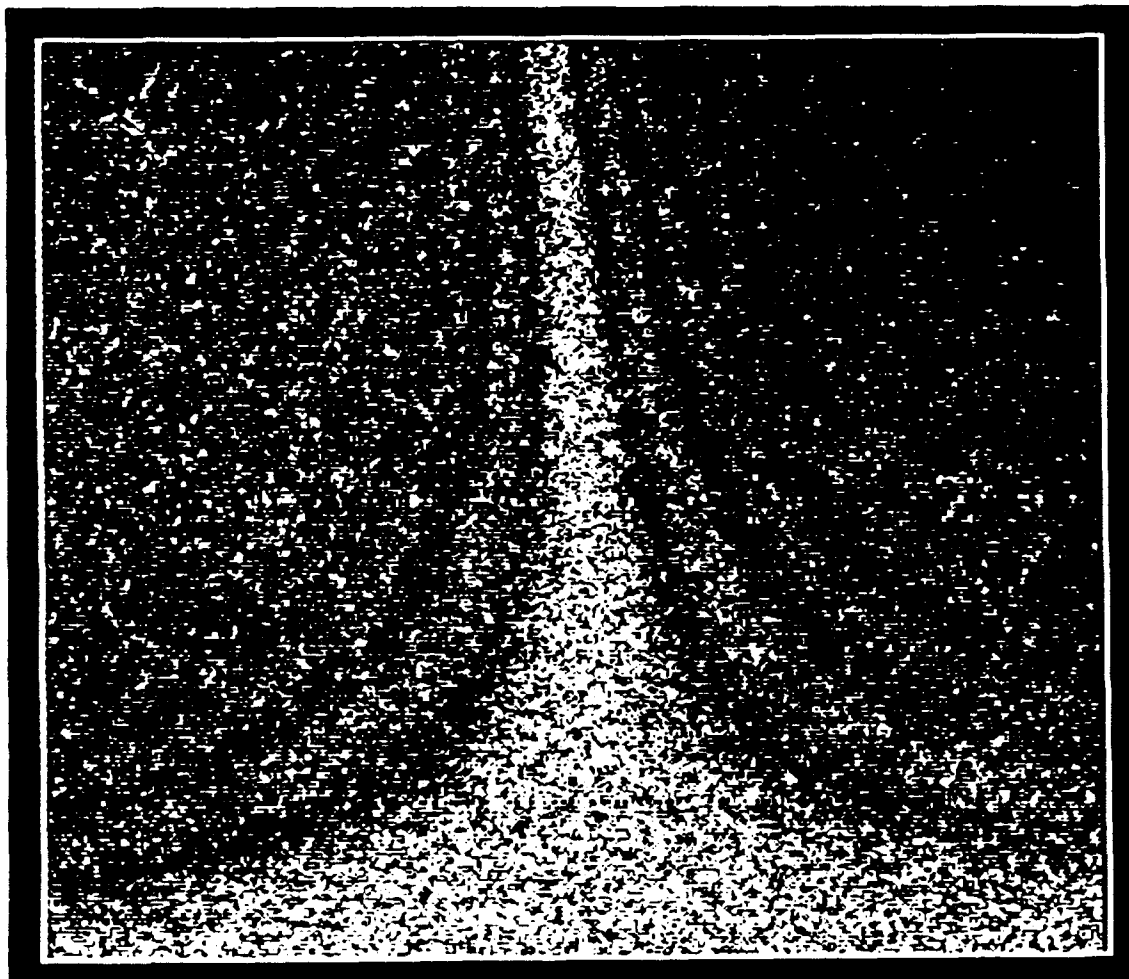
Figure B.45: A 0.08" cantilever composite plate in air: vibrating at 549 Hz (1,0 mode).
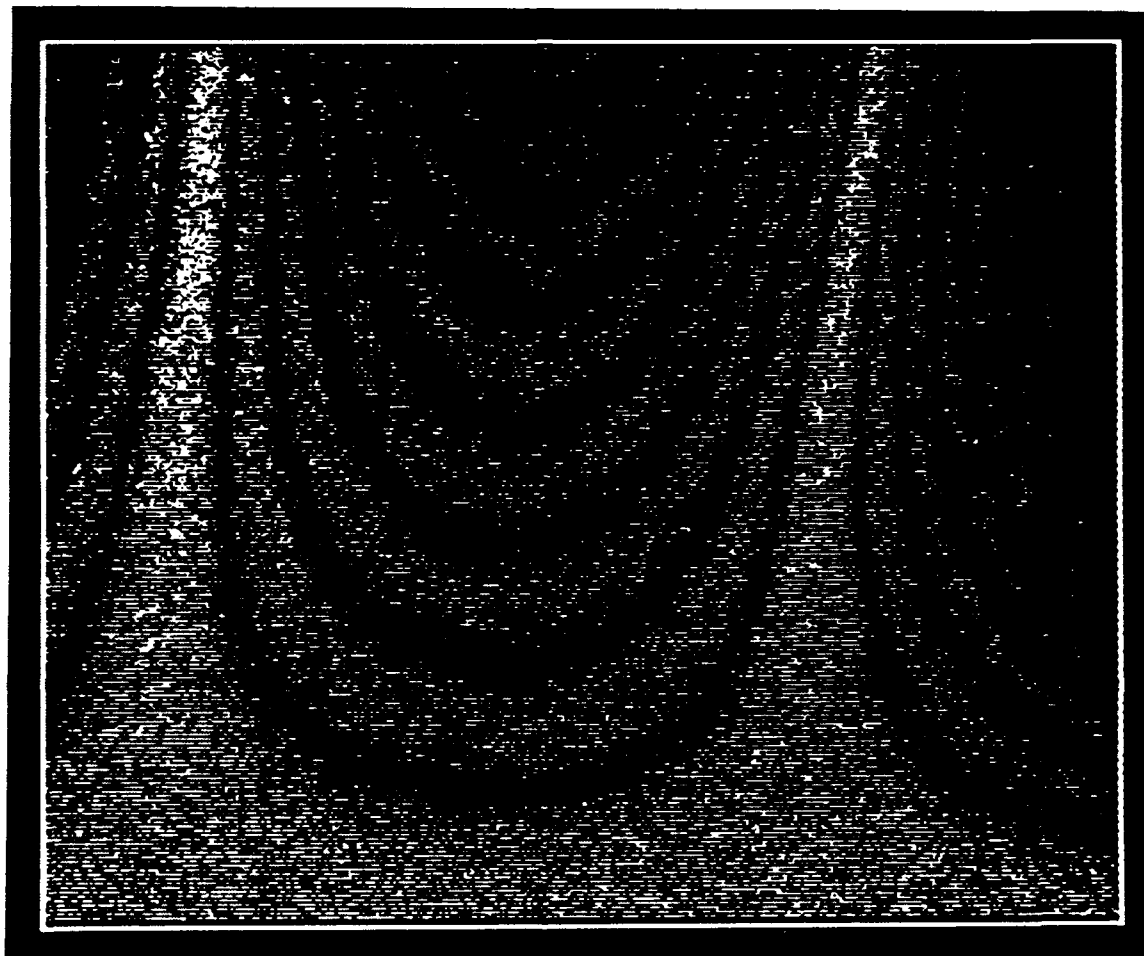
Figure B.46: A 0.08" cantilever composite plate in air: vibrating at 1282 Hz (2,0 mode).
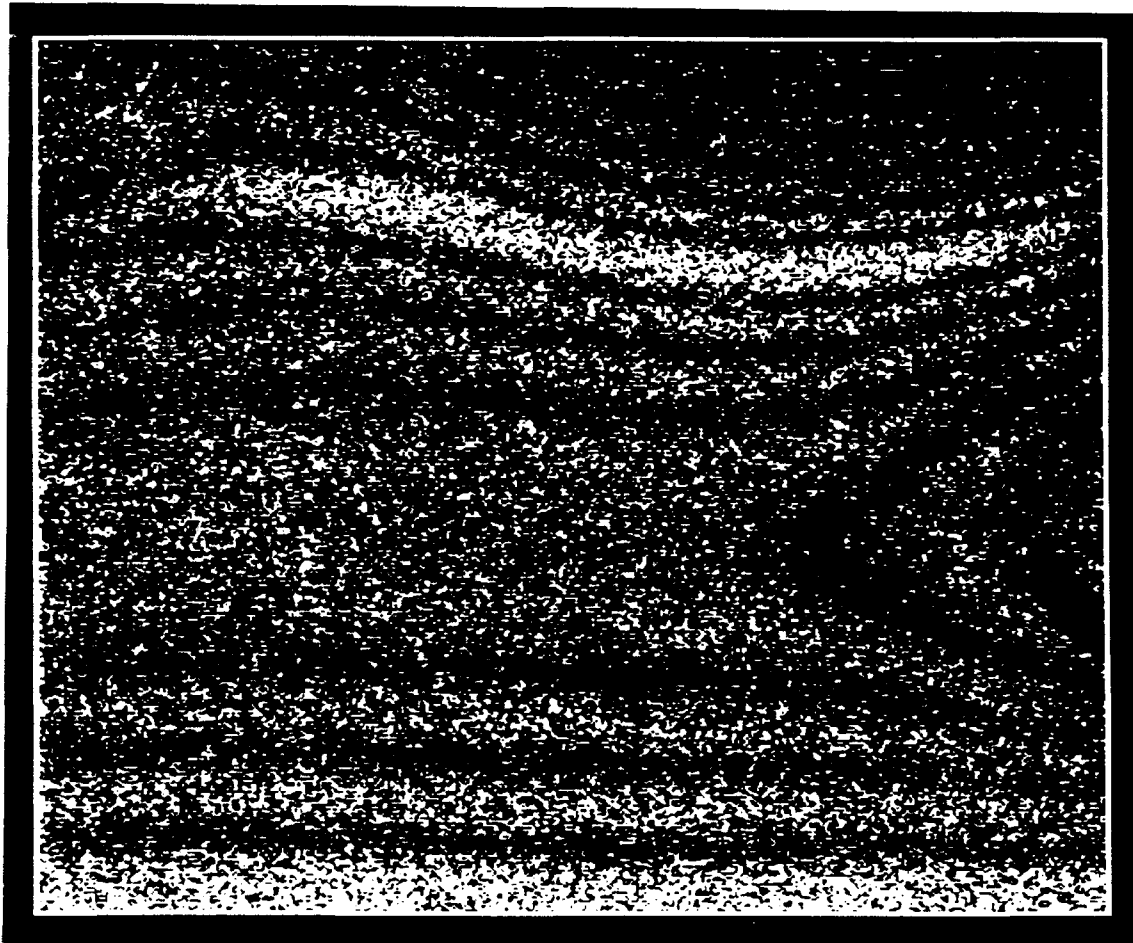
Figure B.47: A 0.08" cantilever composite plate in air: vibrating at 1842 Hz (0,1 mode).
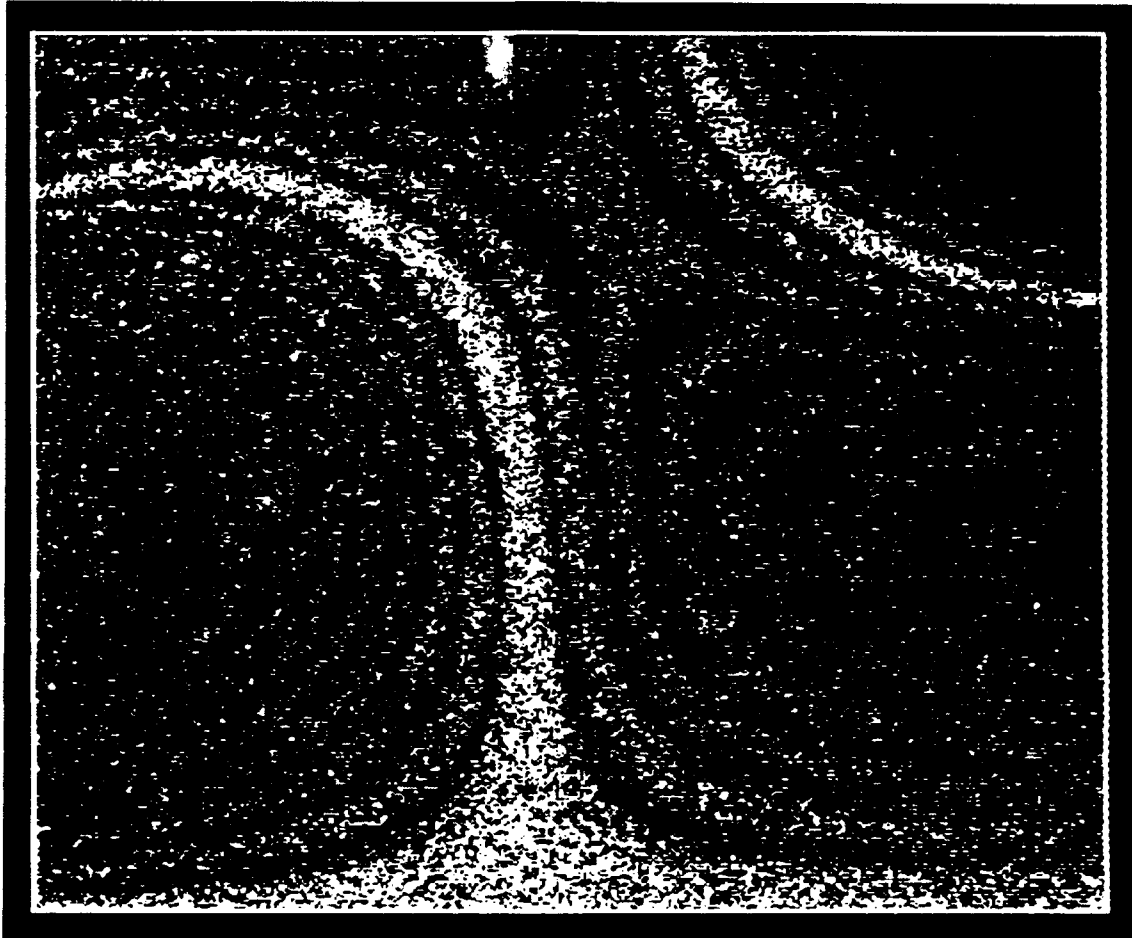
Figure B.48: A 0.08" cantilever composite plate in air: vibrating at 2255 Hz (1,1 mode).
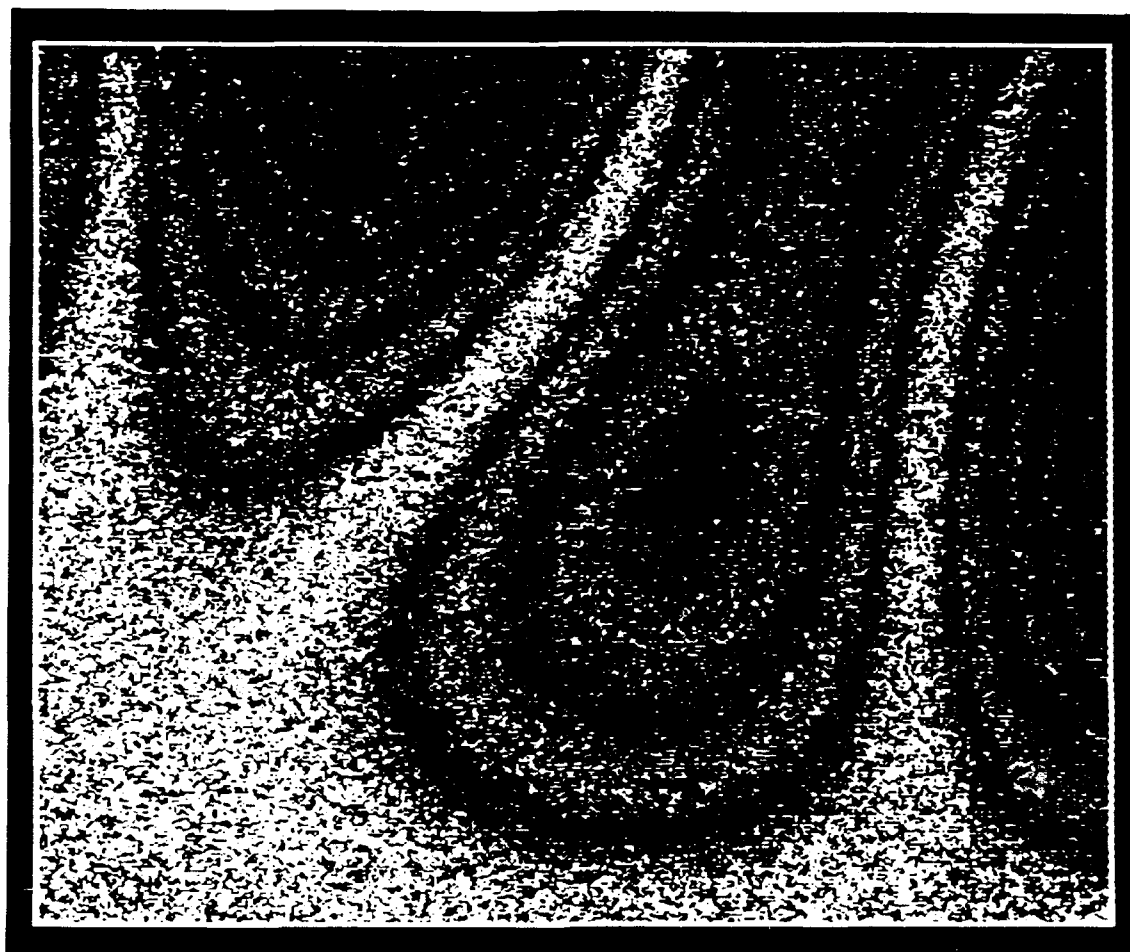
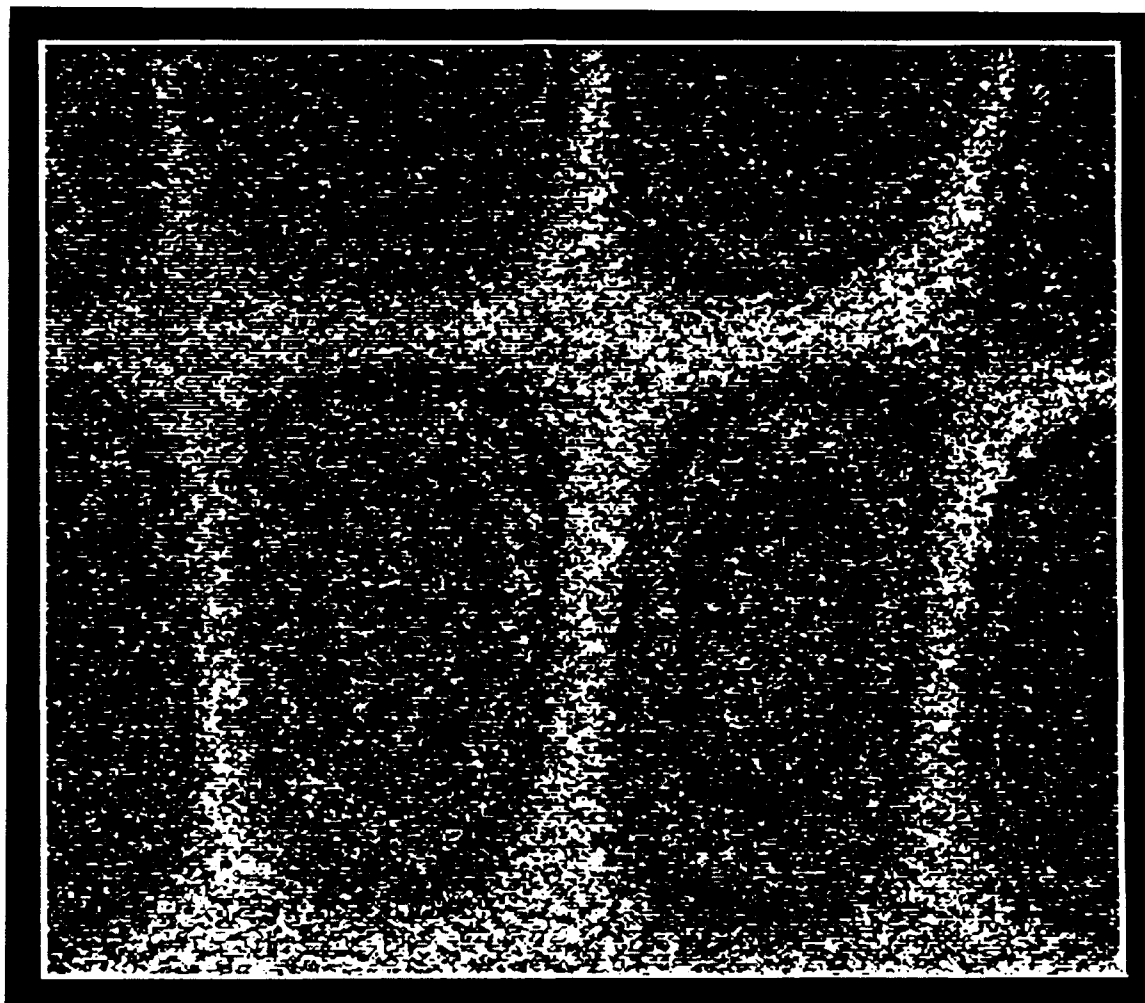Figure B.49: A 0.08" cantilever composite plate in air:
vibrating at 2898 Hz (3,0 mode).
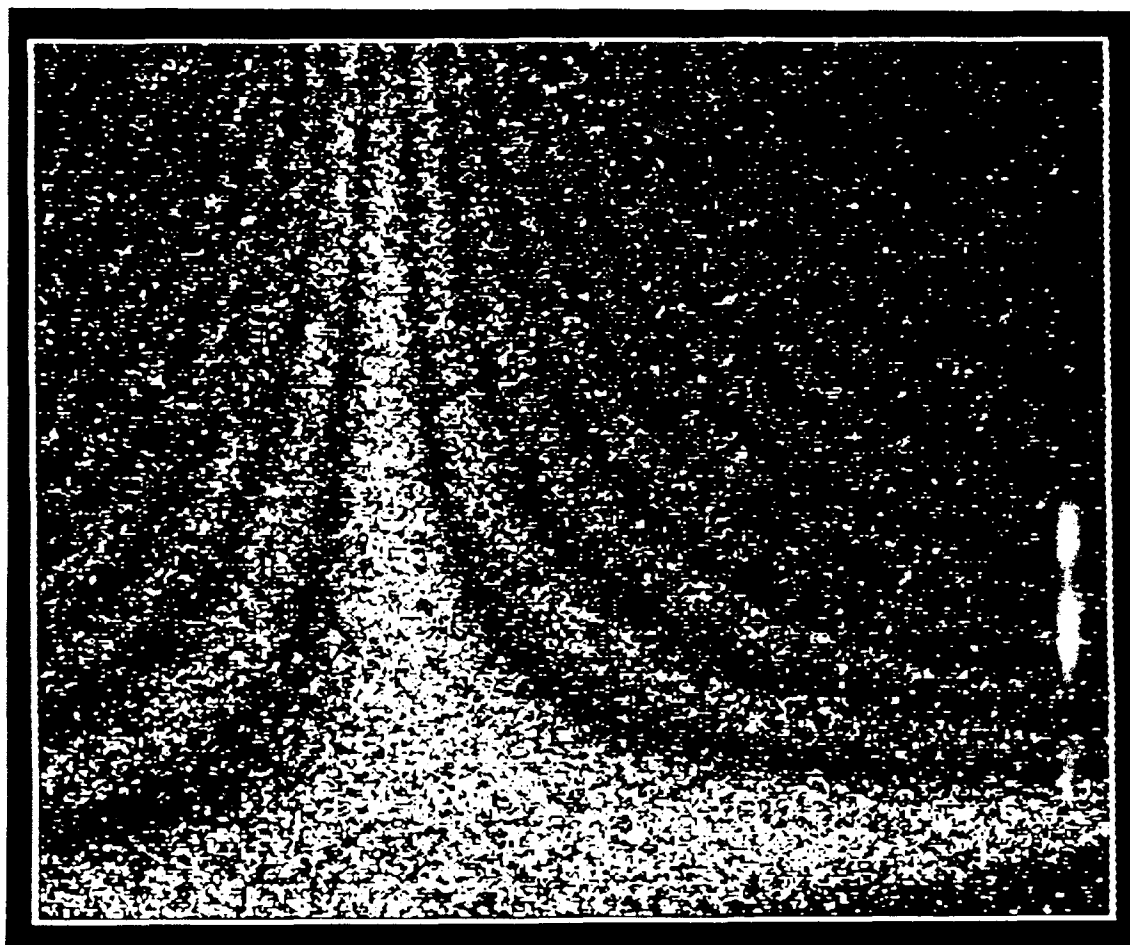
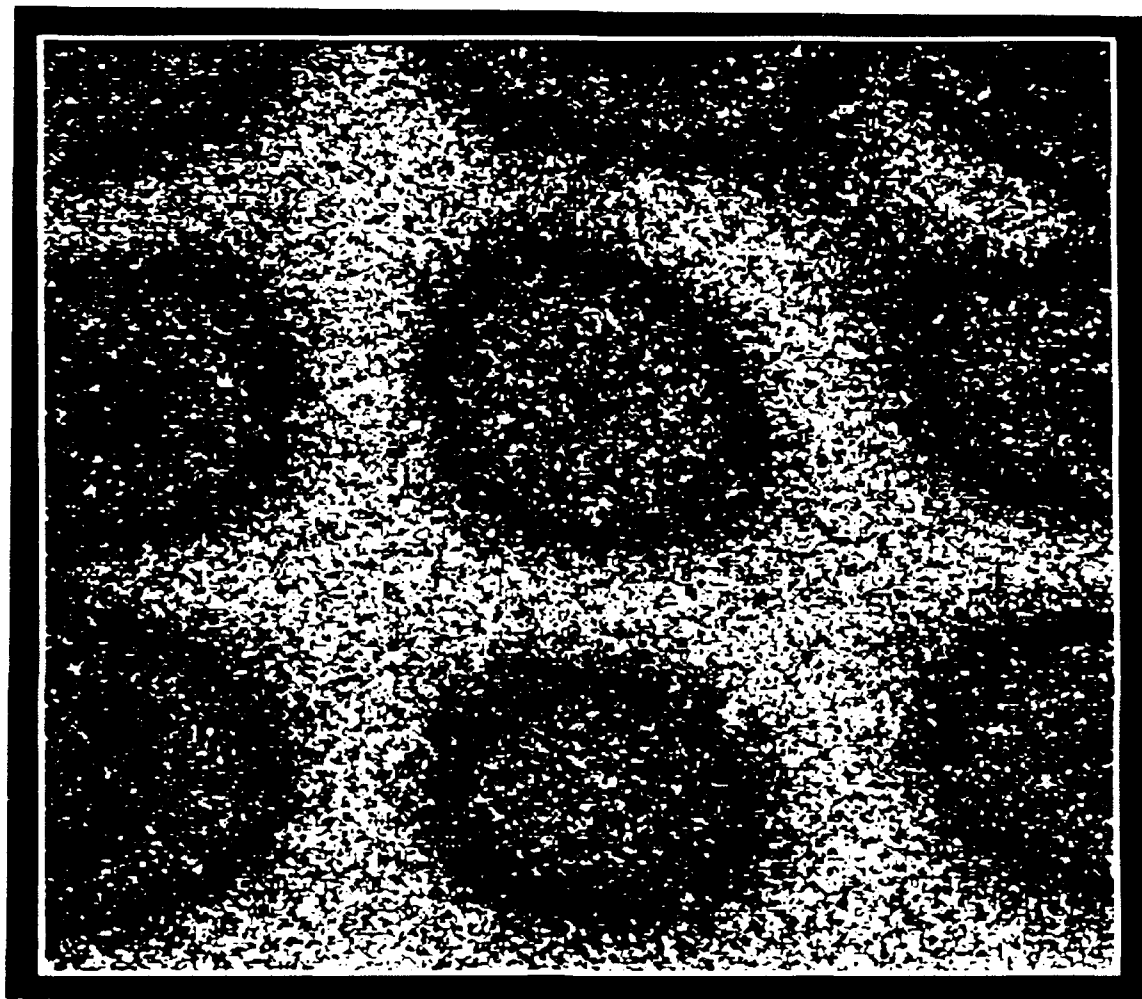Figure B.50: A 0.25" cantilever aluminum plate underwater: vibrating at 808 Hz.
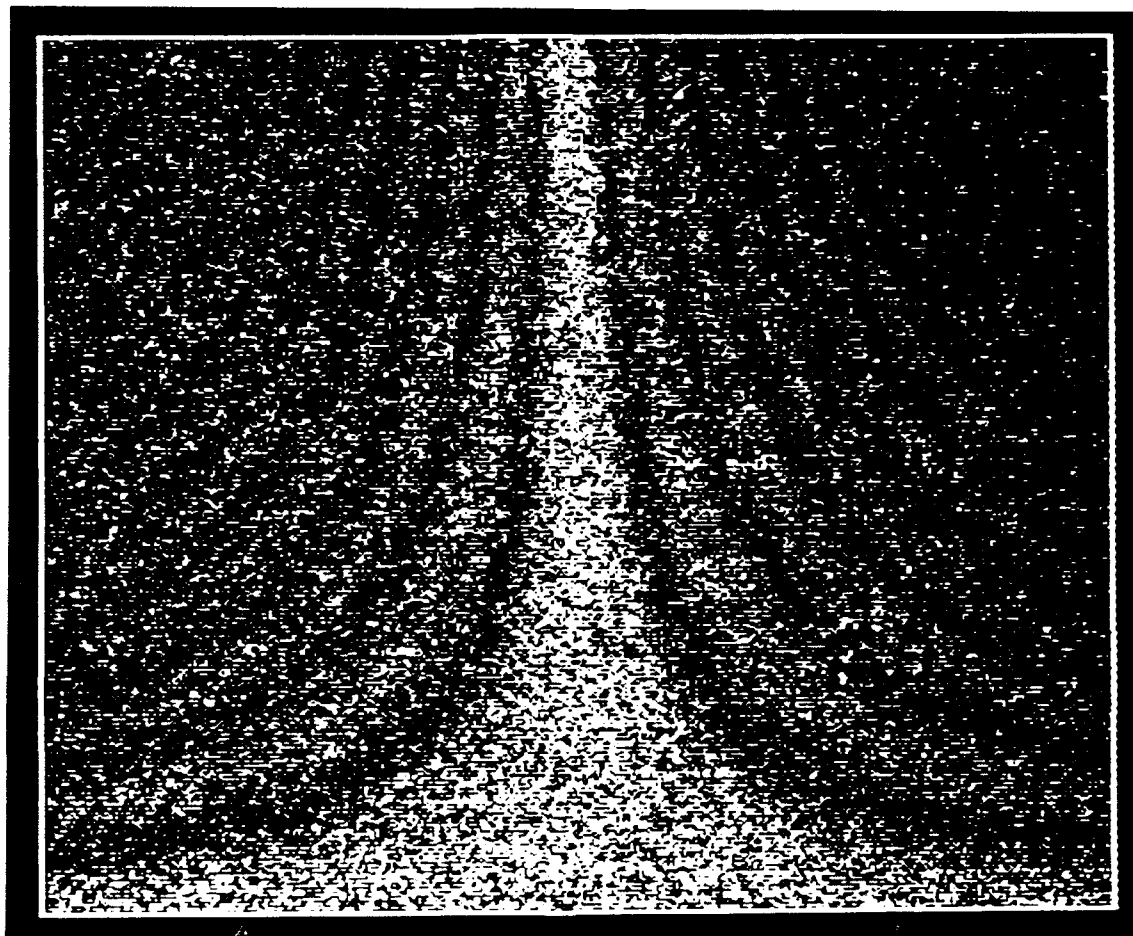
Figure B.51: A 0.25" cantilever aluminum plate underwater: vibrating at 1068 Hz (1,0 mode).

Figure B.52: A 0.25" cantilever aluminum plate underwater: vibrating at 2988 Hz (2,0 mode).

Figure B.53: A 0.25" cantilever composite plate underwater: vibrating at 961 Hz (1,0 mode).

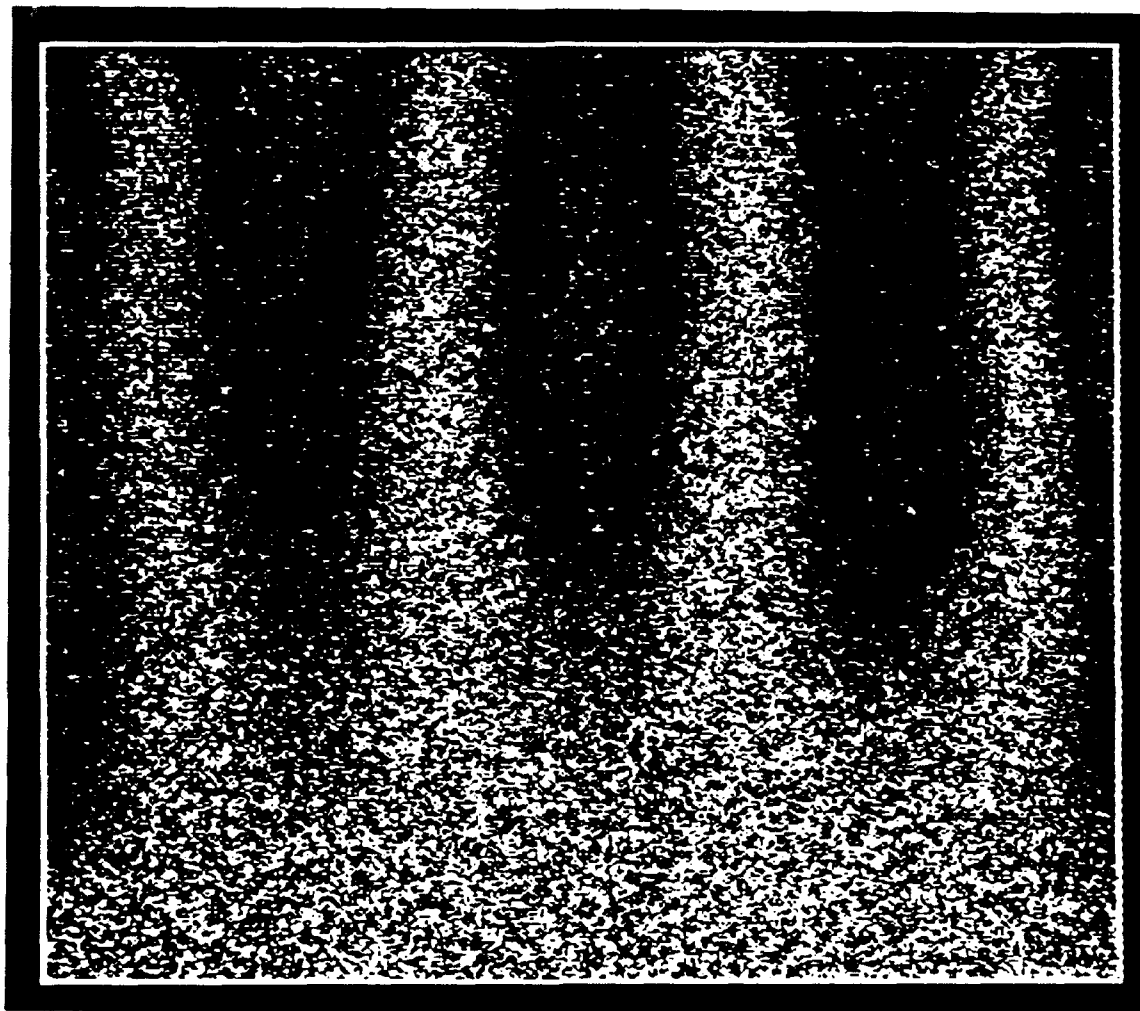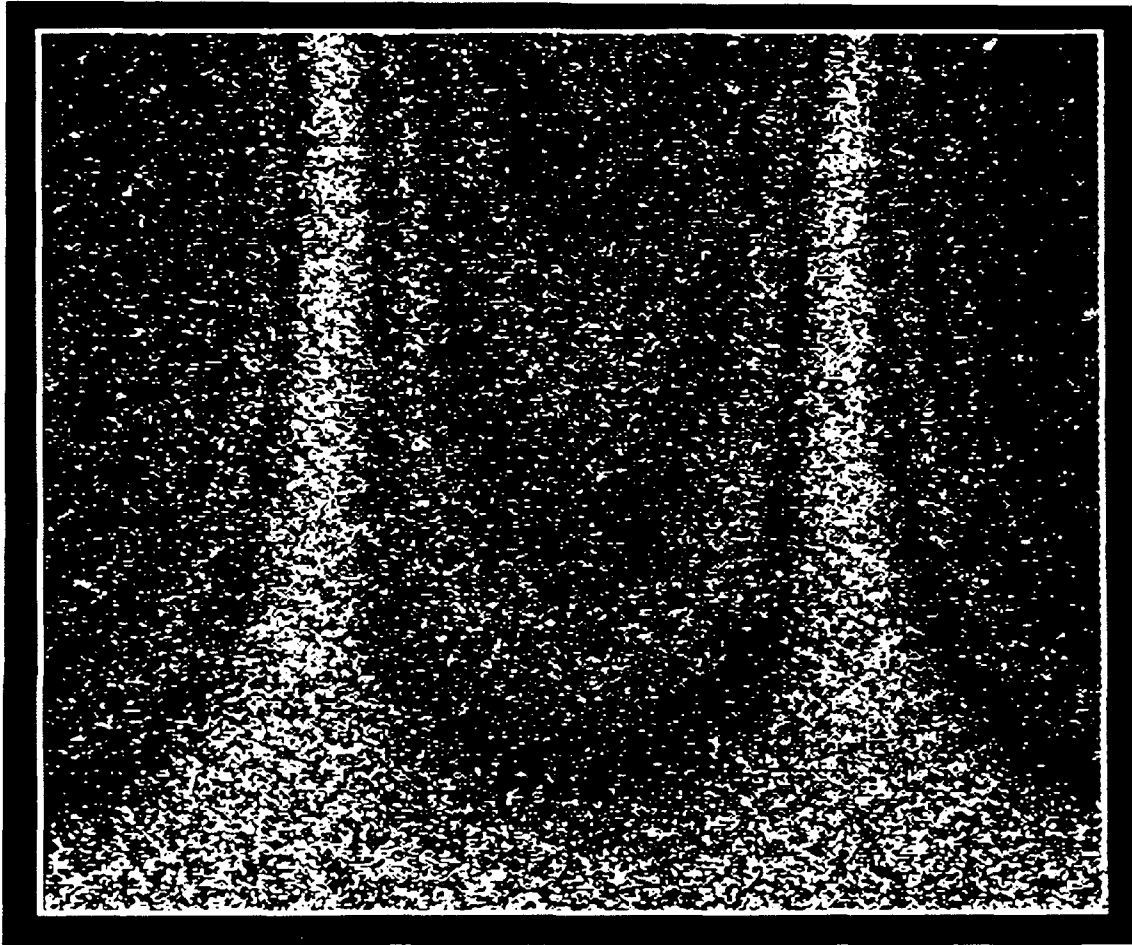Figure B.54: A 0.25" cantilever composite plate underwater: vibrating at 2649 Hz (2,0 mode).
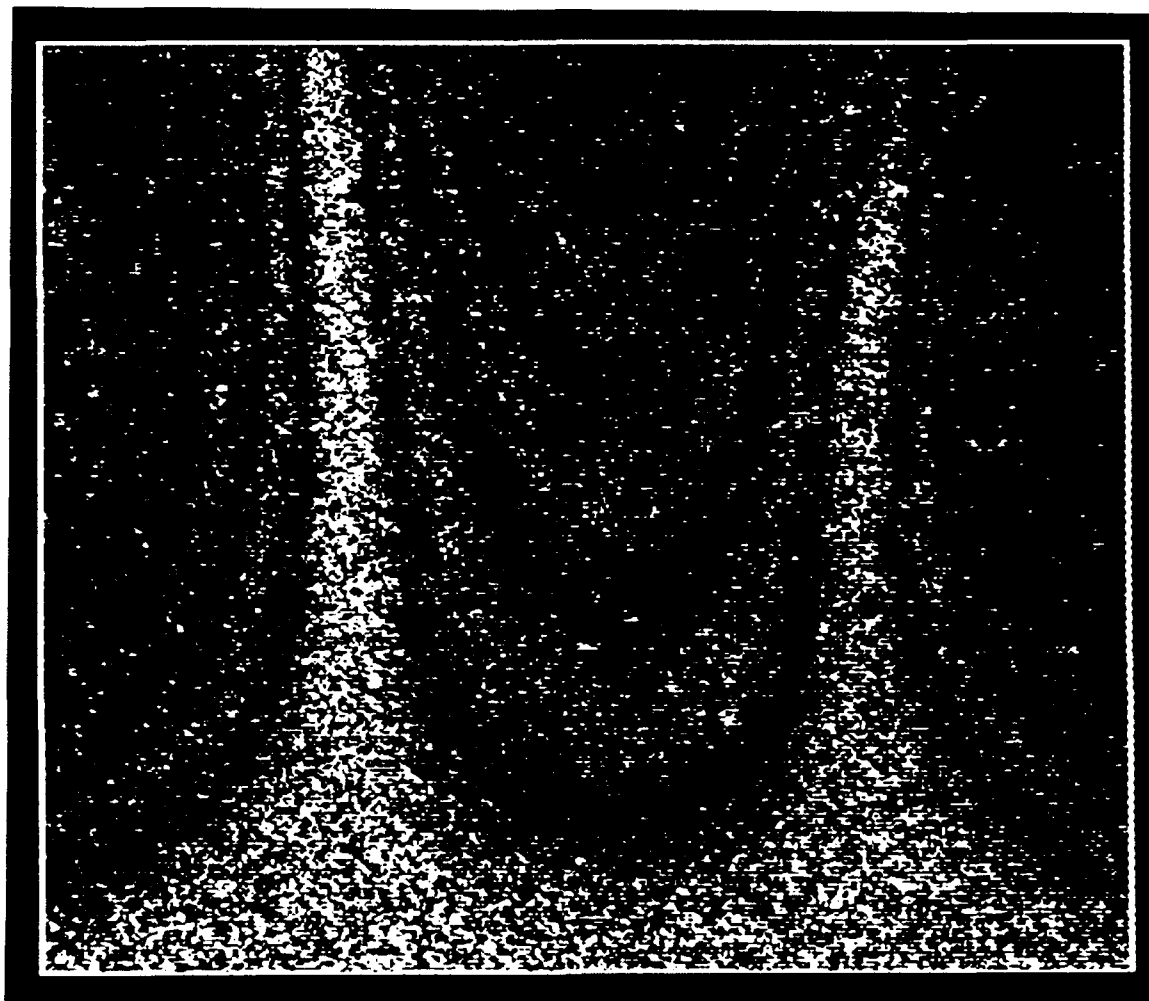
Figure B.55: A 0.08" cantilever aluminum plate underwater: vibrating at 762 Hz (2,0 mode).
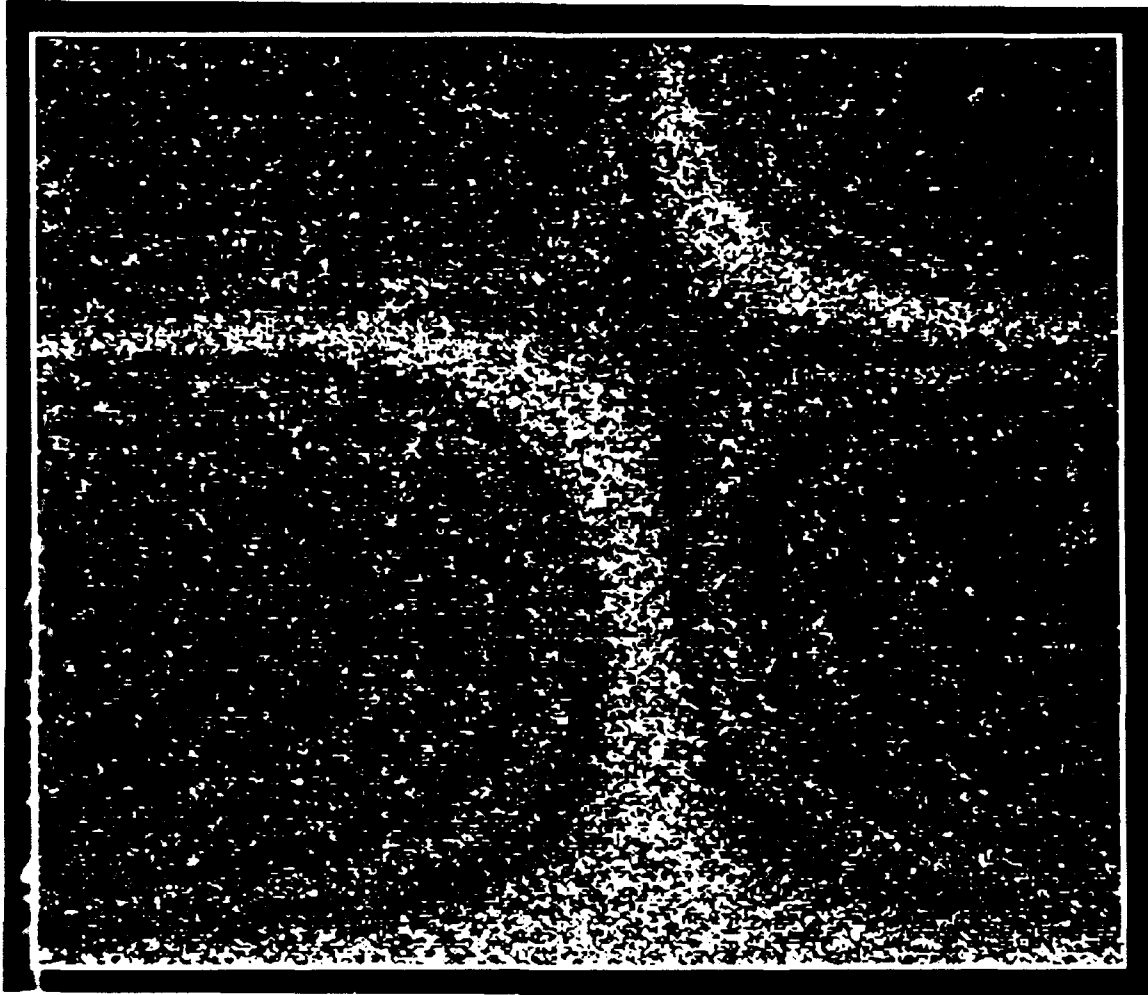
Figure B.56: A 0.08" cantilever aluminum plate underwater: vibrating at 999 Hz (1,1 mode).
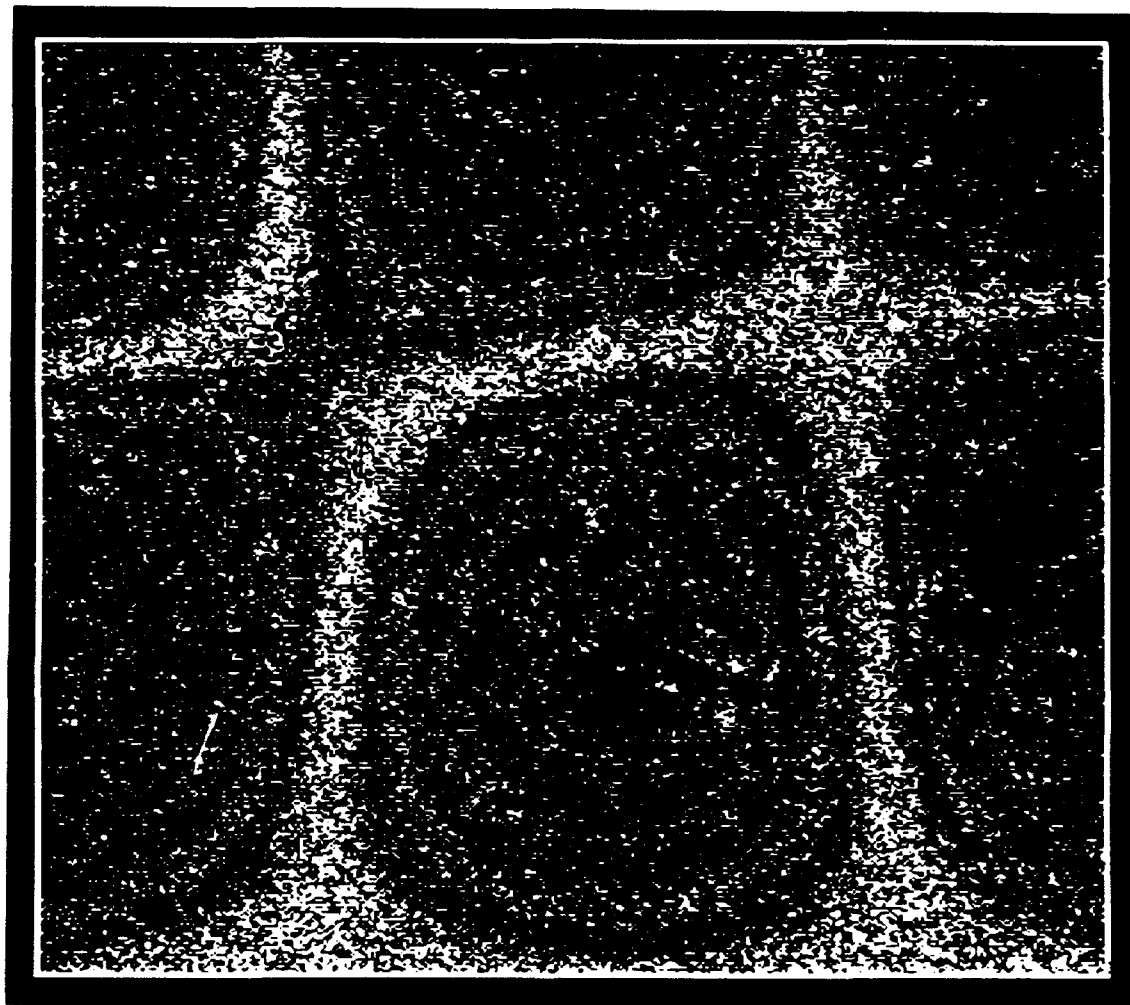
Figure B.57: A 0.08" cantilever aluminum plate underwater:
vibrating at 1563 Hz.

Figure B.58:   A   0.08"   cantilever aluminum plate underwater:
vibrating at 1726 Hz (3,0 mode).
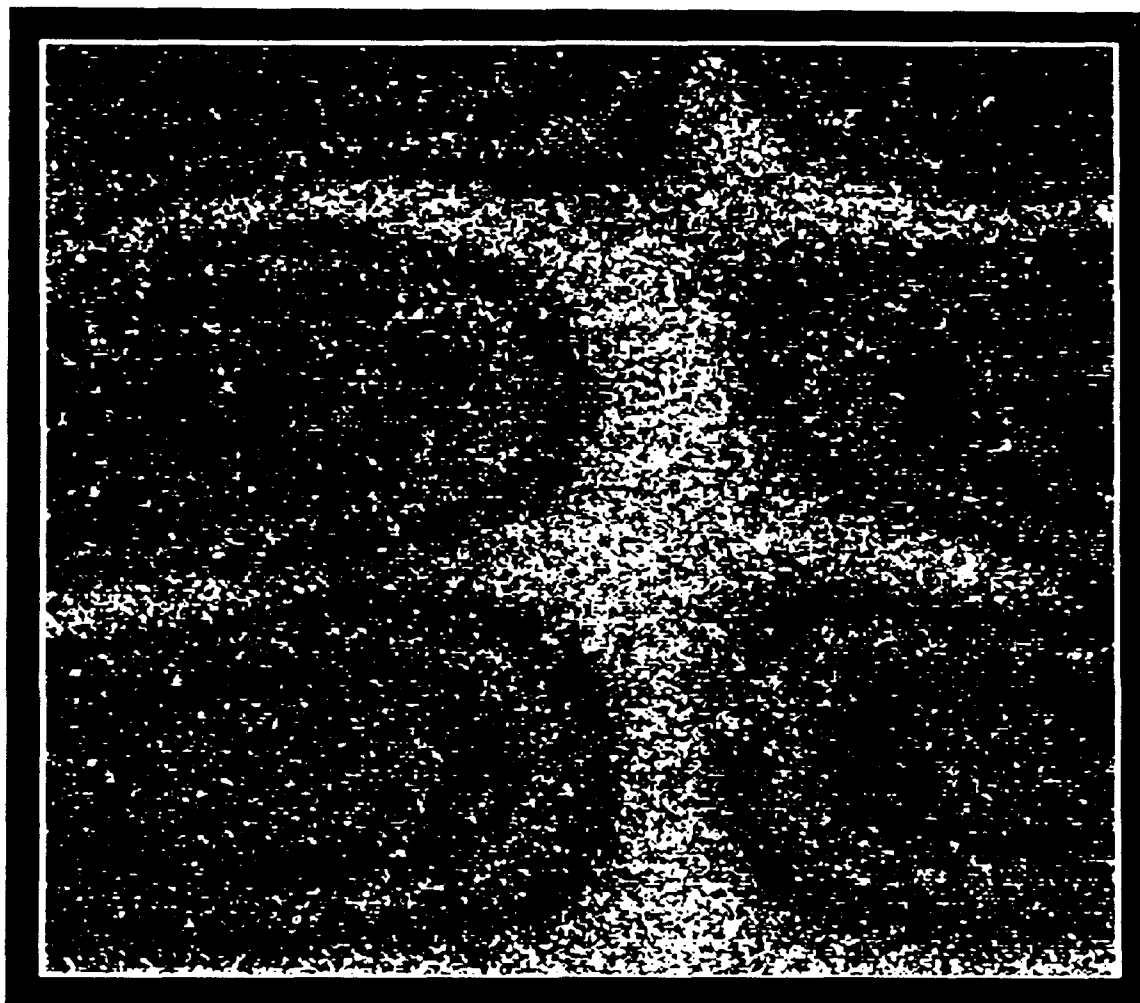
Figure B.59: A 0.08" cantilever aluminum plate underwater: vibrating at 2375 Hz (1,2 mode).

Figure B.60: A 0.08" cantilever aluminum plate underwater: vibrating at 2651 Hz (3,1 mode).

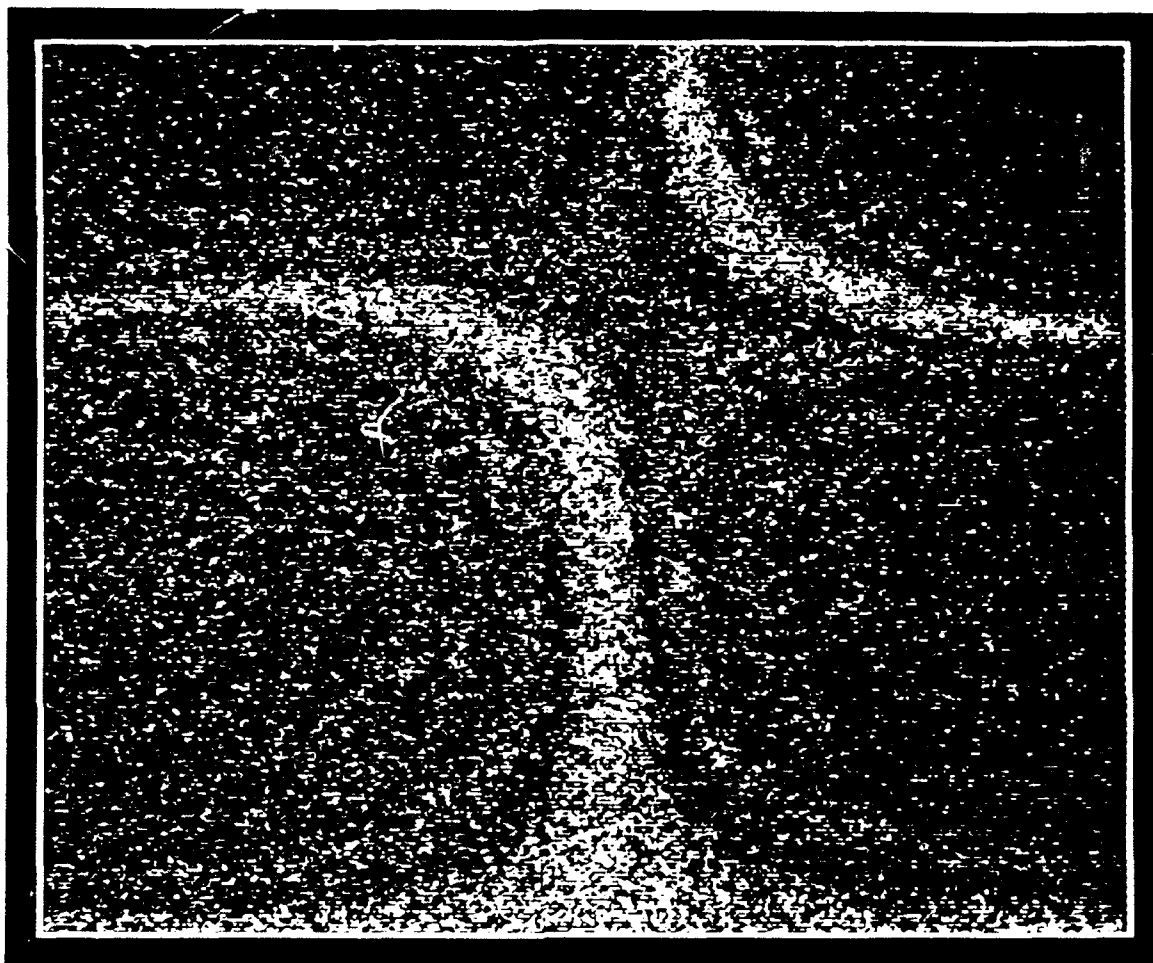Figure B.61: A 0.08" cantilever aluminum plate underwater: vibrating at 3139 Hz (2,2 mode).

Figure B.62: A 0.08" cantilever aluminum plate underwater: vibrating at 3365 Hz (4,0 mode).

Figure B.63: A 0.08" cantilever composite plate underwater:
vibrating at 583 Hz (2,0 mode).

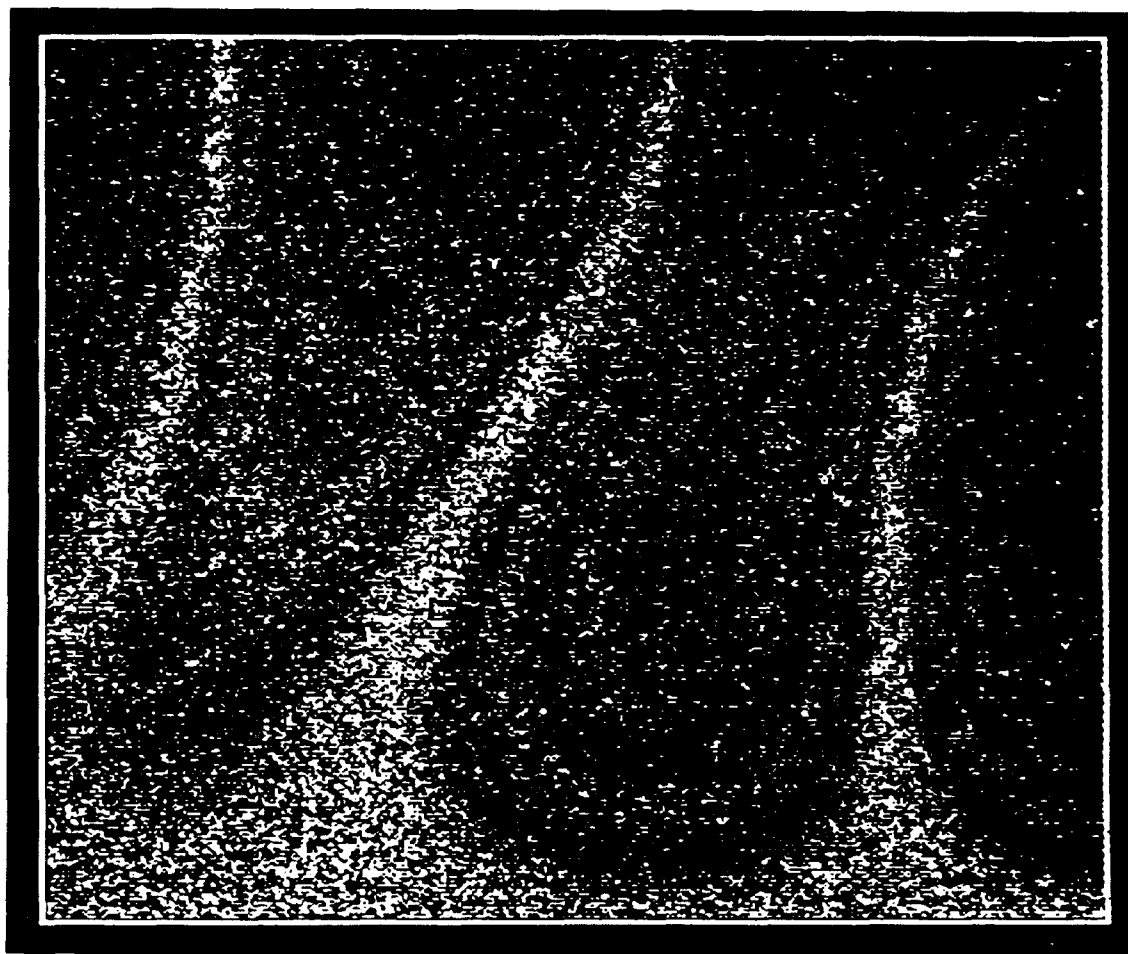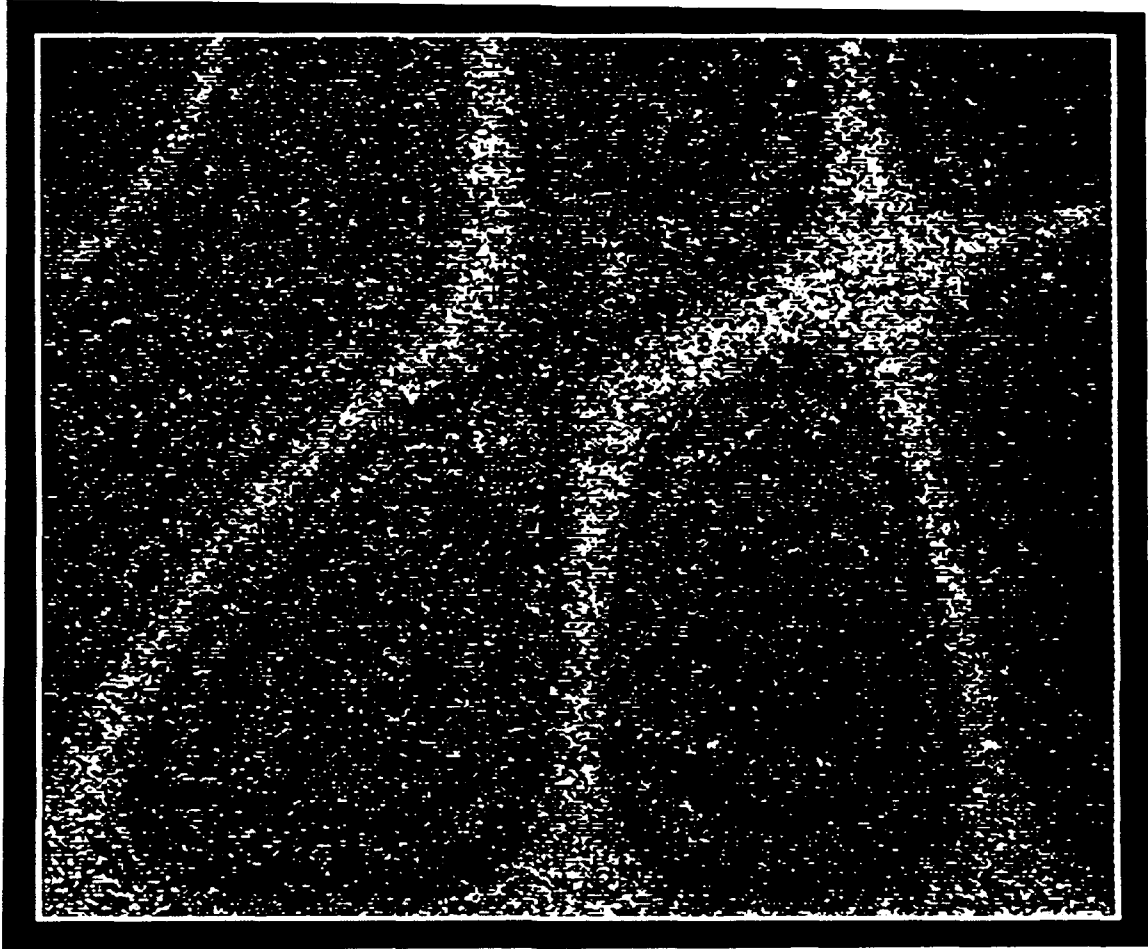Figure B.64: **A** 0.08" cantilever composite plate underwater: vibrating at 904 Hz (1,1 mode).

Figure B.65: A 0.08" cantilever composite plate underwater: vibrating at 1272 Hz (3,0 mode).

Figure B.66: A 0.08" cantilever composite plate underwater: vibrating at 2114 Hz.
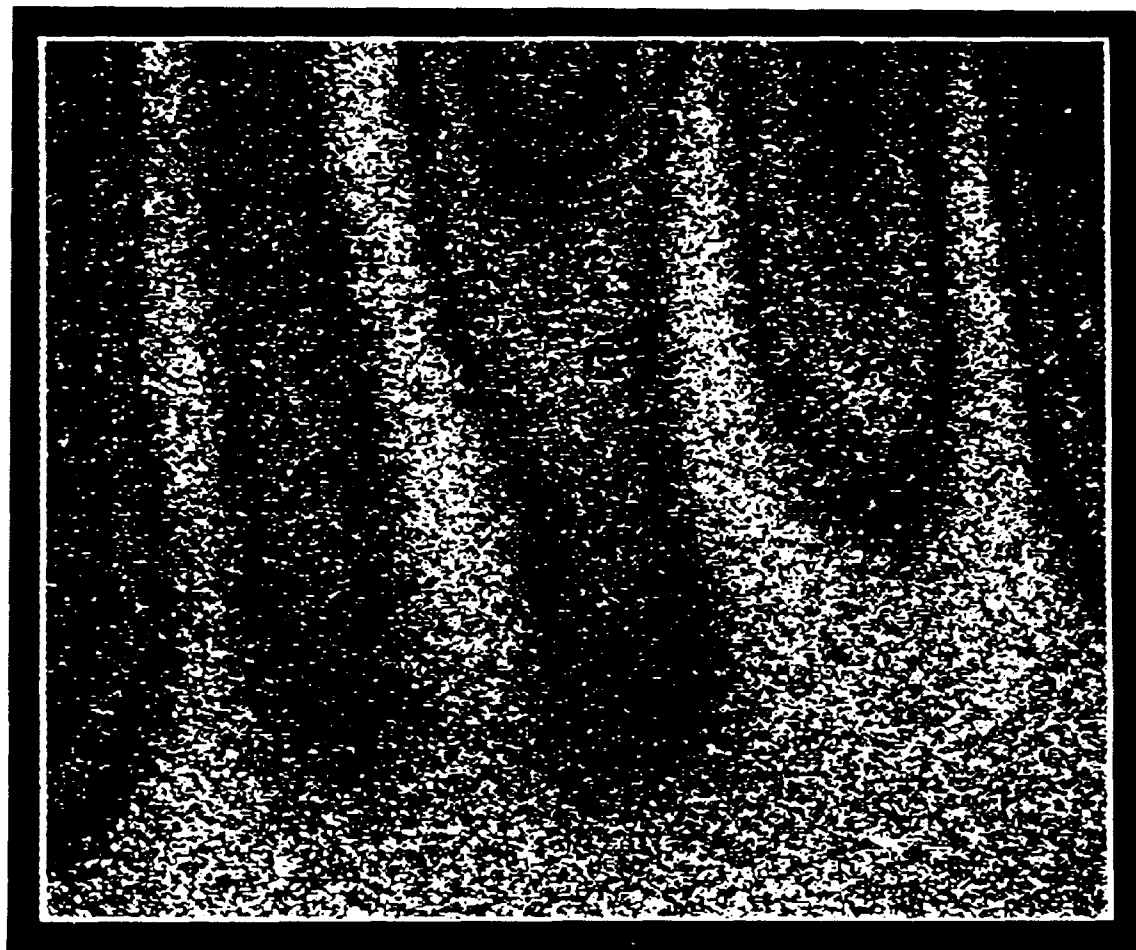
Figure B.67: A 0.08" cantilever composite plate underwater: vibrating at 2571 Hz (4,0 mode).

Figure B.68: A 0.08" cantilever composite plate underwater: vibrating at 2903 Hz (2,2 mode).